ABSTRACT

XU, ZELIN. An Improved Thermal Conductivity Model for Nanofluids with Applications to Concentration Photovoltaic-Thermal Systems. (Under the direction of Dr. C. Kleinstreuer).

Improvements in solar photovoltaic and thermal conversion efficiencies may accelerate the development of economically viable concentration photovoltaic-thermal (CPV/T) systems. Nanofluids, used as coolants, promise improved solar-to-electric as well as solar-to-thermal energy conversion efficiencies due to their enhanced thermal conductivities.

A nanofluid is a mixture consisting of nanometer-size particles or fibers dispersed in a liquid. It has been found that even at low volume fractions of nanoparticles the thermal conductivities of the mixtures were significantly enhanced with relatively small penalties in pressure drop, indicating potential applications as a new type of heat transfer fluid. On the other hand, despite many efforts, theories cannot fully explain the reasons for elevated thermal conductivities. Hence, a theory based on solid physical grounds is needed to describe the enhanced thermal conductivity of nanofluids. A model for nanofluid thermal conductivity is presented in Chapter 2 and compared to experimentally observed evidence. This model is an improvement of an existing model of nanofluid thermal conductivity based on Brownian motion effects, i.e., the F-K model (Kleinstreuer & Feng, 2012). The new model incorporates nanoparticle aggregation effects and interfacial thermal resistance, in addition to the Brownian motion induced “micro-mixing” effects. Specifically, nanoparticles may form fractal-like aggregates in the base fluid due to particle-particle as well as particle-fluid interactions. The aggregation provides bridges for fast heat transfer between particles. In addition, the aggregates can be treated as effective spheres that undergo Brownian motion in the base fluid. The Brownian motion of aggregates perturbs the base fluid and introduces

micro-scale mixing effects that enhance the heat transport between fluids with different temperatures. On the other hand, the interfacial thermal resistance creates a barrier against effective heat transfer across the interface between the solid and the fluid; thus, weakening the effective thermal conductivity. In general, the effective thermal conductivity of the nanofluids consists of two parts, i.e., $k_{nf} = k_{\text{static}} + k_{mm}$, where the static part, k_{static}, is due to the existence of the nanoparticle aggregates, and the "micro-mixing" part, k_{mm}, is due to Brownian-motion induced fluctuations. The new k_{nf} model predictions for different nanoparticles in water were compared with benchmark experimental data sets as well as recent experimental results to validate the model.

The newly developed k_{nf} model has been incorporated in a numerical study of thermal analyses of a CPV/T system. Specifically, a two-dimensional cooling channel with photovoltaic cells, subject to heat conduction and turbulent nanofluid convection, was used to study the effects of inlet temperature, inlet Reynolds number, and channel height on cell efficiency. An analysis of entropy-generation minimization was employed to determine an optimal geometric configuration and best operational conditions. Simultaneously, we used a counter-flow double-tube heat exchanger to evaluate the influence of inlet Reynolds number and inlet temperature on the thermal as well as overall efficiencies of the system. It was determined that a high Reynolds number for flow in the annular and a low Reynolds number for flow in the inner tube are desirable; but, performance was limited in the laminar flow regime. Moreover, high nanofluid temperature promotes the overall efficiency of the system. The performance of nanofluid in the heat recycling part was compared with that of pure water, demonstrating that a better efficiency was achieved when using nanofluids.

An Improved Thermal Conductivity Model for Nanofluids with Applications to Concentration Photovoltaic-Thermal Systems

by
Zelin Xu

A thesis submitted to the Graduate Faculty of
North Carolina State University
in partial fulfillment of the
requirements for the degree of
Master of Science

Mechanical Engineering

Raleigh, North Carolina

2014

APPROVED BY:

_____	_____
Dr. C. Kleinstreuer Committee Chair	Dr. B. T. O'Connor
_____	
Dr. J. F. Selgrade	

BIOGRAPHY

The author was born on December 5, 1988 in Shan Town, Shandong Prov., China.

After graduating from high school, he was admitted to Central South University (CSU), China, in 2006 and studied in the Department of Energy Science and Engineering. The author earned his Bachelor degree in Thermal Energy and Power Engineering in 2010, and continued one year of graduate study in the same department focusing on microfluidics. After that, he took a half-year break.

The author enrolled as a doctoral student on January, 2012 in the Department of Mechanical and Aerospace Engineering at North Carolina State University in Raleigh, NC. His MS thesis research focused on nanofluid heat transfer property analysis and computational nanofluid flow and heat transfer analysis applied to concentration photovoltaic-thermal systems.

ACKNOWLEDGMENTS

I would like to express a great deal of appreciation for Dr. C. Kleinstreuer, Chairman of my advisory committee. His physical insight, guidance and encouragement have been the impetus for me to climb. He has proven to be a very considerate advisor who serves as a role model for professional excellence and integrity. He has provided me with both intellectual freedom and timely guidance, which I especially value and appreciate. He has shown great patience on me when I explore, especially given my introversive nature. I feel very lucky to work with him who has absolute rigor in academia and enormous humor in life.

I would like to express the greatest gratitude to my mother country, China. Without the fellowship from the China Scholarship Council, I could not even have dreamt of coming to the United States to pursue the degree.

Appreciation is also extended to Dr. J. F. Selgrade and Dr B. T. O'Connor for serving as committee members, and offering superb classes. The author appreciates Dr. Y. Feng for providing guidance on nanofluid heat transfer theories and numerical simulations as well as many helps in my daily life, Dr. E. M. Childress for providing advices on numerical skills and American culture, and Dr. J. Li for his help when I first arrived here. The author was happy to be with all the members in our Computational Multi-Physics Laboratory, including Dr. Z. Zhang, Mr. A. V. Kolanjiyil, Mr. T. Umbarkar, Mr. M. Vaish, and Mr. X. Chen.

I feel indebted to Dr. P. Zhou in CSU. Her guidance during my years in CSU set a solid base for me to climb up to the top. I would also like to thank Dr. J. R. Edwards Jr. of Department of Mechanical and Aerospace Engineering and Dr. S. Tsynkov of Department of Mathematics of NCSU for offering superb classes.

Special gratitude should go to my parents, who supported me in every way to pursue my study, and to my older sister, whose generosity and kind-heartedness have always been invaluable to me.

TABLE OF CONTENTS

LIST OF TABLES

LIST OF FIGURES

Chapter 1

INTRODUCTION AND OVERVIEW

1.1 Nanofluids as Coolants

A nanofluid is a mixture consisting of nanometer-size particles (e.g. metal-oxide particles or nanodrugs) or fibers (e.g. carbon nanotubes) dispersed in a liquid at low volume fractions (see Fig. 1.1). Nanofluids have emerged as a new type of heat transfer fluid more than a decade ago, during which period a lot of experimental, theoretical and numerical work has been done to investigate the convective and conductive heat transfer characteristics of nanofluids and their applications. It has been found that with low volume fractions of nanoparticles, the thermal conductivities of the mixtures were significantly enhanced (up to 200% when using carbon nanotubes) with relatively small penalty in pressure drop. In addition to the advantages of nanofluids for microchannel cooling, they are also part of nanodrug delivery (see Fig. 1.2 and Kleinstreuer et al. (2013)).

Among many of the properties of nanofluids, the thermal conductivity, k_{nf}, has been studied extensively. Experiments have been conducted for nanofluids with metal, metallic, and organic nanoparticles dispersed in different base fluids, including water, ethylene glycol (EG), and oil. However, the results scattered from minimal to substantial enhancement of k_{nf} over the thermal conductivity of the base fluid. This may be due to a number of reasons, e.g., aggregation, complex colloidal chemistry, and thermodynamic conditions (Shima & Philip, 2014). Meanwhile, because the enhancement cannot be predicted using convectional models

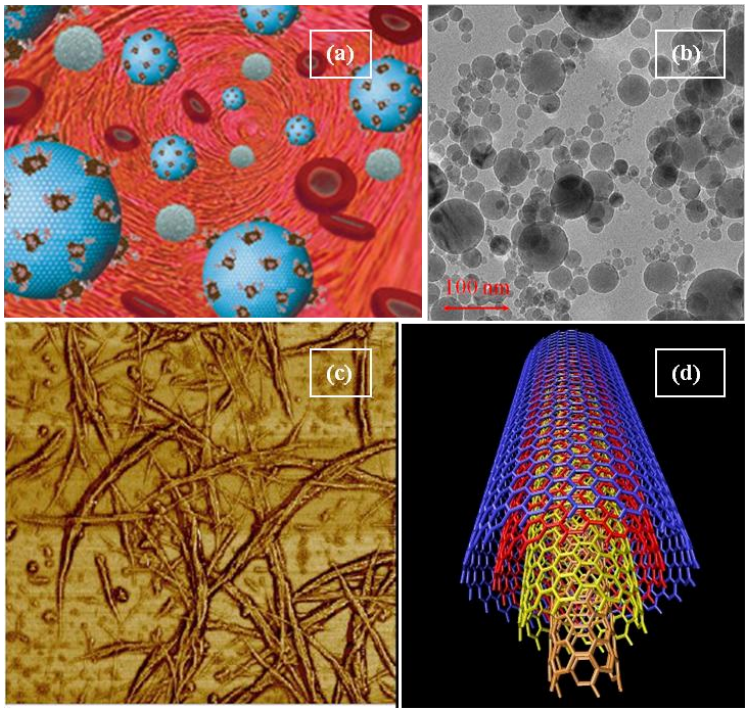

Figure 1.1: Typical nanoparticles and nanofibers: (a) Nanodrug carriers in blood vessel (http://www.inforural.com.mx/spip.php?article49682); (b) Transmission electron microscope (TEM) image of a 0.06% Al_2O_3/water nanofluid (http://www.users.muohio.edu/sommerad/research.html); (c) An atomic force microscope (AFM) image of carbon nanotubes, before removing the metallic tube (http://www.news.cornell.edu/stories/2009/01/cornell-dupont-make-nanotubes-flexible-electronics); and (d) Multi-wall carbon nanotubes (http://www.nanotech-now.com/nanotube-buckyball-sites.htm)

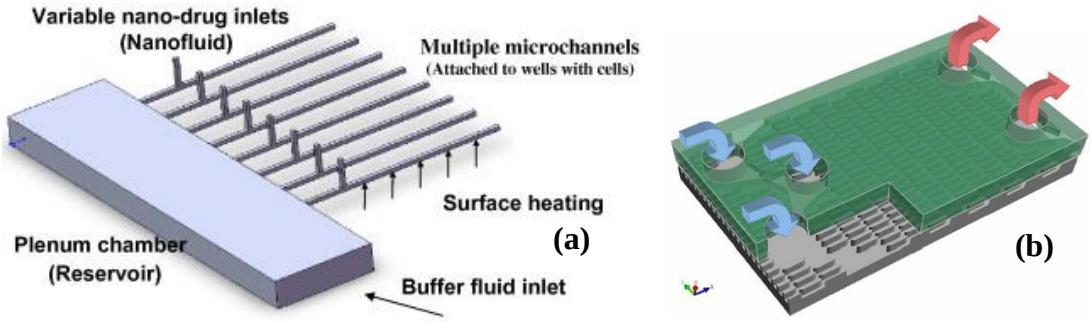

Figure 1.2: Selected applications of nanofluids: (a) Nanomedicine delivery system(Kleinstreuer et al., 2008); (b) Nanofluid cooling of microchannel heat sinks (http://www.mae.ncsu.edu/cmpl/nanoflow.htm)

based on the effective medium theory (Keblinski et al., 2002), four major mechanisms have been proposed to account for the anomalous k_{nf} –augmentation. Specifically,

- Brownian motion of nanoparticles;
- molecular-level layering of the liquid at the liquid/particle interface;
- ballistic heat transport in the nanoparticles; and
- effects of nanoparticle clustering.

Various k_{nf} models have been proposed based on one or several of these mechanisms. However, they have limited abilities in accurately predicting k_{nf} of different nanoparticle-base fluid pairings as well as under broad ranges of temperatures and nanoparticle volume fractions.

1.2 Solar Photovoltaic-Thermal Systems

Electricity production via solar photovoltaic cells is believed to have the potential to be the next-generation energy source. However, cooling of photovoltaic cells has been a challenge especially for high concentration photovoltaic (CPV) systems, where concentrated sun radiation requires more efficient heat removal methods. Moreover, the collected heat could be recycled for later applications instead of energy dissipation to the environment. Therefore, it is highly desirable to find a cooling fluid that has a superior heat transfer performance over convectional ones, and to analyze the heat transfer characteristics for both CPV cooling and waste-heat recycling.

1.3 Thesis Overview

This thesis has two parts. In the first part, an existing model of nanofluid thermal conductivity based on Brownian motion, i.e., the F-K model (Kleinstreuer & Feng, 2012), will be improved to better explain the experimentally observed enhancement. In the second part, the model developed in the first part will be used for a numerical study of nanofluid heat transfer characteristics with applications to thermal analyses of a CPV/T system.

Specifically, Chapter 2 provides the derivation of the improved F-K model by incorporating nanoparticle aggregation effects and interfacial thermal resistance, in addition to the Brownian motion induced "micro-mixing" effect. The new thermal conductivity expression still consists of a static part and a micro-mixing part. However, the static part is a modified expression of the Maxwell model, with aggregate units replacing the nanoparticles. In addition, the micro-mixing part is simplified from the F-K model by neglecting the inter-particle surface forces. The new k_{nf} model predictions for different nanoparticles in water were then compared with selected experimental data sets.

In Chapter 3, the new k_{nf} model was first used to analyze the performance of nanofluid cooling of CPV cells. The effects of different parameters (i.e., inlet temperature, inlet Reynolds number, and channel height) on the cell efficiency were investigated. An analysis of entropy-generation minimization was employed to determine an optimal geometric configuration and best operational conditions. Then the performance of nanofluid in the heat recycling part was examined and compared with that of water, using a counter-flow double-tube heat exchanger. Again, the effects of different parameters on the thermal performance of the heat exchanger were investigated and an analysis of entropy generation minimization was

conducted for different nanofluid inlet Reynolds number, inlet temperature, and nanoparticle volume fraction.

1.4 Motivation

Dispersing millimeter- or micrometer-size particles in a base liquid has long been a method to enhance the thermal conductivity of a coolant. Recent developments in nanotechnology have enabled the preparation of nanofluids that are able to overcome many of the shortcomings of conventional particle suspensions in cooling applications, such as filter/channel clogging and particle settling. Hence, with experimentally confirmed augmented thermal conductivities (see Sect. 1.6), nanofluids are considered to be promising coolants. However, the mechanisms that cause this enhancement are still under debate. Because of this, a reliable model based on sound physics for the prediction of nanofluid thermal conductivities, k_{nf}, is still unavailable. Though different models have been proposed, considering different mechanisms, no single mechanism can explain the enhancement. Instead, the combined effect of nanoparticle aggregation and Brownian motion induced micro-convection in addition with interfacial thermal resistance can provide a satisfying explanation. For example, Kleinstreuer & Feng (2012) developed a k_{nf} theory (i.e., the F-K model) based on Brownian motion induced micro-mixing. However, they did not consider the nanoparticle aggregation effect as well as the interfacial thermal resistance. Hence in the present study, we improve the F-K model by including these additional effects.

The low heat transfer performance of conventional fluids (typically water) used in CPV systems may keep heat exchanger efficiencies too low or even cause dangerously high system temperatures. Employing a nanofluid with an enhanced thermal conductivity could lead to improved energy efficiencies and smaller systems with lower capital costs. Hence it is necessary to examine the thermal performance of nanofluids in cooling of CPV cells as well

as the recycling of the heat collected in the cooling section. In addition, in order to optimize system performance with minimal cost, entropy generation should be analyzed as well.

1.5 Research Objectives and Novel Results

The research objectives of the current study are:

- Identification of important mechanisms for enhanced thermal conductivity of nanofluids.
- Derivation of a novel model for nanofluid thermal conductivities.
- Evaluation of the thermal performance of nanofluids as applied to cooling and heat recycling systems.
- Performance estimation and entropy analysis of nanofluid flow, leading to the improvement of the overall efficiency of a combined concentration photovoltaic-thermal system.

The novel contributions of the current study are:

- Improved F-K model by including aggregation effects and interfacial thermal resistance. Specifically, the new model reduces the correlation factor in the F-K model from 38 to around unity; the new model compares better with experiments in terms of k_{nf}/k_{water} *vs.* φ; and the new model is applicable to a broader range of conditions, i.e., up to 10% in volume fraction, up to 80nm in particle diameter, and up to 350K in mixture temperature.
- A first-time numerical investigation of the performance of nanofluid flow in a combined concentration photovoltaic-thermal system, using a reliable thermal conductivity model.

1.6 Nanofluid Heat Transfer Properties

1.6.1 Experimental observations

Nanofluids are a new class of heat transfer fluids by dispersing nanometer-sized particles with typical length scales on the order of 1 to 100 nm in traditional heat transfer fluids. Experiments have confirmed that at very low volume concentrations of nanoparticles (i.e., less than 5%) there is a measurable enhancement in thermal conductivity over the base fluid alone, e.g., water, ethylene glycol, or oil (Kleinstreuer & Feng, 2011). Various experimental methods have been developed to measure the thermal conductivities of nanofluids with different accuracies. For example, the Transient Hot Wire (THW) method was widely used over the few years after Eastman et al. (1997) published the pioneer paper. However, the THW method was found to give contradictory results due to the unavoidable convective effects (Hong et al., 2011). To overcome such limits, alternative methods have been introduced, including the thermal-lensing measurement method (Rusconi et al., 2004; Rusconi et al., 2006), the forced Rayleigh scattering method (Venerus et al., 1999; Venerus et al., 2006), the optical beam deflection technique (Putnam & Cahill, 2004; Putnam et al., 2006), among others. It was found through the experimental investigations that the effective thermal conductivity (k_{eff}) could be affected by several parameters, i.e., nanoparticle material, particle volume fraction, particle size, particle shape, particle aggregation, basic fluid properties, temperature, and pH value (Yu et al., 2008).

1.6.1.1 k_{nf} *vs.* temperature (T)

Both temperature dependent and temperature independent nanofluid thermal conductivity have been reported during the past decade or so. For example, the independent studies of (Buongiorno et al., 2009; Colangelo et al., 2012; Kole & Dey, 2012; Li et al., 2008; Putnam et al., 2006; Rusconi et al., 2006; Shima et al., 2010; Turgut et al., 2009) reported various nanoparticle-base fluid pairings with a large range of nanoparticle sizes under different volume fractions, all of which showed no obvious increase of thermal conductivity with temperature. However, many of the investigations used optimal measurement methods instead of the THW method for the thermal conductivity measurement, implying that the measured augmentation of k_{nf} with temperature may be due to the convection effect affiliated with the THW method (Hong et al., 2011). On the other hand, some studies found that at low volume concentrations, k_{nf}/k_{bf} shows no trend of augmentation, and sometimes even decrease with the increase of temperature; while at higher volume fractions, a positive correlation with temperature emerged (Lee et al., 2012; Sundar et al., 2012). Still, a lot of researches have shown increase in thermal conductivity ratio with temperature (Das et al., 2003; Karthik et al., 2012; Li & Peterson, 2006; Li & Peterson, 2007a; Sundar et al., 2013) . Some of the most recent experimental measurements are displayed in Fig. 1.3.

It should be noted that the increase of absolute values of k_{nf} with temperature is evident in most studies. Therefore, some attribute the increased k_{nf} to the increase of base fluid thermal conductivity with temperature. On the other hand, it was argued that as the nanofluid viscosity declines when the temperature increases, while at the same time the Brownian

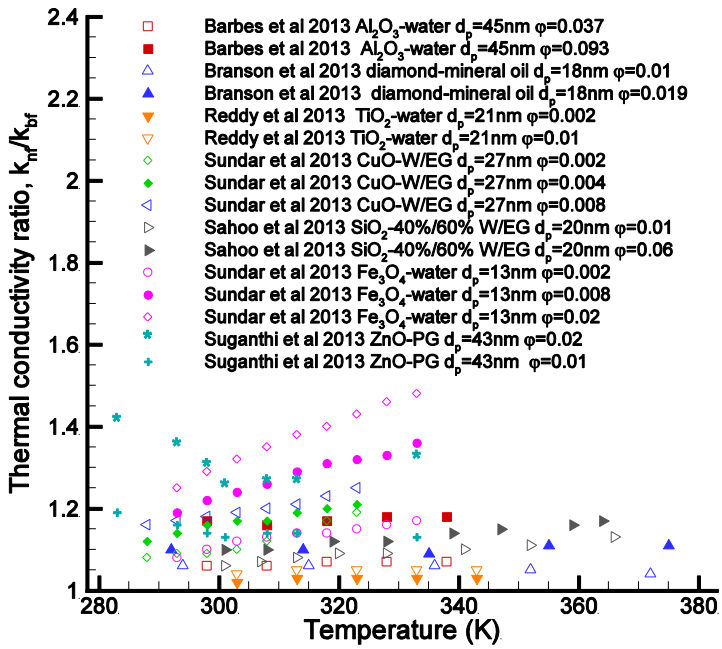

Figure 1.3: Recent experimental data of nanofluid thermal conductivity as a function of temperature T

motion of particles intensifies, the nanofluid thermal conductivity should increase. Yet it was also reported that the average hydrodynamic size of nanoparticle aggregates increases with temperature. Because of all the conflicts in the literature, more careful and deliberate experimental studies are required in the future.

1.6.1.2 k_{nf} *vs.* volume fraction (φ)

Various groups have published a large volume of experimental data concerning the effect of nanoparticle volume fraction on the effective thermal conductivity of nanofluids. It may be safe to conclude now that the thermal conductivity increases with volume fraction, as has been observed by almost all research groups. However, the rate of increase of k_{nf} with

respect to φ has not shown the same functional dependence among the different studies. Both linear dependence (Xie et al., 2002a; Yu et al., 2011) and non-linear dependence (Pang et al., 2012; Paul et al., 2012) of thermal conductivity on volume fraction have been reported for spherical nanoparticles. For nanomaterial with high aspect ratios like carbon nanotubes, the relation is usually non-linear (Chandrasekar et al., 2010; Xie et al., 2003). Moreover, the magnitudes of enhancement of thermal conductivity reported by various studies differ from each other, even under the same experimental conditions, i.e., nanoparticle-base fluid pairing, particle diameter, temperature, and volume fraction. For example, for TiO_2-water nanofluid at room temperature, Yiamsawasd & Wongwises (2012) measured a 12% increase of thermal conductivity over water at 3% volume fraction using transient hot wire method, while Turgut et al. (2009) measured a much meager increase, i.e., just 7% using the 3-ω method.

Recently, the effects of temperature and volume fraction were investigated using a new class of heat transfer fluids as well as nanoparticles. For example, Nieto de Castro et al. (2012) measured the thermal conductivity of multi-wall carbon nanotubes in base ionic liquids (ionanofluid) as a function of temperature and volume fraction. The results show that larger enhancement of thermal conductivity of ionanofluids can be obtained with higher particle concentrations. However, the effect of temperature on thermal conductivity enhancement was found to be insignificant. Liu et al. (2014) used graphene as the dispersed phase in an ionanofluid and measured an enhancement of thermal conductivity by 15.2% to 22.9% at a room temperature of about 20°C and a mass concentration of 0.06%. Also, thermal conductivity behavior of non-Newtonian fluid based nanofluids has been reported

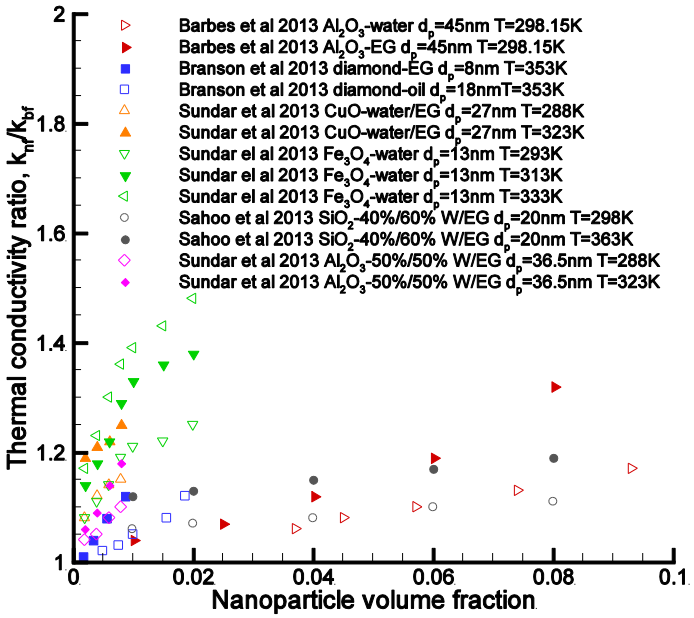

Figure 1.4: Recent experimental data of nanofluid thermal conductivity as a function of volume fraction φ

(Maciej et al., 2013; Yang et al., 2012). Some of the most recent measurements on the relationship between k_{nf} and φ are shown in Fig. 1.4.

In summary, despite the inconsistencies, higher particle volume fractions give larger thermal conductivity enhancements. The increase rate differs between different studies and is highly dependent on the experimental conditions. Further experiments should be conducted under more consistent conditions.

1.6.1.3 k_{nf} *vs.* particle size (d_p)

Particle size affects the thermal conductivity of nanoparticles mainly through two possible mechanisms. First, more rigorous Brownian motion is encountered by smaller particles,

hence stronger particle-particle as well as particle-base fluid interactions can be expected, which enhance the effective thermal conductivity. Second, for the same mass fraction, smaller nanoparticles drastically increase the total surface area for heat transfer.

Again, there has been controversy over the relationship between particle size and nanofluid effective thermal conductivity. By comparing a few experimental results, Yu et al. (2007) concluded that larger particle diameters produce a larger enhancement in thermal conductivity. Timofeeva et al. (2010) reported data for nanofluids with 16-90nm α-SiC nanoparticles. According to their observations, larger particles of the same material and volume fraction provide higher thermal conductivities. This trend was also confirmed by Beck et al. (2009), using alumina nanoparticles 8-282nm in diameter dispersed in water and ethylene glycol. In contrast, other researchers (Colangelo et al., 2012; Kim et al., 2007; Li & Peterson, 2007a; Moghadassi et al., 2010; Paul et al., 2012) provided an opposite trend, i.e., an inverse dependence of thermal conductivity enhancement on particle diameter.

The nanoparticle aggregation effects may provide some clue on explaining these conflicting results. As smaller particles are more likely to form aggregates, they exist in the base fluid essentially as clusters in the absence of electric surface charge, batch mixing, etc.. Clusters are usually not as compact as single particles, i.e., they are having voids that are not filled with particles; thus, weakening the Brownian motion effect. However, one can still argue that the form of chains of particles, forming “solid bridges”, facilitate the transport of heat, therefore enhancing the thermal conductivity.

Because of the difficulty of direct observation and measurement of the effect of aggregation, a final conclusion cannot be made at this point. Yet this holds the key to a better

understanding of the relationship between nanoparticle size and thermal conductivity enhancement, as clearly demonstrated with carbon nanotubes.

1.6.1.4 k_{nf} *vs.* pH

Although most of the earlier works have not shown the pH values of the nanofluids used in the measurement of thermal conductivity, recent experimental studies have addressed this parameter effect. By changing the pH of the solution the surface charge density and surface potential that can be reflected by the zeta potential can be controlled. The value of thermal conductivity ratio k_{nf}/k_{bf} dependents on the difference between the pH of the solution and the isoelectric point of particles (the pH values at which the zeta potential is zero, meaning no repulsive force between particles). As the pH departs further away from the isoelectric point, k_{nf}/k_{bf} becomes larger (D. Lee et al., 2006; Xie et al., 2002b)Lee et al., 2006; Xie et al., 2002). In other words, k_{nf}/k_{bf} increases with the absolute value of the zeta potential on particle surfaces, which may point to an optimal value of pH for nanofluids (Zhu et al., 2009). (Lee et al., 2006) proposed that the charged surface site facilitates heat transport by providing a more effective passage through which heat carriers move. Another important aspect to be considered is that nanoparticle aggregation and nanofluid stability is directly related to the pH value. Moreover, the formation of electrical double layer (EDL) on nanoparticles due to the existence of ions enhances the Brownian motion through the Coulomb force (Iranidokht et al., 2013; Jung & Yoo, 2009).

The experimental evidence on particle size and pH value of the mixture suggests that the aggregation effect is a key factor that affects the mechanism of heat transfer in nanofluids at

the micro-scale. Hence, it is necessary to consider this effect when measuring and explaining the macroscopic character of nanofluids, i.e., k_{nf} *vs.* T and k_{nf} *vs.* φ .

1.6.1.5 Other factors

A number of other parameters have been found to affect thermal conductivity enhancement of nanofluids; for example, base fluid properties, particle shape, sonication, etc..

The enhancement of thermal conductivity of the base fluid is found to depend on the thermal conductivity of the base fluid itself. For example, (Xie et al., 2002) found that for a particle loading of 5%, pump oil, ethylene glycol, and deionized water show maximum enhancements of 38%, 29.5% and 22.2%, respectively. Therefore they suggested that there might be an inverse relationship between the enhancement of thermal conductivity and the thermal conductivity of base fluid itself. Timofeeva et al. (2011) reported lower enhancement of thermal conductivity of SiC-water nanofluids as compared to SiC-EG/water nanofluids for the same nanoparticle size. They proposed that the difference may be due to lower value of the interfacial thermal resistance between nanoparticles and EG/water mixture. Others (Khedkar et al., 2012; Moghadassi et al., 2010) found opposite results. They suggested that base fluids with lower viscosities favor particle Brownian motion and particle interaction, hence have larger thermal conductivity enhancement. Also layered structure of base fluid molecules at the nanoparticle surface may be another reason. Recently Shima & Philip (2014) measured hexadecane and kerosene based Ag and Fe_2O_3 nanofluids with average diameter of 7nm and concluded that the thermal conductivity of nanoparticle does not influence the *k* enhancement in stable nanofluids at low particle loading.

Proper preparation of stable nanofluids is a key issue in nanofluid research. Ultra-sonication has been used to break large aggregations and obtain a stable suspension. However, ultra-sonication time varied from less than hour to a few days among different studies (Haddad et al., 2014). It was found that thermal conductivity of nanofluids increases with sonication time until certain limit (Khedkar et al., 2012; Kole & Dey, 2012; LotfizadehDehkordi et al., 2013; Yang et al., 2012). Lee et al. (2008) found that extending sonication time produced more stable suspensions; although good dispersion with little aggregates was already observed after 5h sonication. Clearly, it is important to have long enough sonication before measuring the properties of nanofluids.

The thermal conductivity enhancement of nanofluids is also affected by particle shape, as reported by a number of studies (Elias et al., 2014; Jeong et al., 2013; Murshed et al., 2005; Timofeeva et al., 2009). Nanofluids with non-spherical nanoparticles usually have higher thermal conductivity enhancement compared with spherical nanoparticles suspension at the same volume fraction. Especially elongated nanoparticles generate the largest enhancements. In fact, nanofluids with carbon nano-tubes (CNTs) usually show much higher thermal conductivity enhancement than spherical particles. This may be because of the much higher total surface area of CNTs than spheres at the same volume fraction and that CNTs are more likely to form aggregations.

In conclusion, it has been found that a number of factors would affect the enhancement of thermal conductivity of nanofluids. However, no general consensus has been reached qualitatively or quantitatively on the behavior of k_{nf} under different conditions. The microscopic behavior of nanoparticles like aggregation and Brownian motion make it

difficult to conduct direct observations and measurements of these effects. Clearly, future experiments should focus on the *microscopic* behavior of nanoparticles in order to have a better understanding of the characteristics as well as underlying mechanisms of the enhanced thermal conductivity of nanofluids.

1.6.2 Theoretical models

The effective thermal conductivity of particle-liquid mixtures have long been developed (Maxwell, 1881) and continuously improved for various situations based on the effective medium theory (Bruggeman, 1935; Davis, 1986; Garnett, 1906; Hamilton & Crosser, 1962; Jeffrey, 1973; Leal, 1973). The key underlying assumptions for all of these theoretical approaches is the diffusion-like heat transfer in both the components of the mixture, stationary state of particles, and mono-dispersity of particles in the liquid. However, as these models predict micrometer or larger-size multi-component mixtures, they usually fail to predict the thermal conductivity of nanofluids. Experimental results for nanofluid thermal conductivity indicate a significant underestimation when using the models based on the effective medium theory.

Keblinski et al. (2002) proposed four possible explanations for the anomalous increase of the thermal conductivity of nanofluids, i.e., Brownian motion of particles, molecular-level layering of the liquid at the liquid/particle interface, ballistic heat transport in the nanoparticles, and the effects of nanoparticle clustering. There have been a number of models developed over the years to address each of the four mechanisms or combined mechanisms, with quite a few review articles summarizing the pros and cons of them. Since we believe

that the enhanced thermal conductivity originates from the micro-mixing caused by nanoparticle Brownian motion and the clustering of nanoparticles, we narrowed the literature review of theoretical models based on these two effects.

1.6.2.1 Brownian models

Though there have been opponent voices to the effectiveness of Brownian motion on enhancing the thermal conductivity of nanofluids (Evans et al., 2006; Keblinski et al., 2002; Wang et al., 1999), it still remains a physically sound mechanism to explain the anomalous augmentation.

The mere existence of particles in a fluid matrix can promote the thermal conductivity of the fluid. This has been well studied in a number of works starting with Maxwell (1881). For nanofluids, additional enhancement is realized due to the vigorous random motion of nanoparticles as a result of the collisions with randomly moving fluid molecules, i.e., Brownian motion.

Jang & Choi (2004) suggested that the vigorous Brownian motion of nanoparticles produces convection-like effects at the nano-scale, which translate into conduction at the macro-scale. The resulted k_{nf} has three parts

$$k_{nf} = (1-\varphi)k_{bf} + k_{peff}\varphi + 3C_1 \frac{d_{bf}}{d_p} \varphi k_{bf} \, \mathrm{Re}_{d_p}{}^2 \, \mathrm{Pr} \tag{1.1}$$

where C_1 is a constant, d_{bf} is the base fluid molecule diameter, and Re_{d_p} is the Reynolds number based on nanoparticle diameter. The first term on the right hand side of the equation is due to heat transfer through base fluid, the second term is due to heat transfer inside particles, and the third term is due to micro-convection induced by nanoparticle Brownian

motion. The Brownian motion velocity of nanoparticles can be determined using Einstein's diffusion coefficient. Though this model considers convection like heat transfer between particles and the base fluid, the micro-mixing effect induced by the particle random motion was neglected. Moreover, as pointed out by Kleinstreuer & Li (2008), this model is inconsistent and has limited accuracy in predicting the thermal conductivity of nanofluids.

In an attempt to consider the Brownian motion effect, Kumar et al. (2004) used the kinetic theory of heat flow and assumed the thermal conductivity due to Brownian motion is proportional to the average velocity of particles. However, this assumption has little justification. Moreover, based on the model, the calculated enhancement ratio due to Brownian motion is on the order of 10^{-6} for Au-water nanofluid with 1% volume fraction (Bastea, 2005), which can be safely ignored.

Prasher et al. (2005) proposal a semi-empirical model incorporating both Brownian motion induced micro-convection effect and the interfacial resistance. The convection contribution of a single particle is given by the analytical solution provided by Acrivos & Taylor (1962), while the thermal contact resistance is considered by modifying the Maxwell-Garnett model as:

$$\frac{k_{nf}}{k_{bf}} = (1 + A\mathrm{Re}^{m}\,\mathrm{Pr}^{0.333}\,\varphi)\left(\frac{[k_p(1+2\alpha)+2k_m]+2\varphi[k_p(1-2\alpha)-k_m]}{[k_p(1+2\alpha)+2k_m]-\varphi[k_p(1-2\alpha)-k_m]}\right) \tag{1.2}$$

where $\alpha = 2R_b k_m / d_p$ is the nanoparticle Biot number, R_b is the thermal contact resistance. The intensity of micro-convection effect due to multi-particles and the magnitude of the interfacial resistance were both determined by matching experimental results. Kleinstreuer &

Li (2008) pointed out that the model has a very narrow application range in terms of particle diameter, and the semi-empirical nature of the model will inevitably require curve-fitting.

Koo & Kleinstreuer (2004) postulated that the enhanced thermal conductivity is mainly due to Brownian motion induced micro-mixing. Specifically, a particle under Brownian motion brings with it a portion of the fluid adjacent to it. The perturbation to the fluid thus creates a convection-like micro-effect between fluid fields with higher and lower temperatures, thereby enhancing the thermal conductivity of the mixture. They considered a model comprised of two parts:

$$k_{nf} = k_{\text{static}} + k_{\text{Brownian}} \tag{1.3}$$

where k_{static} is due to the higher thermal conductivity of nanoparticles and can be determined by the Maxwell model

$$k_{static} = k_{bf} \cdot \left(1 + \frac{3\left(\frac{k_p}{k_{bf}} - 1 \right)\varphi}{\left(\frac{k_p}{k_{bf}} + 2 \right) - \left(\frac{k_p}{k_{bf}} - 1 \right)\varphi} \right) \tag{1.4}$$

and k_{Brownian} is due to the perturbation of particles to the base fluid which induces velocity components. The induced velocity field was calculated using the solution for Stokes flow around a sphere and the affected fluid volume was determined using the 99% criterion of vanishing impact. The final expression was given by

$$k_{Brownian} = 5\times 10^4 \beta\varphi\left(\rho c_p\right)_{bf} \times \sqrt{\frac{\kappa_B T}{\rho_p d_p}}\, f(T,\varphi) \tag{1.5}$$

where β and $f(T,\varphi)$ are two empirical functions. This model takes into account the effects of temperature, volume fraction, and particle size dependence as well as type of nanoparticle and base fluid combinations. Later Li & Peterson (2007b) provided simulation evidence that this mixing effect can have a significant influence on the effective thermal conductivity of nanofluids.

Li & Kleinstreuer (2008) modified the model of Koo & Kleinstreuer (2004) by incorporating the interfacial thermal resistance between particles and base fluids, and combining the functions beta and f into a new g-function which considers the influence of multi-particle interaction. In the modified model, k_{Brownian} has an expression of

$$k_{Brownian} = 5\times 10^4 \varphi \left(\rho c_p\right)_{bf} \times \sqrt{\frac{\kappa_B T}{\rho_p d_p}} g(T,\varphi,d_p) \tag{1.6}$$

where $g(T,\varphi,d_p)$ has the form

$$\begin{aligned} g(T,\varphi,d_p) = (a + b\ln(d_p) + c\ln(\varphi) + d\ln(d_p)\ln(\varphi) + e\ln(d_p)^2)\ln T + \\ (g + h\ln(d_p) + i\ln(\varphi) + j\ln(d_p)\ln(\varphi) + k\ln(d_p)^2) \end{aligned} \tag{1.7}$$

where a-k are the empirical coefficients based on the type of particle-liquid pairing.

The original k_p in Eq. (1.4) becomes k_{peff}

$$R_f + \frac{d_p}{k_p} = \frac{d_p}{k_{peff}} \tag{1.8}$$

Here $R_f = 4\times 10^{-8}\,\mathrm{K\cdot m^2 W^{-1}}$ is the interfacial resistance. In this model, the base fluid properties are also functions of temperature.

Based on the Langevin equation for random particle motion, Xuan et al. (2006) proposed a thermal fluctuation equation to describe the stochastic temperature variation of the nanoparticles. The superposition principle and the Green-Kubo theorem was applied to derive the explicit expression for k_{Brownian}. Particles are assumed to be spherical and well dispersed.

In an approach similar to that of Koo & Kleinstreuer (2004), Yang (2008) also decomposed k_{nf} into a static part and a Brownian motion part, and focus on the Brownian motion within one time interval to calculate the thermal energy flow due to perturbation velocity. The author suggested that since the Langevin equation does not consider the fluid inertia around the particles, the relaxation time for particle Brownian motion can only be determined in a semi-empirical way.

On the other hand, Shukla & Dhir (2008) considered the interaction force between particles and the Brownian force on the particle to determine the particle velocity in the base fluid. Then assuming small departure from equilibrium and pairwise additive interaction potential between particles, the Brownian contribution to the heat flux was calculated to give the expression of $k_{Brownian}$. The inter-particle potential was calculated using the DLVO theory for colloidal dispersions. However, the assumption for pairwise additive inter-particle potential has little justification, because the effective range of this potential is limited to the case of small particle separation. In this case strong particle interaction would lead to aggregation. Yet the model assumed that particles are well separated and hydrodynamic interactions among particles are negligible.

Recently, Kleinstreuer & Feng (2012) developed a k_{nf} model which considers random temperature and velocity fluctuations as conceived by Reynolds for turbulent flow. It encapsulates various effects, such as Brownian motion induced nanoparticle fluctuation, particle-particle interaction, and particle-base fluid interaction. In this model, each nanoparticle induces a velocity field in the surrounding base fluid, and the induced fluctuation velocities are superimposed to realize multi-particle effects. With this induced velocity, the Reynolds-averaged heat transfer equation is solved to give the expression of k_{mm}, the dynamic part of the effective thermal conductivity of nanofluids, k_{nf}

$$k_{mm} = 49500 \cdot \frac{\kappa_B \tau_p}{2m_p} \cdot C_c \cdot (\rho c_p)_{nf} \cdot \varphi^2 \cdot (\bar{T} \ln \bar{T} - \bar{T}) \cdot \frac{\exp(-\xi \omega_n \tau_p) \sinh\left(\sqrt{\frac{(3\pi\mu_{bf} d_p)^2}{4m_p^2} - \frac{K_{p-p}}{m_p}} \frac{m_p}{3\pi\mu_{bf} d_p}\right)}{\tau_p \sqrt{\frac{(3\pi\mu_{bf} d_p)^2}{4m_p^2} - \frac{K_{p-p}}{m_p}}} \tag{1.9}$$

There have also been a few empirical correlations developed from experimental data that show the relationship between k_{nf} and both T and φ. For example, Chon et al. (2005) gave a correlation based on data measured on Al_2O_3-water nanofluids with volume fraction ranging between 0 and 4%, and working temperature as high as 370K:

$$\frac{k_{nf}}{k_{bf}} = 1 + 64.7\varphi^{0.746} \left(\frac{d_{bf}}{d_p}\right)^{0.369} \left(\frac{k_p}{k_{bf}}\right)^{0.7476} \cdot \mathrm{Pr}^{0.9955}\, \mathrm{Re}^{1.2321} \tag{1.10}$$

where $\mathrm{Pr} = \mu_{bf} / \rho_{bf} \alpha$, $\mathrm{Re} = \rho_{bf} \kappa_B T / 3\pi\mu_{bf}^2 l_{bf}$, in which κ_B is the Boltzmann constant, and l_{bf} is the mean free path of water molecules.

Corcione (2011) provided a correlation based on a variety of experimental data for different kinds of nanoparticles dispersed in water and ethylene glycol (EG), with particle diameter ranging from 10nm to 150nm:

$$\frac{k_{nf}}{k_{bf}} = 1 + 4.4\,\mathrm{Re}^{0.4}\,\mathrm{Pr}^{0.66}\left(\frac{T}{T_{fr}}\right)^{10}\left(\frac{k_p}{k_{bf}}\right)^{0.03}\cdot\varphi^{0.66} \tag{1.11}$$

where Re is the nanoparticle Reynolds number, $\mathrm{Re} = 2\rho_{bf}\kappa_B T \big/ \pi\mu_{bf}^2 d_p$, Pr is the Prandtl number of the base liquid, T is the nanofluid temperature, T_{fr} is the freezing point of the base liquid, k_p is the nanoparticle thermal conductivity. This correlation is applicable to nanoparticle volume fractions in the range from 0.2% to 9%, temperatures from 294K to 324K. Figure 1.5 shows the comparison between the empirical correlations and recent experimental data.

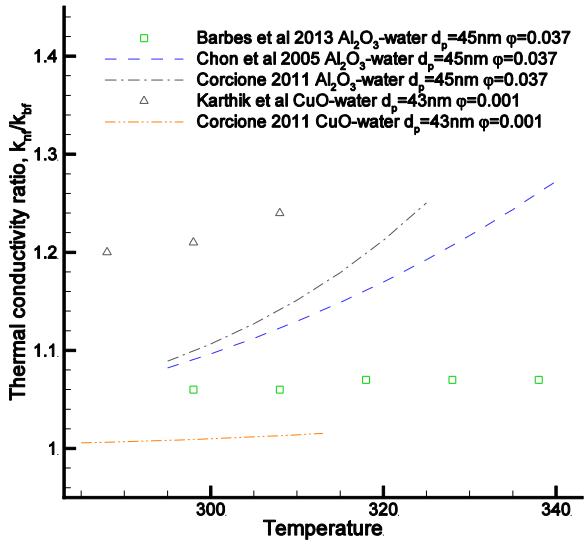

Figure 1.5: Comparisons between empirical correlations and recent experimental data on nanofluid thermal conductivity as a function of temperature. Clearly, only poor agreement was obtained.

In a more recent study, Mallick et al. (2013) compared a number of models for thermal conductivity of nanofluids in terms of matching a selective experimental data. By comparing with the results of Longo & Zilio(2011), they suggested that better agreement can be obtained using cluster size in the model of Koo & Kleinstreuer (2004) compared to nominal particle size, indicating the need to consider the aggregation effect.

1.6.2.2 Aggregation models

The particles move independently under Brownian motion until they come close enough for the van der Waals forces to become important and result in a stick-together. Particles may repel each other several times due to the electrostatic barrier before actually joining into an aggregate (Gharagozloo & Goodson, 2011). Under the action of these forces, the randomly moving particles tend to aggregate in order to minimize the surface energy of the whole system.

Nanomaterials are commonly manufactured with surface coatings (e.g., surfactants, polymers, and polyelectrolytes) to enhance dispersion stability, i.e., by increasing surface charge and electrostatic repulsion or by reducing interfacial energy between particle and solvent (Rosen & Kunjappu, 2012). Moreover, procedures like sonication, magnetic stirring, or adding surfactants to the mixture were used to weaken the aggregation effect. However, through SEM (scanning electron microscope) observations, many experiments suggest that aggregation formation is inevitable. Therefore the aggregation effect has been another aspect that has inspired many studies.

Since the thermal conductivity of nanoparticles is usually orders of magnitude higher than that of the base fluid, the heat transfers much more rapidly through the particles when

compared to the base fluid. The aggregates provide a bridge for the rapid heat transport through particles in close contact with each other. Hence, despite the risk of forming very large agglomerates that sediment out of the fluid, the formation of relatively small aggregates actually enhance the heat transport rate.

Wang et al. (2003) introduced a model to describe the aggregation effect of nanofluids using a fractal model for the cluster structure. The effective thermal conductivity of a cluster is determined by the Bruggeman model (Bruggeman, 1935) because of its ability to consider large volume fraction dispersions, where a log-normal function is used to provide the size distribution of clusters. Then the effective thermal conductivity of clusters and the size distribution function are substituted into a multi-component Maxwell-Garnett (Garnett, 1906) model to obtain the effective thermal conductivity of nanoparticle suspension. Wang et al. (2003) also indicated an increase in the fractal dimension with volume fraction.

Xuan et al. (2003) conducted an aggregation simulation and found that the aggregation structure of Cu-water nanofluid has a fractal like feature. They assumed separable contribution from the mere addition of particles into the base fluid, and from the random motion of aggregates, and proposed a model which is comprised of two parts: the thermal conductivity due to effective medium theory and the thermal conductivity that combines the aggregation effect and the Brownian motion effect:

$$\frac{k_{eff}}{k_f} = \frac{k_p + 2k_f - 2\phi(k_f - k_p)}{k_p + 2k_f + \phi(k_f - k_p)} + \frac{\rho_p \phi c_p}{2k_f}\sqrt{\frac{k_B T}{3\pi r_c \mu}} \tag{1.12}$$

where the first term on the right hand side of the equation is the Maxwell model and the second is due to Brownian motion of aggregates. A quick examination of the expression

reveals a problem with this model: given that the nanoparticles are assumed to aggregate and form clusters of size r_c, the Maxwell model is still used which assumes perfect dispersion.

Xu et al. (2006) considered the Brownian motion induced micro-convection in the thermal boundary layer near the particles. However the thickness of the boundary layer is determined by matching experimental data. To take particle aggregation into consideration, they assumed a particle size distribution that obeys the power law. The ratio of largest and smallest fractal cluster size was given to be 10^{-3} without further justification. The proposed model is expressed as a function of the average size of nanoparticles, fractal dimension, volume fraction, temperature, and fluid properties. The model predicted a critical concentration above which k_{nf}/k_{bf} decreases with the increase in concentration, which indicates weakened Brownian motion effect.

Prasher et al. (2006) added the aggregation effect into the Brownian motion micro-convection model (Prasher et al., 2005) with the aggregation structure again depicted by the fractal theory. For modeling the contribution of the aggregated system, they adopted the approach of Wang et al. (2003). On the other hand, Evans et al. (2008) built a three-level homogenization model to describe the particle aggregates which also considers the thermal contact resistance (see Fig. 1.6). The aggregate is decomposed into a backbone which has a fractal structure, and dead-ends with the fluid, which has an effective thermal conductivity calculated by the Bruggeman model. The effective thermal conductivity of the aggregate sphere k_a is determined using the model of Nan et al. (1997) and then replace the thermal conductivity of particle in the Maxwell-Garnett model to give k_{nf}. The authors claim that

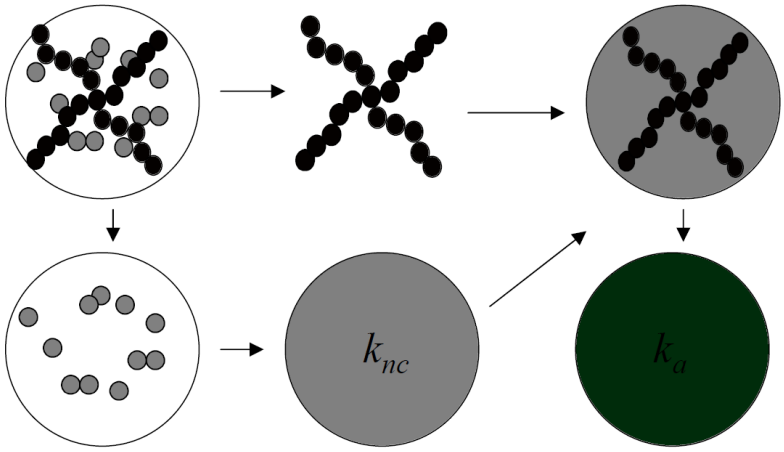

Figure 1.6: Three-level homogenization model described in Evans et al. (2008)

aggregation of nanoparticles contributes to the enhanced thermal conductivity of the nanofluid while the interfacial thermal resistance impedes the enhancement. A similar approach was adopted by Chen et al. (2009) and Gharagozloo & Goodson (2011).

Recently, Nabi & Shirani (2012) modified the model proposed by Koo & Kleinstreuer (2004) to include the aggregation effect. The description of the clusters is similar to that adopted by Prasher et al (2006). The simultaneous effects of Brownian motion induced micro-mixing and aggregation kinetics of nanoparticles were taken into consideration.

1.6.2.3 Thermal contact resistance

For the transport of energy across interfaces between two phases, continuum theory usually assumes continuity of both the heat fluxes and the temperatures. The latter assumption, however, has little theoretical foundation, and is known to work only at the macroscopic scale. In fact, the discontinuity in temperature drop across an interface has been discovered

and further proved decades ago (Kapitza, 1941). This discontinuity arises from the combination of a poor mechanical or chemical adherence at the interface and a mismatch in the coefficients of thermal expansion (Hasselman & Johnson, 1987).Thermal contact resistance, or interfacial resistance, which refers to the temperature discontinuity at the solid-liquid interface that equivalent to an additional thermal resistance, has significant influence on the thermo-physical properties on the mixture (Barrat & Chiaruttini, 2003; Hasselman & Johnson, 1987).

A consistent description of transport process across an interface should allow for a jump in the temperatures between the two phases, proportional to the heat flux (Barrat & Chiaruttini, 2003). This can be expressed as

$$\vec{J}_E \cdot \vec{n} = \frac{T_1 - T_2}{R_K} \tag{1.13}$$

where $\vec{J}_E$ is the heat flux and $\vec{n}$ is the direction perpendicular to the interface, R_K is the Kaptiza resistance (thermal contact resistance) of the interface, whose existence was pointed out by Kapitza in the context of liquid helium physics (Kapitza, 1941). It is common to express the thermal contact resistance in terms of a length scale:

$$A_K = R_K k_{bf} \tag{1.14}$$

where A_K is the Kapitza length, which is the thickness of the base fluid material equivalent to the interface from a thermal point of view (see Fig. 1.7).

Thermal contact resistance has been considered by most theoretical models for effective thermal conductivity of nanofluids. However, the prominent issue related to this effect is the value of the equivalent resistance, R_b. Scattered values have been adopted in the literature

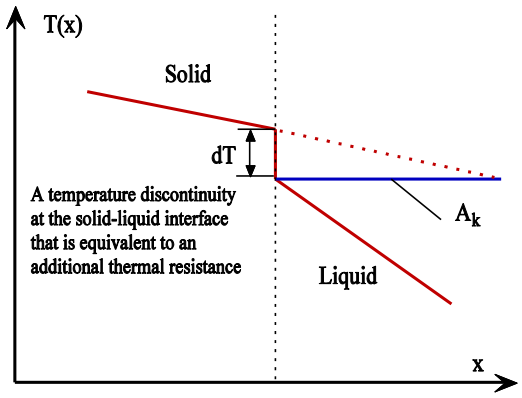

Figure 1.7: Illustration of interfacial thermal resistance

spanning two orders of magnitude, i.e., $O(0.1)\times10^{-8}$ K·m^{2}W^{-1} to $O(10)\times10^{-8}$ K·m^{2}W^{-1} (J. Li & Kleinstreuer, 2008) for R_b. For example, Timofeeva et al. (2007) suggested 0.2×10^{-8} K·m^{2}W^{-1} for alumina-water interface, Prasher et al. (2005) $0.25\text{-}2.5\times10^{-8}$ K·m^{2}W^{-1} to match different experimental data, Li & Kleinstreuer (2008) chose an average value of 4.0×10^{-8} K·m^{2}W^{-1}.

Since the reason for this phenomenon is believed to be poor mechanical or chemical adherence of liquid molecules at the interface, and a thermal expansion mismatch, the value is consequently a function liquid molecule structures, solid and liquid physical properties, and the hydrophobic or hydrophilic nature of the solid surface. In fact, many have suggested large effect of different R_b value on the model prediction of k_{nf} (Hasselman & Johnson, 1987; Nan et al., 2004; Prasher et al., 2005; Shenogin et al., 2004). Typically, the particle size is an important parameter when evaluating the effect of thermal contact resistance which can be seen from the function

$$R_f + \frac{d_p}{k_p} = \frac{d_p}{k_{peff}} \tag{1.15}$$

Till now, there is no experimental data that suggest proper values for different nanoparticle-base fluid composites. Nevertheless, the importance of thermal contact resistance is widely recognized and this effect should be considered when developing theoretical models for k_{nf} .

1.6.2.4 Summary

A number of theoretical models have been proposed for k_{nf} , accounting for Brownian motion effects, nanoparticle aggregation, and thermal contact resistance. The models were derived via several semi-empirical and/or phenomenological approaches, resulting in different accuracies and ranges of application. It seems that no model can match experimental results for most types of nanofluids. This may be due to the complexities of nano-scale transport phenomena as well as the very different properties of both the nanoparticles and the base fluids. However, it is clear that to have a reliable model based on sound physics that predicts accurate k_{nf} values, all of the three listed effects should be considered.

1.7 Nanofluid Turbulent Convection Heat Transfer

The superior thermal conductivity of a nanofluid over its base fluid indicates potential applications in the field of convective heat transfer. Over the past decade or so, the heat transfer and pressure drop characteristics have been studied extensively for *laminar* nanofluid flow regimes, while fewer can be found addressing turbulent nanofluid flow. However, in many practical applications turbulent flow is usually required to deal with high heat fluxes, e.g., cooling of concentration photovoltaic cells. Therefore we give a brief discussion of the nanofluid convective heat transfer performance focusing on the turbulent flow regime.

1.7.1 Experimental data and correlation for nanofluid flows

In comparing the performance of turbulent convective heat transfer between nanofluid and the base fluid, a proper comparison base and a meaningful parameter of merit are necessary. The latter is the quantity used to measure the convective heat transfer performance and to determine the utility of a nanofluid relative to its base fluid. The comparison base specifies the condition under which parameters of merit are evaluated (Yu et al., 2012). To assess the convective heat transfer performance of nanofluids, flow velocity, and pumping power are two proper bases while the Reynolds number is not, because it completely ignores the pumping power penalty effect. The convective heat transfer coefficient is preferred over the Nusselt number as the parameter of merit. This is because the Nusselt number is the ratio of convective to conductive heat transfer, and a low Nu may mean either low convective heat

transfer coefficient or high thermal conductivity, making it ambiguous in evaluating the convective heat transfer performance of nanofluids.

Unfortunately, the comparison bases and parameters of merit used in the literature for the convective heat transfer performance of nanofluids are not always the same. In fact, the Nusselt number has been frequently used, making it difficult to obtain the conclusion on whether the nanofluids are superior to the base fluid in terms of convective heat transfer performance. Nevertheless, the existing experimental results do provide some characteristics of the convective heat transfer performance of nanofluids, which are summarized next.

1.7.1.1 Turbulent convective heat transfer coefficient

For turbulent convective heat transfer, elevated, unchanged and reduced h_{nf} values have all been reported in comparison to h_{bf} . No consensus has been reached as of whether the dispersion of nanoparticles in the base fluid enhances the convective heat transfer. However, most studies which found elevated h_{nf} values also reported increased convective heat transfer coefficients with increased nanoparticle loadings. Another widely recognized character is the nanoparticle size effect on the convective heat transfer coefficient. Larger particles seem to give better h_{nf} results for the same particle volume fractions. A few results are provided here for reference.

Pak & Cho (1998) reported turbulent friction and heat transfer behavior in a tube using alumina-water and titania-water nanofluids. They found that under constant velocity condition the convective heat transfer coefficient for nanofluids is smaller than that for the base fluid.

Li et al. (2003) investigated convective heat transfer and flow features of Cu-water nanofluid in a tube under turbulent conditions, enhanced convective heat transfer coefficients over that of the base fluid were found under constant velocity conditions. Moreover, the enhancement was found to increase with nanoparticle concentration, which was confirmed by Heyhat et al. (2012) for Al2O3–water nanofluids with volume fraction range between 0.1% and 2%.

Williams et al. (2008) tested alumina-water and zirconia-water nanofluids under fully turbulent conditions. The results suggested that if the measured thermo-physical properties of the nanofluids are used in calculating the dimensionless numbers, the existing correlations accurately reproduce the convective heat transfer and viscous pressure loss behavior in tubes. Therefore, they concluded that no abnormal heat transfer enhancement was observed. However, they comparison was made under constant Reynolds numbers.

The effect of nanoparticle concentration on nanofluid turbulent convective heat transfer performance was observed by Timofeeva et al. (2011), where under constant velocity, the SiC-EG/water nanofluid exhibits higher h_{nf} than h_{bf} for 66nm and 90nm particles, yet lower h_{nf} than h_{bf} for 16nm and 28nm particles. Moreover, the convective heat transfer coefficient not only increases with particle size, but also increases with temperature and particle concentration.

Duangthongsuk & Wongwises (2010) studied the heat transfer performance and pressure drop of TiO_2-water nanofluids in a double tube counter-flow heat exchanger with nanoparticle volume fraction ranging from 0.2% to 2%. While a 26% enhancement in heat transfer coefficient over water was measured for 1% volume fraction nanofluid, a 14%

reduction was also found for 2 vol.% nanofluid. The authors attribute this to the higher rate of increase of nanofluid viscosity over that of thermal conductivity with particle concentration. Similarly, Sahin et al. (2013) reported an optimal volume concentration of 1% for Al_2O_3-water nanofluid, and Azmi et al. (2013) reported optimal volume concentration of 3% for SiO_2-water nanofluid with 22nm particle diameter under constant Reynolds number condition.

Fotukian & Nasr Esfahany (2010a; 2010b) measured turbulent convective heat transfer and pressure drop behavior of dilute (φ<0.3%) CuO-water and Al_2O_3-water nanofluids. The results indicate significant increase in heat transfer coefficient. Also, no variation with nanoparticle concentration was observed for this augmentation. However, large penalty in pressure drop was also observed accompanying increased heat transfer coefficient. Moreover, the thermo-physical properties used in the calculation of h_{nf} were themselves calculated from theoretical models instead of direct measurements, which makes the results vulnerable. The results also showed effects of zeta potential (or, effects of aggregation) on the heat transfer performance.

Yu et al. (2009) used silicon-carbide-water suspension consisting of 3.7% volume of 170nm particles for turbulent convective heat transfer measurements. While the convective heat transfer coefficient increased by 50-60% above the base fluid when compared on the basis of constant Reynolds number, it decreased by 7% when constant velocity was sued. This again suggested the ambiguity raised by the use of constant Re.

Liao & Liu (2009) tested the flow drag and heat transfer characters of carbon nanotube-water suspensions in a tube. While little pressure drop penalty was observed, the convective

heat transfer coefficient of the suspension was found to increases with the increase of the multi-wall carbon nanotube concentration under constant velocity condition. Also observed is the sharp increase of h_{nf} with the fluid temperature.

Abbasian Arani & Amani (2013) studied the effect of particle size on the convective heat transfer and pressure drop under fully developed turbulent condition with TiO_2-water nanofluid have a volume fraction of 0.01-0.02. A thermal performance factor was used to exclude the increased viscosity of nanofluid:

$$\eta = \frac{Nu_{nf}}{Nu_{bf}} \Bigg/ \left(\frac{f_{nf}}{f_{bf}} \right)^{1/3} \tag{1.16}$$

They found that for all particle concentrations investigated, while nanofluid with all particle sizes from 10nm to 40nm exhibit better performance than the base fluid, 20nm particle diameter give the best convective heat transfer performance based on the thermal performance factor. A similar study can be found in Meriläinen et al. (2013).

Recent studies have been focus on different kind of nanoparticle-base fluid pairings, e.g., (Akhavan Zanjani et al., 2013; Hemmat Esfe et al., 2014) and novel configurations, e.g., (Jamal-Abad et al., 2013; Naik et al., 2013). For example, Nguyen et al. (2007) investigated the Al_2O_3-water nanofluid performance in a jet type system designed for electronic device cooling. The heat transfer coefficient increased as much as 40% compared to that of the base fluid for a particular particle volume concentration of 6.8%. In contrast to other studies, they reported decreased convective heat transfer coefficient when 47nm nanoparticles were replaced by 36nm particles with the same volume fraction.

It can be seen from the above discussion that though the dispersion of nanoparticles in the base fluid generates higher k_{nf} than k_{bf}, a increased viscosity also comes along with it. Hence the ability of nanofluid to enhance the convective heat transfer performance is dependent on the selection of nanoparticle as well as base fluid types, and on different operational conditions, e.g., particle size, concentration. More experimental data with reliable comparison bases and parameters of merit are needed to provide the guide for practical applications.

1.7.1.2 Heat transfer coefficient and Nusselt number correlations

A large volume of studies have been devoted to validate correlations used in the prediction of turbulent heat transfer characteristics. Similar to the definition for convectional fluids, the heat transfer coefficient h_{nf} and Nusselt number Nu_{nf} for nanofluids are defined as:

$$h_{nf} = \frac{q_w}{T_w - T_b} \tag{1.17}$$

$$Nu_{nf} = \frac{h_{nf} D}{k_{nf}} \tag{1.18}$$

where the subscript nf denotes nanofluid property, q_w is the wall heat flux, T_w and T_b are wall temperature and bulk temperature, respectively, and D is a characteristic length scale of the flow system. Clearly, large values of h_{nf} and Nu_{nf} indicate better heat transfer performances. For turbulent flow, the Dittus-Boelter correlation can be used to calculate Nu for conventional fluids:

$$Nu = 0.023 \mathrm{Re}^{0.8} \mathrm{Pr}^{n} \tag{1.19}$$

Table 1.1: Nusselt number correlations for turbulent nanofluid flow in fully developed regions

References	Expressions
Pak and Cho (1998)	$Nu_{nf} = 0.021 \mathrm{Re}_{nf}^{0.8} \mathrm{Pr}_{nf}^{0.5}$
Xuan & Li (2003)	$Nu_{nf} = 0.0059(1.0 + 7.6286\varphi^{0.6886} Pe_d^{0.001}) \mathrm{Re}_{nf}^{0.9238} \mathrm{Pr}_{nf}^{0.4}$
Buongiorno (2006)	$Nu_{nf} = \frac{\frac{f}{8}(\mathrm{Re}_{nf} - 1000)\mathrm{Pr}_{nf}}{1 + \delta_v^+ \sqrt{\frac{f}{8}(\mathrm{Pr}_v^{2/3} - 1)}}$
Maïga et al.(2006)	$Nu_{nf} = 0.085 \mathrm{Re}_{nf}^{0.71} \mathrm{Pr}_{nf}^{0.35}$
Duangthongsuk & Wongwises (2010)	$Nu_{nf} = 0.074 \mathrm{Re}_{nf}^{0.707} \mathrm{Pr}_{nf}^{0.385} \varphi^{0.074}$
Sajadi & Kazemi (2011)	$Nu_{nf} = 0.067 \mathrm{Re}_{nf}^{0.71} \mathrm{Pr}_{nf}^{0.35} + .0005 \mathrm{Re}_{nf}$

where Re is the Reynolds number, Pr is the Prandtl number, and n=0.3 for cooling of the fluid, n=0.4 for heating of the fluid. Eq. (1.19) is valid for 0.7<Pr<160, Re>10000, and L/D>10 in which L is the pipe test section length and D is the pipe diameter.

Many experimental results suggested that Eq. (1.19) under-predicts Nu_{nf} when measured thermo-physical properties of nanofluids were used to calculate the dimensionless numbers (Yu et al., 2008). Hence new correlations have been proposed to fit the experimental data. A list of expressions for Nu_{nf} proposed by different researchers is provided in Table 1.1.

Yu et al. (2012) recently reviewed the existing experimental data for turbulent heat transfer of nanofluids in horizontal tubes. Despite the many new expressions proposed for Nu_{nf}, they concluded that the actual heat transfer coefficient enhancement of nanofluids over their base fluids can be predicted quite accurately using the Dittus-Boelter equation.

1.7.2 Numerical study of nanofluid turbulent heat transfer

Concerning nanofluid properties and nanofluid flow in the turbulent regime, the chaotic mixing is typically much stronger than the nanoparticle-induced micro-mixing effect. Furthermore, turbulent entrainment could significantly change nanoparticle behavior and hence the resulting heat transfer characteristics.

Maïga et al. (2006) used a single phase model to study the turbulent heat convection of nanofluids, heat transfer coefficient was found to increase with nanoparticle volume fraction and Reynolds number. The enhancement of h_{nf} is more pronounced for flows with moderate to high Reynolds numbers. Namburu et al. (2009) used a single phase model and found that heat transfer coefficient is higher at lower Reynolds numbers. Demir et al. (2011) also confirmed that single phase model is accurate enough to predict the convective heat transfer characters. On the other hand, Behzadmehr et al. (2007) used a two phase mixture model to investigate turbulent forced convection of a nanofluid in a tube. The mass transfer of nanoparticles was predicted using convection-diffusion equation. They claimed that comparison with experimental values shows that the mixture model is superior to the single phase model. Bianco et al. (2011) confirmed this result by comparing the performance of the single phase and mixture model. However, both of the studies used very simple thermal conductivity and viscosity models which cannot accurately predict the nanofluid thermo-physical properties.

Although both single-phase models with modified thermo-physical properties and two phase models have shown successful applications in predicting the heat transfer

characteristics in the turbulent regime, the validity of such models requires further investigation.

1.8 Cooling of High Concentration Photovoltaic Cells

The demand on CPV cooling spurred various cooling methods and devices. For example, Sala (1989)(Sala, 1989) discussed cooling of solar cells, considering passive cooling through radiation, natural convection and conduction, as well as forced liquid cooling. Royne et al. (2005) provided a comprehensive review of cooling techniques for CPV systems and compared different types of cooling devices with applications on single, linear, and densely packed cells. In addition to traditional water cooling methods (Du et al., 2012), alternative CPV cooling designs were developed, such as jet impinging (Barrau et al., 2011), two-phase cooling (Ho et al., 2010), liquid immersion cooling (Han et al., 2013; Zhu et al., 2011), and microchannel cooling (Müller et al., 2011). More recently, Micheli et al. (2013) reviewed the use of micro- and nano-technologies for CPV cooling, focusing on the use of nanofluids for natural convection and micro-heat pipe cooling. Still, the low heat transfer performance of conventional fluids (e.g., water, engine oil and ethylene glycol) may keep heat exchanger efficiencies too low or even cause dangerously high system temperatures.

Thus, employing nanofluid with an enhanced thermal conductivity could lead to improved energy efficiencies and smaller systems with lower capital costs. While interest in applications of nanofluids in solar energy conversion has mainly focused on solar collectors and solar water heaters, Elmir et al. (2012) published a preliminary study on solar-cell cooling using nanofluids. However, they used the model of Wasp et al. (1977) to estimate the thermal conductivity of their nanofluid, which has limited accuracy in predicting the thermo-physical properties of nanofluids. More encompassing is a recent review by Mahian et al. (2013), addressing nanofluid parameters and heat transfer mechanisms with applications.

Specifically, the authors summarized theoretical and computational works on entropy generation due to flow and heat transfer of nanofluids in various geometries and flow regimes. It was suggested that the minimization of entropy generation has to be considered for proper optimization of thermal engineering systems in terms of design and operation.

Chapter 2

AN IMPROVED THERMAL CONDUCTIVITY MODEL FOR NANOFLUIDS

2.1 Introduction

The thermal conductivity is one of the most important properties of nanofluids in motion. A significantly higher thermal conductivity of a nanofluid over the base fluid has broad applications in various fields, including cooling of high concentration photovoltaic cells and high power electronic components. However, despite of the selectively good performance of nanofluids as heat transfer fluids, experimental findings of the thermal conductivities have been controversial, while theories describing the elevated thermal conductivities have been either phenomenological or incomplete (Kleinstreuer & Feng, 2011). Therefore, part of the objective of the current study is to present a theoretical model that explains the enhanced thermal conductivity of dilute nanofluids in light of Brownian-motion induced micro-mixing, thermal contact resistance, nanoparticle-aggregation effects, and nanofluid properties.

Among the various models proposed for the effective thermal conductivity, k_{eff} or k_{nf}, Kleinstreuer & Feng (2012) started from the Koo-Kleinstreuer-Li (KKL) model (Li & Kleinstreuer, 2008) and improved three of the four main approximations. In the Feng-Kleinstreuer (F-K) model, each nanoparticle induces a velocity field in the surrounding base fluid, and the induced fluctuation velocities are superimposed to realize multi-particle effects.

With this induced velocity, the Reynolds-averaged heat transfer equation is solved to give an expression for k_{mm}, the dynamic part of the effective thermal conductivity of nanofluids, k_{nf}. The F-K model assumes mono-diperse nanoparticles in the based fluid. Here, we introduce a theoretical extension to the model by incorporating the otherwise neglected nanoparticle aggregation effects and thermal contact resistance. In addition, an assumption in the F-K model was modified to better address the relationship between the fluctuating temperature and the mean temperature field. The new model uses the Bruggeman model (Bruggeman, 1935) as well as the model of Nan et al. (1997) to describe the effective thermal conductivity of aggregates; where the latter is a model developed for arbitrary isotropic particulate composites. The Kapitza theory (Kapitza, 1941) is used to account for the interfacial resistance.

In this chapter, the theoretical background and derivation of the new model is presented, considering four contributions:

- Aggregations of nanoparticles form fractal-like structures, which can be seen as effective particles having distinctive thermal conductivities.
- The existence of nanoparticle aggregates modifies the thermal conductivity of the base fluid.
- Random motion of the fractal structures in the base fluid produces micro-scale convection effects, augmenting the energy exchange rates and hence boosting the effective thermal conductivity of the mixture.
- The thermal contact resistance at the interface of the particles and the fluids is considered using the Kapitza theory.

As a result, the effective thermal conductivity of a nanofluid is a function of nanoparticle size, temperature, particle volume fraction, the physical and chemical properties of the nanoparticles, and the type of particle-liquid pairing.

The model predictions for different particle-fluid combinations are compared with various experimental data sets for validation, focusing mainly on metal oxide nanoparticles embedded in water. The new model is able to predict the thermal conductivities of alumina, copper oxide and titanium oxide-water nanofluids accurately in the range of nanoparticle diameters of $20nm<d_p<50nm$, nanoparticle volume fractions up to 10%, and mixture temperatures below 350K. Based on the nature of the model, it can be readily extended to predict the thermal conductivities of nanofluids with other types of nanoparticle-liquid pairings and with non-spherical nano-materials such as carbon nanotubes.

2.2 Parameter Decomposition

One of the core concepts in the derivation of the current model involves the decomposition of effective variables, specifically, of velocity and temperature. This follows the Reynolds decomposition of the energy equation that divides the thermal conductivity of a nanofluid into a static part and a dispersion part (Feng, 2010; Xuan & Roetzel, 2000). In fact, this is an analogy made between random Brownian motion generated fluctuations and turbulent fluctuations:

$$\vec{v}_{nf} = \bar{\vec{v}}_{nf} + \vec{v}'_{nf} \tag{2.1a}$$

$$\vec{v}_{p} = \bar{\vec{v}}_{p} + \vec{v}'_{p} \tag{2.1b}$$

$$T = \bar{T} + T' \tag{2.1c}$$

where the superscript $\bar{}$ represents the time-averaged term and the superscript ' denotes the fluctuation term that is induced by the Brownian motion of nanoparticle aggregates. The subscript nf denotes the nanofluid, and the subscript p denotes the nanoparticle. Similar to the treatment of turbulence, the time average of the fluctuation terms equals to zero. It should be noted that the particle fluctuation velocity is the particle Brownian motion velocity.

2.3 Forces Acting on Nanoparticles

Throughout the current study, we assume the nanofluids to be dilute suspensions. Many of the properties of the dispersions change once they become concentrated, when the physics involved are far more complicated. There is no clear boundary between dilute and concentrated dispersions; however, one can evaluate the relative importance of different forces acting on the particles to determine whether a treatment of dilute/concentrated mixture is appropriate.

Nanoparticles, when dispersed in the base fluid, experience different forces. Here we give a brief discussion of the various forces acting on particles as they are of vital importance to the mechanisms of the enhanced thermal conductivity we will later discuss.

2.3.1 Random force

The random force $\overrightarrow{F_B(t)}$ that derives from the collisions between particles and the randomly moving base fluid molecules gives rise to the Brownian motion of the nanoparticles. Based on the Langevin equation and the equi-partition theorem, the stochastic process causes an average instantaneous nanoparticle velocity of $\overrightarrow{v_p}$, which can be expressed as

$$\vec{v}^{BM} = \sqrt{\frac{3\kappa_B T}{m_p}} \tag{2.2}$$

where $\kappa_B = 1.38\times10^{-23}\,\mathrm{m^2\cdot kg\cdot s^{-2}\cdot K^{-1}}$ is the Boltzmann constant, T is the local temperature, $\vec{v}^{BM}$ is the Brownian motion velocity of a typical nanoparticle with mass m_p in a time scale of $t \ll \tau$, where τ is the particle momentum relaxation time.

2.3.2 Body force

Nanoparticles may experience different field forces depending on the types of applications. Typically the gravitational force applies due to the density difference between the nanoparticles and the base fluids, which gives rise to a settling velocity

$$v_s = \frac{\Delta\rho g {d_p}^2}{18\mu_{bf}} \tag{2.3}$$

where μ_{bf} is the base fluid viscosity, $\Delta\rho$ is the density difference between the nanoparticle and the base fluid, d_p is the particle diameter, and g is the gravitational constant.

In an applied electrical field, particles will undergo electrophoretic motion with a velocity of v_{el}, i.e.,

$$v_{el} = \frac{\sigma d_p E}{3\mu_{bf}} \tag{2.4}$$

where σ is the surface charge density of the particle and E is the applied electric field.

2.3.3 Stokes force

When a nanoparticle moves relatively to the base fluid, it experiences a drag force. At Reynolds numbers of $\mathrm{Re} \le 1$, the drag force can be expressed according to the Stokes' law:

$$\vec{F}_{Stokes} = 3\pi\mu_{bf} d_p \vec{v}'_p \tag{2.5}$$

where $\vec{v}'_p$ is the instantaneous particle velocity.

An important parameter in the analysis of particle motion in a fluid is the relaxation time defined as

$$\tau_p = \frac{m_p \vec{v}'_p}{\vec{F}_{Stokes}} = \frac{m_p}{3\pi\mu_{bf} d_p} \tag{2.6}$$

It characterizes the time required for a particle to adjust to or relax its velocity to a new condition of forces.

2.3.4 Inter-particle forces

When two particles approach each other due to Brownian motion, the attractive van der Waals forces and the repulsive electrostatic force become important.

2.3.4.1 Attractive forces

For nanoparticles in a base fluid, the van der Waals forces due to the London dispersion interaction cause attraction between particles. The London dispersion force acts in a relatively long range that is comparable to the size of the particles (Israelachvili, 2011). The attractive potential is proportional to the particle diameter, the material constant (the Hamaker constant A_H (Hamaker, 1937)), and is inversely proportional to the distance of separation (Cosgrove, 2010):

$$\psi_{LD} = -\frac{A_H}{12}\left[\frac{1}{x(x+2)} + \frac{1}{(x+1)^2} + 2\ln\frac{x(x+2)}{(x+1)^2}\right] \tag{2.7}$$

where $x = h/d_p$. For small particle separations ($h \ll d_p$), Eq. (2.7) is reduced to

$$\psi_{LD} = -\frac{A_H d_p}{24h} \tag{2.8}$$

The Hamaker constant differs among materials, depending on the density as well as the electronic polarisability of the material. A typical Hamaker constant has a value of $O(10^{-20})$J.

When particles are imbedded in a fluid matrix, the attraction between particles is weakened due to the interactions between particles and the medium. In this case, the Hamaker constant can be estimated using a geometric mean:

$$A_H = \left(\sqrt{A_{\text{particle}}} - \sqrt{A_{\text{medium}}}\right)^2 \tag{2.9}$$

For metals (Au, Ag, Pt, etc.), the Hamaker constant is around 40×10^{-20}J; for water, the Hamaker constant is 3.7×10^{-20}J. For Al_2O_3-water nanofluids, $A_H = 4.17\times10^{-20}$J.

2.3.4.2 Repulsive force

When two particles approach each other, the ionic atmospheres overlap and create an ion concentration difference between the overlapped region and the bulk. This difference gives rise to an osmotic pressure acting to force the particles apart. The potential of this repulsive force can be obtained by integrating the force over distance (Hunter, 2001):

$$\psi_{EDL} = 32\pi d_p \kappa_B T \kappa^{-2} \rho_{el} \tanh^2\left(\frac{\sigma e \phi_0}{4\kappa_B T}\right)\exp(-\kappa h) \tag{2.10}$$

where κ_B is the Boltzmann constant, σ is the valence of the ions, κ is the Debye constant which is the inverse of the Debye length, ρ_{el} is the concentration of electrons, e is the electronic charge, and ϕ_0 is the electric double layer (EDL) potential at the surface of the nanoparticles. The expression is valid when κd_p is greater than 20, and becomes invalid when the double layer thickness is about the same as or larger than the particle radius. For the latter situation, the potential equations for the interaction between two double layers must be solved specifically for spherical particles. This is especially important for nanofluids,

because for metal-oxide nanofluids and metal nanofluids, κd_p is usually less than 4 (Shukla & Dhir, 2008).

2.3.5 Relative importance of the forces

The orders of magnitude of the Stokes force and the inter-particle forces in nanofluids have been compared in Feng (2010). In dilute nanofluids, the surface forces, i.e., the van der Waals forces and the electrostatic force are of the same order as the Stokes force if multi-particle interactions are considered. Meanwhile, Buongiorno (2006) has showed that body forces are negligible compared to the random force which causes Brownian diffusion. However, we will show in the next section that the surface forces are only important when nanoparticles are well dispersed in the base fluid. When the particle aggregations grow big enough, the surface forces become less important, while the wake interactions due to Brownian motion dominate.

2.4 Mechanisms of k_{nf} Enhancement

As mentioned in section 2.1, the enhanced thermal conductivity of a nanofluid is due to the combined contributions of Brownian motion induced micro-mixing, nanoparticle aggregation, and interfacial thermal resistance.

The F-K model divided the thermal conductivity of the nanofluid, k_{nf} , into two parts:

$$k_{nf} = k_{static} + k_{mm} \tag{2.11}$$

where k_{static} is the thermal conductivity part due to the effective medium theory, and k_{mm} is the thermal conductivity part due to the Brownian motion effect.

Most experimental studies relating to nanofluids have observed nanoparticle aggregations of different levels. In other words, nanoparticles exist in the base fluid not as single particles, but as building bricks of aggregates. Hence, when considering Brownian motion effects, it is the Brownian motion of the aggregates rather than primary nanoparticles that should be considered.

The thermal contact resistance exists at the interface of a nanoparticle and the base fluid (see section 1.4.2.3 in introduction) that impedes the effective transport of energy between them. This resistance compensates the enhancement of heat transport enabled by the formation of small aggregates and the Brownian motion of the aggregates. However, for a more consistent description of the heat transport in nanofluids, this effect has to be considered.

In summary, the enhanced thermal conductivity of a nanofluid is due to the particle-particle and particle-base fluid interactions that form aggregates, the aggregate-base fluid

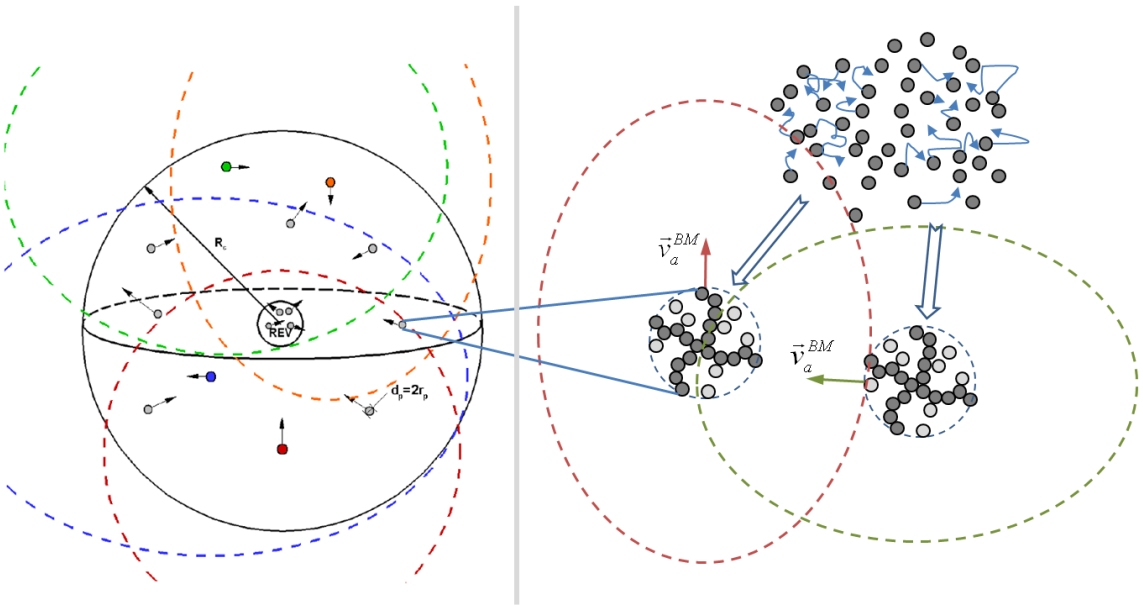

Figure 2.1: Aggregation formation and interaction due to Brownian motion

interactions that give rise to the Brownian motion, and the thermal contact resistance that moderates the augmentation. Figure 2.1 shows the formation of the aggregates, the Brownian motion of the aggregate units and the interactions between them, the combined effects of which enhances the thermal conductivity of nanofluids.

2.4.1 Nanoparticle aggregation

2.4.1.1 Aggregation formation

Aggregation formation is a process in which initially dispersed particles join together (Jullien & Botet, 1987). The stability of the mixture to aggregation is governed by the total potential energy of interaction due mainly to the combined effects of electrostatic repulsions and van der Waals inter-particle attractions. These can be described using the classical Derjaguin-

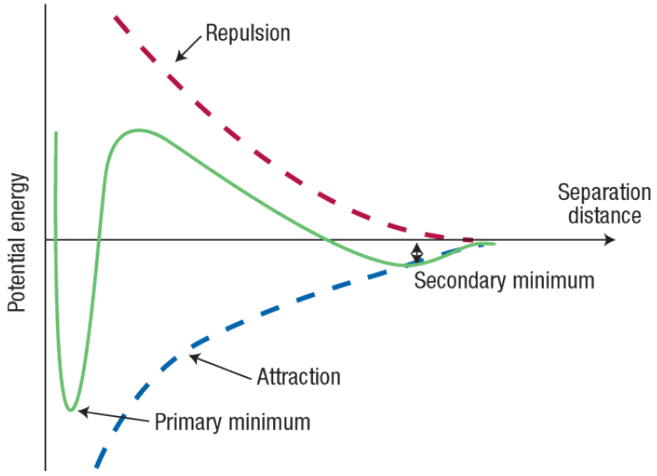

Figure 2.2: The interaction potential between two identical particles

Landau-Verwey-Overbeek (DLVO) theory of colloid stability (Derjaguin & Landau, 1941; Verwey & Overbeek, 1948):

$$\psi_{\text{total}} = \psi_{LD} + \psi_{EDL} \tag{2.12}$$

Fig. 2.2 shows the total potential between two particles as the distance between them varies, which is the consequence of the exponential decay of the repulsive term and the reciprocal decay of the attractive term. The vertex of the curve is known as the primary maximum. It sets a barrier for the two approaching particles, which must be overcome before aggregation can take place. However, this barrier to aggregation only provides kinetic stability to dispersion. The thermodynamic drive is toward an aggregated, phase separated state (Cosgrove, 2010).

The energy of a Brownian collision is of the order of $\kappa_B T$. Accordingly, a primary maximum of at least $20\,\kappa_B T$ is needed to achieve a long-term stability (Cosgrove, 2010).

Three key factors affect the value of the primary maximum significantly, i.e., the ion type and concentration, the value of the zeta potential, and the particle size. Usually the height of the maximum decreases with increasing electrolyte concentration, is proportional to the square of the surface potential, and decreases linearly with decreasing particle size at $d_p < 200\text{nm}$. As the nanofluid pH departs away from the isoelectric point, the absolute value of zeta potential increases rapidly, and the primary maximum changes accordingly.

According to the above discussion, one can expect fast aggregation of nanoparticles if the energy barrier is much less than $20\kappa_B T$. However, according to Eq. (2.10), the height of the primary maximum increases as aggregates become larger, which significantly hinders further aggregation. Furthermore, as particles form clusters, the average distance between aggregates grows while the Brownian motion intensity reduces. This means smaller chance of encounter that drastically reduces the aggregation rate.

The average (minimum) separation distance between two spheres in a well dispersed suspension can be obtained by (Cosgrove, 2010)

$$L = \frac{d}{2}\left[\left(\frac{\varphi_{rcp}}{\varphi}\right)^{\frac{1}{3}} - 1\right] \tag{2.13}$$

where d is the sphere diameter and $\varphi_{rcp} = 0.64$ corresponds to random close-packing of the particles. For simplicity, we assume that the effective diameter D of an aggregate can be calculated using volume effective diameter, then the relation between D and d is $(D/d)^3 = n$, where n is the number of primary particles in an aggregate. Therefore the relation between L and n can be obtained as

$$L = n^{\frac{1}{3}} \cdot \frac{d}{2}\left[\left(\frac{\varphi_{rcp}}{\varphi}\right)^{\frac{1}{3}} - 1\right] \tag{2.14}$$

Fig. 2.3 shows the change of average distance between aggregates for different n and φ. There is a log-linear relationship between L and n for a given particle volume fraction φ. Meanwhile the average distance increases rapidly when φ keeps reducing below 1%. The interaction energy between two spheres decays as $1/D^n$.

According to this analysis, we assume that there is a balance state, i.e., a relatively long period of stable stage for the nanofluid when mean cluster size reaches a plateau and further aggregation is sluggish. The nanofluid discussed in the current study lies in this stage. It should be noted that this stable state is dynamic, i.e., there are still aggregation formation and break-up, but the average size of the aggregates varies little.

Clearly, it is no longer proper to treat the nanoparticles as individual elements. Instead, we take a single aggregate as a basic unit, and determine k_{nf} based on the assumption that the nanofluid is a mixture of aggregates with average radius R_g dispersed in the base fluid. Theories considering nanoparticle aggregations were discussed in the introduction part. For example, inspired by the treatment of Shih et al. (1990) for colloidal gels, Evans et al. (2008) presented a three-level homogenization model to describe the particle redistribution in the fluid matrix, which was also adopted by Chen et al. (2009) and Gharagozloo & Goodson (2011). In this model, nanoparticles form fractal like structures (aggregates), and the aggregates are treated as spheres with radius determined by the radius of gyration, R_g.

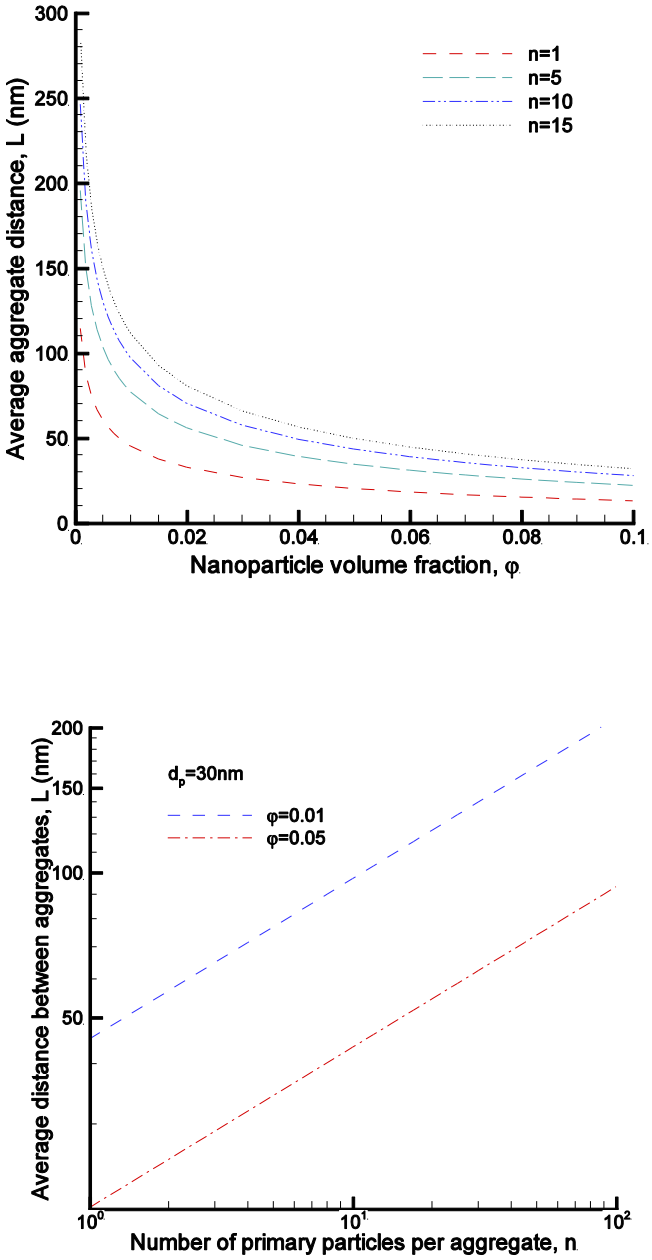

Figure 2.3: Average distance between aggregate units vs. number of primary particles per aggregate and nanoparticle volume fraction

2.4.1.2 Fractal structure

We use fractal theory to describe the nanoparticle clusters. Fractals are scale invariant objects with dilation symmetry, i.e., they look the same on all scales (Kulkarni et al., 2011). An illustration of a fractal structure is provided Fig. 2.4. An introduction to fractals is given by Family & Landau (1984). A fractal aggregate is a cluster of particles that scales in a fractal structure from the primary or monomer particle size to the overall size of the aggregate. Fractal aggregates can be found in various colloids as a result of diffusion limited cluster aggregation.

Generally two major categories can be identified for the aggregation formation: (i) particle-cluster aggregation or diffusion limited aggregation (DLA), which occurs when primary particles diffuse to and stick to a stationary, growing cluster (Witten Jr & Sander, 1981); and (ii) cluster-cluster aggregation or diffusion limited cluster aggregation (DLCCA), which occurs when, along with the primary particles, the clusters themselves diffuse and stick when they randomly touch each other (Kolb et al., 1983). Only DLCCA occurs in colloids as well as aerosols (Kulkarni et al., 2011). An example of a fractal aggregate is shown in Fig. 2.5.

Nanoparticles form fractal like clusters (aggregates) in nanofluids. An effective sphere with average radius R_g can be used to represent the aggregate (see Fig. 2.5). The spherical unit (called aggregate unit hereafter) itself is composed of two kinds of nanoparticles, i.e., backbone particles and dead ends particles. The main branches (backbones) of a aggregate span the sphere of radius R_g, while the dead ends particles connect to the backbones in a loose manner without showing any obvious pattern. It should be noted that the fractal

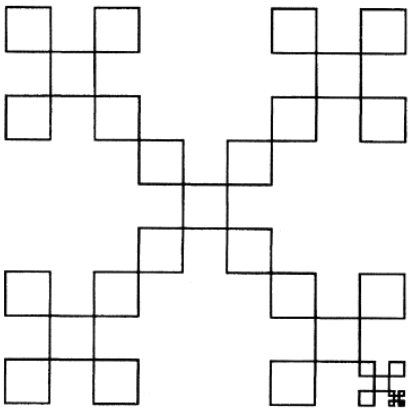

Figure 2.4: A scale invariant structure (From: Kulkarni et al. (2011))

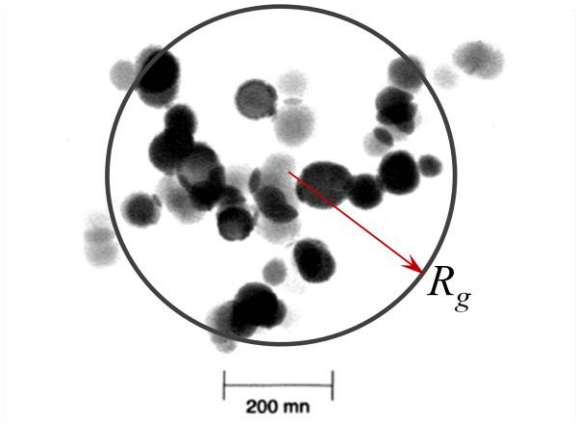

Figure 2.5: A fractal structure (Modified from Kulkarni et al. (2011))

aggregates are three dimensional structures in the Euclidean space. More experimental evidence of the fractal nanoparticle clusters as a result of nanoparticle aggregation can be seen in Fig. 2.6.

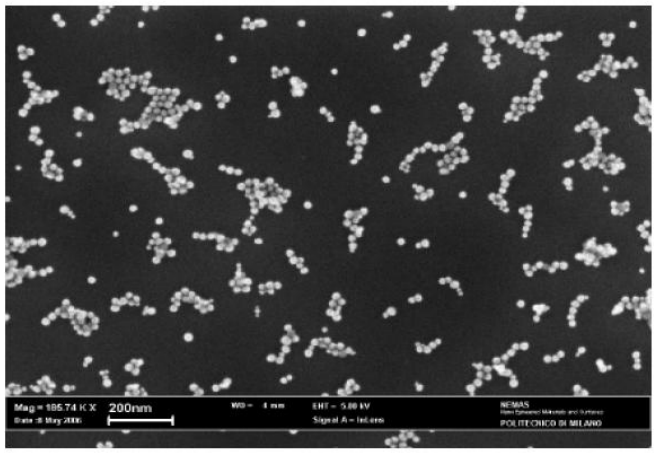

SEM picture of silica nanofluid (From: Williams (2007))

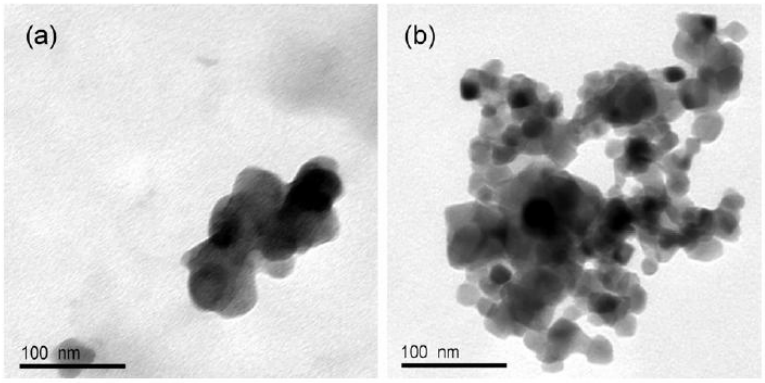

TEM images of (a) alumina and (b) titania nano-particles (From: Utomo et al. (2012))

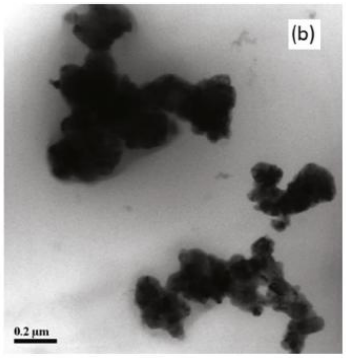

TEM images of nanofluids taken after 2h of preparation (From: Kole & Dey (2013))

Figure 2.6: Experimental evidences of nanoparticle aggregation

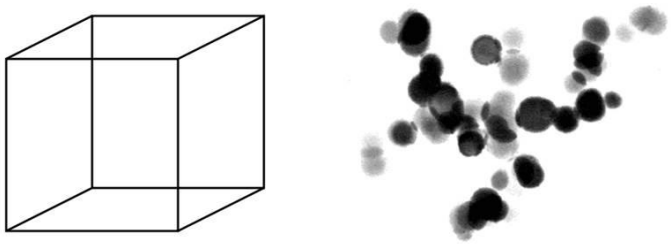

Figure 2.7: Illustration of fractal dimension as compared with the dimension of a cube

2.4.1.3 Aggregation size

Fractal aggregates can be measured by means of fractal dimension, which relates the linear size of a structure with its volumetric size. The latter is linearly related to the mass or number of primary particles, *N*, in the aggregate. Figure 2.7 shows an analogy between a fractal aggregate and a regular geometry in the Euclidean space, e.g., a cubic. The volume of a cubic is equal to the length of the side to the third power (its spatial dimension), while the number of primary particles in a fractal aggregate scales with the linear size R_g to the fraction dimension D_f, i.e.,

$$N \propto R_g^{D_f} \tag{2.15}$$

where R_g is the radius of gyration of a fractal aggregate, which is taken to be the radius of the aggregate unit discussed above; and D_f is the fractal dimension, which is a parameter that relates only to the geometry. The radius of gyration is defined as the root mean square distance of the objects' parts from either its center of gravity or a given axis, i.e.,

$$R_g^{\,2} = \frac{1}{N}\sum_{k=1}^{N}\left(r_k - r_{mean}\right)^2 \tag{2.16}$$

where r_{mean} is the mean position of the monomers. It should be noted that, the linear size can be any of the geometric sizes, e.g., a diameter, a length, or a radius of gyration, but it cannot be a mobility radius which depends on the linear geometric size as well as the flow situations (Kulkarni et al., 2011).

The fractal dimension D_f provides a way to quantitatively describe the ramification of a random aggregate. It measures the speeds of the aggregates to fill space as the radius of gyration varies. Specifically, a smaller D_f means a faster piling-up of the space as R_g increases. Hence the fractal dimension determines the aggregate density, the optical properties, the diffusion characters, and the growth kinetics of the aggregates.

The aggregate size will increase as more particles join. When aggregates become large enough (~1μm), settling occurs that reduces particle concentration and hence, mixture thermal conductivity. Potentially large enhancements can occur only in stable solutions where aggregates are small enough to remain in the suspension. For the current study, we only consider nanofluids in this stable stage, i.e., the aggregates are not big enough to trigger sedimentation. Therefore, it is necessary to estimate the upper bound of the aggregate unit size for this stability. One way to determine it is to equal the average distance traveled by a particle undergoing Brownian motion, with the distance moved under settling velocity during the same characteristic time. The average Brownian motion velocity can be estimated using Eq. (2.2); while the characteristic time scale is given by

$$\tau_a = \frac{2D}{\left(v_a^{BM}\right)^2} \tag{2.17}$$

The settling velocity is obtained through a force balance between gravity, buoyancy, and drag, expressed as:

$$u_{TS} = \frac{d_a^2\left(\rho_a - \rho_{bf}\right)g}{18\mu_{bf}} \tag{2.18}$$

where ρ is the density of the aggregate (a) or fluid (bf), d_a is the effective diameter of the aggregate, u_{TS} is the terminal settling velocity, and g is the acceleration of gravity. Hence we obtain that

$$d_a = O(\mu_{bf}^{2/7}\kappa_B^{1/7}T^{1/7}\Delta\rho^{-3/7}) \tag{2.19}$$

For metal oxide-water nanofluids, $d_a = O(1\mu\text{m})$. This indicates that nanofluids should be stable even when the aggregates are an order of magnitude larger than the primary particles. It should be noted that in the estimation of the velocity scales, aggregates are treated as spheres with an average volume effective diameter. This assumption will be further applied in the following derivation where applicable.

In summary, nanoparticles form fractal like aggregations in nanofluids, having effective size determined by the radius of gyration. Aggregates consist of two kinds of nanoparticles: backbone particles and dead-ends particles. There will be a dynamically stable stage for the nanofluids when the average aggregation size reaches a plateau. It is the Brownian motion of these aggregates that enhances the thermal conductivity of the nanofluid.

2.4.2 Brownian motion induced micro-convection

We have presented the model to treat the aggregates in the base fluid, i.e., small spherical units with average diameter determined by the radius of gyration. In light of this treatment, the nanofluid is akin to a mixture of particles of diameter R_g dispersed in the base fluid. Therefore, the F-K model (Feng, 2010) can now be modified to determine the effective thermal conductivity of the mixture.

According to the F-K model, particles (in the current case, aggregate units) interact with each other indirectly through Brownian motion induced perturbations to the base fluid. Since the particle Reynolds number is usually well below unity, the analytical solution for Stokes flow around a spherical particle can be employed to give the induced velocity around a particle (Panton, 2006):

$$v_{nf}^{(r)}{}' = -\left(\frac{\left|v'_p\right| R_g{}^3}{2r^3} - \frac{3\left|v'_p\right| R_g}{2r} \right) \cos\theta \tag{2.20a}$$

$$v_{nf}^{(\theta)}{}' = -\left(\frac{\left|v'_p\right| R_g{}^3}{4r^3} + \frac{3\left|v'_p\right| R_g}{4r} \right) \sin\theta \tag{2.20b}$$

$$v_{nf}^{(\phi)}{}' = 0 \tag{2.20c}$$

where $\left|v'_p\right|$ is the particle velocity, r is the distance from the particle center. The particle velocity can be determined using the Langevin equation

$$m_a \frac{d\vec{v}'_p}{dt} = -\vec{F}_{Stokes} + \vec{F}_B(t) \tag{2.21}$$

where $\vec{F}_{Stokes}$ is the Stokes drag force, and $\vec{F}_B(t)$ is the random force due to collisions with base fluid molecules. Using $v'_p = \frac{dh}{dt}$, Eq. (2.21) can be rewritten as

$$\frac{d^2h}{dt^2} + \frac{3\pi\mu_{bf}R_g}{m_a}\frac{dh}{dt} = F_B(t) \tag{2.22}$$

The solution to this equation with initial conditions $h(0) = 0$ and $dh/dt\big|_{t=0} = \sqrt{\kappa_B T/m_a}$ is well established (Coffey et al., 2004). Set the cut-off radius to be where $\left|\overrightarrow{v'_{nf}}\right| = 0.002\left|\overrightarrow{v_p}\right|$, after superposition of the perturbation velocities due to multiple particles at a fluid package point, the overall induced velocity can be determined at any point of the fluid domain to be

$$v_{nf}^{(y)\prime} = \frac{9}{64}\frac{R_c^2}{R_s^2}\pi\varphi\left(\sqrt{\frac{\kappa_B\bar{T}^H}{m_a}} - \sqrt{\frac{\kappa_B\bar{T}^L}{m_a}}\right)e^{-t/\tau} \tag{2.23}$$

where R_c is the cut-off radius.

It should be noted that in deriving Eq. (2.21), aggregate units are assumed to disperse evenly in the base fluid. Also, weak surface interaction between aggregate units was assumed, so that the van der Waals forces as well as the electrostatic forces can be neglected (see the discussion in Section 2.4.1.1). The latter assumption eliminated the particle-interaction force term which appeared in the extended Langevin equation in the original derivation of Feng (2010). This elimination, in consequence, greatly reduced the complexity of the final expression of k_{nf} (Eq. (2.46)). Hence, by considering the nanoparticle aggregation, not only has the theory become more complete, but it also has exhibited simpler form. In fact, in the F-K model, the interaction forces between two particles were

approximated using a linear expression, which was later curve fitted based on experimental data, because of the mathematically prohibitive nature of superposition of many-particle interactions. Yet in the current study, this curve fitting process is avoided based on solid physical ground.

2.4.3 Thermal contact resistance

The effect of the Kapitza resistance can be incorporated to give an effective nanoparticle thermal conductivity k_{peff} as (Li & Kleinstreuer, 2008):

$$\frac{2d_p}{k_{peff}} = \frac{2d_p}{k_p} + 2R_b \tag{2.24}$$

2.5 Revised Effective Medium Theory

As discussed above, the thermal conductivity of the nanofluid, k_{nf}, comprised of two parts: k_{static}, the thermal conductivity part due to effective medium theory, and k_{mm}, the thermal conductivity part due to the Brownian motion effect. The effective medium theory for predicting the thermal conductivity of a mixture of particles perfectly dispersed in a fluid without Brownian motion provides us with a good estimation for k_{static}

$$k_{static} = k_{bf} \cdot \left(1 + \frac{3\left(\frac{k_p}{k_{bf}} - 1 \right)\varphi}{\left(\frac{k_p}{k_{bf}} + 2 \right) - \left(\frac{k_p}{k_{bf}} - 1 \right)\varphi} \right) \tag{2.25}$$

However, due to the combined effects of thermal contact resistance and the aggregation effects, we need to revise the effective medium theory in the following way for nanofluids: nanoparticles form fractal like clusters (aggregates) in the fluid matrix, building effective spherical units with average radius of R_g. The effective thermal conductivity of the aggregate units, k_a, is determined and then used to replace the thermal conductivity of particles, k_p, in Eq. (2.25).

To determine k_a, we use the three-level homogenization model described by Evans et al. (2008). According to this model, nanoparticles form fractal like structures due to aggregation. Each cluster is embedded in a sphere of radius R_g, with nanoparticles that form linear chains (backbones) and nanoparticles that attach to the backbones (dead ends). The

dead ends particles and the base fluid form a medium with effective thermal conductivity k_{de} . When the backbone is included, the effective thermal conductivity of the sphere (aggregate unit of radius R_g), k_a , is determined using the model of Nan et al. (1997). k_{de} (Bruggeman, 1935) and k_a are given by

$$\varphi_{de}\left(\frac{k_{peff}-k_{de}}{k_{peff}+2k_{de}}\right)+(1-\varphi_{de})\left(\frac{k_{bf}-k_{de}}{k_{bf}+2k_{de}}\right) \tag{2.26}$$

$$k_a = k_{de}\cdot\frac{3+\varphi_b\left[2\beta_{11}\left(1-L_{11}\right)+\beta_{33}\left(1-L_{33}\right)\right]}{3-\varphi_b\left(2\beta_{11}L_{11}+\beta_{33}L_{33}\right)} \tag{2.27}$$

where φ_{de} is the volume fraction of dead end particles in an aggregate unit, i.e.,

$$\begin{aligned}\varphi_{de} &= \varphi_{\text{int}}-\varphi_b \\ &= \left(\frac{R_g}{d_p}\right)^{D_f-3}-\varphi_b\end{aligned} \tag{2.28}$$

where φ_{int} and φ_b are, respectively, the volume fraction of nanoparticles in the aggregate unit and the volume fraction of backbone particles. The latter is given by

$$\varphi_b = \left(\frac{R_g}{d_p}\right)^{D_1-3} \tag{2.29}$$

where D_1 is a dimension ranging $1\le D_1\le D_f$ given in Shih et al. (1990). In Eq. (2.26), k_{peff} is the effective thermal conductivity of the nanoparticles including the thermal contact resistance. k_{peff} can be determined using Kaptiza's theory:

$$k_{peff} = \frac{k_p}{1+R_K k_p/d_p} \tag{2.30}$$

where R_K is the Kapitza resistance.

Eq. (2.27) is developed to predict the effective thermal conductivity of arbitrary isotropic particulate composites with interfacial thermal resistance. It is based on the effective medium approach. The various symbols in Eq. (2.27) are explained here:

$$L_{11} = \frac{p^2}{2\left(p^2-1\right)} - \frac{p^2}{2\left(p^2-1\right)^{1.5}} \cosh^{-1} p \tag{2.31}$$

$$L_{33} = 1 - 2L_{11} \tag{2.32}$$

which are geometrical factors depending on the particle shape (Nan, 1994). Here $p = R_g / d_p$ is the aspect ratio of an ellipsoid.

$$\beta_{ii} = \frac{k_{ii}^c - k_{de}}{k_{de} + L_{ii}\left(k_{ii}^c - k_{de}\right)}, \quad i = 1,3 \tag{2.33}$$

where k_{ii}^c (i=1,2,3) are the equivalent thermal conductivities along corresponding symmetric axis of a ellipsoidal composite unit cell, obtained using the multiple-scattering approach (Nan, 1993):

$$k_{ii}^c = \frac{k_p}{1 + \gamma L_{ii} k_p / k_{bf}} \tag{2.34}$$

where the dimensionless parameter γ is given as

$$\gamma = \left(2 + \frac{1}{p}\right)\alpha, \quad \alpha = \frac{A_K}{d_p} \tag{2.35}$$

Again, A_K is the Kapitza length.

Till now, the effective thermal conductivity of an aggregate unit has been determined by combining the theory of Bruggeman (1935) and Nan et al. (1997). Therefore, the thermal conductivity part due to effective medium theory, k_{static}, can be revised as

$$k_{static} = k_{bf} \cdot \left(1 + \frac{3\left(\frac{k_a}{k_{bf}} - 1 \right)\varphi}{\left(\frac{k_a}{k_{bf}} + 2 \right) - \left(\frac{k_a}{k_{bf}} - 1 \right)\varphi} \right) \tag{2.36}$$

It should be noted that, since k_a is determined using a model developed for ellipsoidal particles, this model is also suitable for non-spherical particles dispersed in base fluids with proper modification of geometrical parameters involved. This can be done in future works.

In the next section, we determine k_{mm}, the thermal conductivity part due to the Brownian motion effects.

2.6 Brownian Motion Induced Thermal Conductivity

We have already discussed all the mechanisms that would contribute to the enhanced thermal conductivity of nanofluids. So the next step is to derive the explicit expression of the effective thermal conductivity, k_{mm}. The governing equation of the system, in particular, the energy equation reads

$$\frac{\partial T}{\partial t}+\nabla\cdot\left(\vec{v}_{nf}T\right)=\nabla\cdot\left[\left(\frac{k_{nf}}{\left(\rho c_p\right)_{nf}}\right)\nabla T\right]+\frac{\Phi}{\left(\rho c_p\right)_{nf}} \tag{2.37}$$

where Φ is the viscous dissipation term:

$$\begin{aligned}\Phi = 2\mu_{nf}&\left[\left(\frac{\partial v_{nf}^{(x)}}{\partial x}\right)^2+\left(\frac{\partial v_{nf}^{(y)}}{\partial y}\right)^2+\left(\frac{\partial v_{nf}^{(z)}}{\partial z}\right)^2\right]\\ &+\mu_{nf}\left[\left(\frac{\partial v_{nf}^{(x)}}{\partial y}+\frac{\partial v_{nf}^{(y)}}{\partial x}\right)^2+\left(\frac{\partial v_{nf}^{(x)}}{\partial z}+\frac{\partial v_{nf}^{(z)}}{\partial x}\right)^2+\left(\frac{\partial v_{nf}^{(z)}}{\partial y}+\frac{\partial v_{nf}^{(y)}}{\partial z}\right)^2\right]\end{aligned} \tag{2.38}$$

Similar to the treatment for the superposition of perturbation velocities (see Section 2.2.2), here we assume that the fluid is quiescent and the temperature difference occurs only in the y-direction. The reasoning behind this approach is that the thermal conductivity is the intrinsic property of fluids, which does not change whether or not heat convection presents. Thus, in this 1-D case, by substituting the fluctuating terms of equations (2.1a) and (2.1c) into Eq. (2.37) and time averaging it, the equation reduces to

$$\overline{\left|v_{nf}^{(y)}{}'\right|\frac{\partial T'}{\partial y}}=\frac{1}{\left(\rho c_p\right)_{nf}}\frac{\partial k_{mm}}{\partial y}\frac{\partial \bar{T}}{\partial y} \tag{2.39}$$

where $v_{nf}^{(y)}{}'$ is given by Eq. (2.23).

To solve Eq. (2.39), an explicit expression for T' is needed. In the treatment of the F-K model, T' is related to T through an analogous to the concept of mean-molecular spacing in microfluidics of liquids:

$$T' = \lambda \frac{\partial \bar{T}}{\partial y} \tag{2.40}$$

where λ is the isotropic mixing length composed of two parts:

$$\lambda = \varphi \lambda_p + (1-\varphi)\lambda_{bf} \tag{2.41}$$

where λ_p is the mixing length for nanoparticles and λ_{bf} is the mean molecular distance for base fluids.

Here we argue that the mixing length should be $\lambda = \lambda_p$ only, for the following reason: in the Prandtl's mixing length theory for turbulent flow, assuming gradient-type diffusion, the coefficient of turbulent eddy viscosity is assumed to be the product of the turbulent mixing length and the gradient of the fluctuating velocity. This is analogous to the kinetic theory, where the kinematic viscosity is equal to the product of the root-mean-square velocity of the molecules and the mean free path. In light of these assumptions, the fluctuation ω' of a transport property in the turbulent flow with respect to the mean value $\bar{\omega}$ can be expressed as

$$\omega' = \lambda \frac{\partial \bar{\omega}}{\partial y} \tag{2.42}$$

where, the gradient of the transport property is assumed to be constant over the length scale λ.

For heat transport in nanofluids, the fluctuation of temperature, T', is due to the Brownian motion of particles/aggregate units. Therefore, analogous to the assumption that

the fluctuating velocity is constant within the length scale determined by the product $\left|\vec{v}^{BM}\right|\tau$ (see Eq. (2.2) and (2.6)), it is reasonable to assume that the temperature gradient is constant within the same length scale, i.e.,

$$\lambda = \tau_a \cdot \left|\vec{v}_a^{BM(y)}\right| \tag{2.43}$$

where the Brownian motion velocity of the aggregate units is given by

$$\left|\vec{v}_a^{BM}\right| = \sqrt{\frac{3\kappa_B T}{m_a}} \tag{2.44}$$

and the characteristic time scale is given by

$$\tau = \frac{m_a}{3\pi\mu_{bf} R_g} \tag{2.45}$$

where m_a is the average mass of the aggregate units determined by the density and volume of the particles in a typical aggregate unit. Here we have assumed that λ has the same length in all directions.

Combine Eq. (2.23), (2.39), and (2.40), we obtain the expression for k_{mm} as

$$k_{mm} = 19631 \cdot C_c \varphi \frac{\kappa_B \tau_a}{m_a} \left(\rho c_p\right)_{nf} (\overline{T} \cdot ln\overline{T} - \overline{T}) \tag{2.46}$$

where the number 19631 comes from direct calculation of superimposition of multi-aggregates induced velocity, C_c is a correlation factor which compensates for the variation of material properties that affect, for example, Kapitza length and aggregation properties; for the aggregate-aggregate interactions forces which have been neglected; for the cut-off radius

R_c of multi-aggregate interaction through perturbation, etc.. $C_c \approx 1$. In Eq. (2.46), the density and specific heat capacity of the nanofluid are given by (Li & Kleinstreuer, 2008):

$$\rho_{nf} = \rho_p \varphi + \rho_{bf} \left(1 - \varphi\right) \tag{2.47}$$

$$c_{pnf} = (c_p)_p \rho_p \varphi + (c_p)_{bf} \rho_{bf} (1 - \varphi) \tag{2.48}$$

2.7 Thermal Conductivity of Nanofluids

2.7.1 Expression for k_{nf}

Again, we emphasize that the thermal conductivity of the nanofluid, k_{nf}, is comprised of two parts:

$$k_{nf} = k_{static} + k_{mm} \tag{2.49}$$

where k_{static} was determined in Section 2.5 as

$$k_{static} = k_{bf} \cdot \left(1 + \frac{3\left(\frac{k_a}{k_{bf}} - 1 \right)\varphi}{\left(\frac{k_a}{k_{bf}} + 2 \right) - \left(\frac{k_a}{k_{bf}} - 1 \right)\varphi} \right) \tag{2.50}$$

and k_{mm} was determined in Section 2.6 as

$$k_{mm} = 19631 \cdot C_c \varphi \frac{\kappa_B \tau_a}{m_a} \left(\rho c_p \right)_{nf} (\overline{T} \cdot ln\overline{T} - \overline{T}) \tag{2.51}$$

In Eq. (2.50) ,

$$k_a = k_{de} \cdot \frac{3 + \varphi_b \left[2\beta_{11}\left(1 - L_{11}\right) + \beta_{33}\left(1 - L_{33}\right) \right]}{3 - \varphi_b \left(2\beta_{11} L_{11} + \beta_{33} L_{33} \right)} \tag{2.52}$$

$$\begin{aligned} k_{de} = {} & (3\varphi_{de} - 1)k_{peff} + (2 - 3\varphi_{de})k_{bf} \\ & + \sqrt{[(3\varphi_{de} - 1)k_{peff}]^2 + [(2 - 3\varphi_{de})k_{bf}]^2 + 2[2 + 9\varphi_{de}(1 - \varphi_{de})]k_{peff} k_{bf}} \end{aligned} \tag{2.53}$$

It can be seen from the expressions of k_{static} and k_{mm} that the thermal conductivity of nanofluids is affected by a number of factors, i.e., nanoparticle diameter d_p (incorporated in

k_a), volume fraction φ, mixture temperature *T*, aggregation size, and density and specific heat capacity of the mixture.

2.7.2 Dependence of k_{nf} on different parameters

Similar to the decomposition of k_{nf} into k_{static} and k_{mm}, the dependence of k_{nf} on different parameters can be interpreted in two parts.

First we look at the behavior of k_{static}, which is a function of the base fluid thermal conductivity, the nanoparticle volume fraction, and the effective thermal conductivity of the aggregate units. The original Maxwell model gives an effective thermal conductivity of a mixture that increases with the particle volume fraction. Since in Eq. (2.50), the original form of the Maxwell model is retained, one could say for certain that k_{static} also increase with the nanoparticle volume fraction. Another important parameter in Eq. (2.50) is the effective thermal conductivity of the aggregate units, which replace the thermal conductivity of particles in the original Maxwell model. Hence k_{static} will change with k_a in the same way as k_{static} changes with k_p in the original Maxwell model.

Next we look at the behavior of k_{mm}, which can be rewritten as:

$$k_{mm} = 19631 \cdot C_c \kappa_B \varphi \left(\rho c_p\right)_{nf} G(\mu_{bf}, d_a) F(\bar{T}) \tag{2.54}$$

where the contributing factor are, respectively:

$$G(\mu_{bf}, d_a) = \frac{1}{6\pi\mu_{bf} R_g} \tag{2.55a}$$

$$F(\bar{T}) = \bar{T} \cdot ln\bar{T} - \bar{T} \tag{2.55b}$$

One can conclude from Eq. (2.54) that k_{mm} increase linearly with nanoparticle volume fraction, and increase by a order of 1 to 2 with $\bar{T}$. Also, k_{mm} will increase when the effective radius of the aggregate unit decreases. It should be noted that the increase of the base fluid viscosity will reduce k_{mm}, because the Stokes force experienced by the aggregates will raise in this case, which effectively reduce the intensity of Brownian motion effects.

2.7.2.1 Dependence on volume fraction

It can be seen from Eq. (2.50) that the Maxwell model predicts a linear relationship between the thermal conductivity and the particle volume fraction. In the new model provided, Eq. (2.54) also gives a linear relationship between the two. However, this linearity is broken by the expression of k_a given by Eq. (2.52). Specifically, k_a is a function of R_g, the radius of gyration, or the effective radius of the aggregate unit, which itself is a function of the volume fraction. Therefore, the model presented here gives a non-linear relationship between the thermal conductivity and the volume fraction (see Fig. 2.8). This is a reasonable prediction because the thermal conductivity of the nanofluid is radically affected by the aggregation effect, whereas the latter is affected by the volume fraction of nanoparticles. As the volume fraction increases, the aggregate size grows, and the Brownian motion effects become less important, which effectively reduces k_{mm}. Hence the increase of k_{nf} is slowed down due to larger aggregate formation. Further discussions of the dependence of k_{nf} on R_g can be seen in section 2.7.2.3. On the other hand, when the nanoparticle volume fraction is very small, the

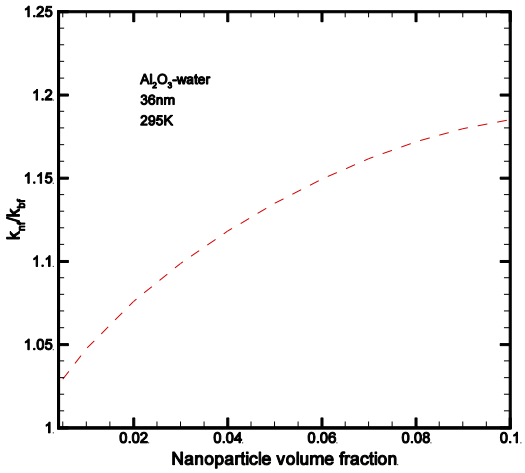

Figure 2.8: Model prediction of thermal conductivity ratio *vs*. nanoparticle volume fraction for an Al_2O_3-water nanofluid

aggregation effect will be meager. Consequently, the current model will not apply at very low particle concentrations.

2.7.2.2 Dependence on temperature

The value of k_{nf} is affected by the mixture temperature in two ways: the aggregation size which is an important parameter in the expression of k_a is influenced by the temperature; and the thermal conductivity due to micro-mixing effects is a function of the temperature (see Eq. (2.57b)). The change of k_{nf} with respect to temperature is shown in Fig. 2.9 for both Al_2O_3-water nanofluid and CuO-water nanofluid. As the temperature increases, the Brownian motion effect intensifies, consequently, k_{mm} raises up. This is the main reason for the dependence of k_{nf} on temperature. The influence of T on k_{static} through R_g will be discussed in the next section.

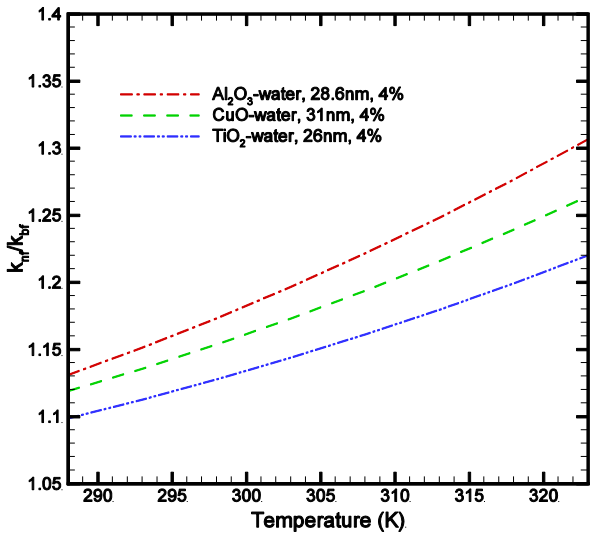

Figure 2.9: Model prediction of thermal conductivity ratio *vs*. temperature

2.7.2.3 Dependence on aggregation size

One of the most important parameters in the current study of the thermal conductivity of nanofluids is the aggregation size, R_g . The formation of aggregations in nanofluids is an extremely complex process which is difficult observe and describe. The lack of quantitative data on the aggregation process leads us to the compromise of qualitative characterization. Fortunately, this can be done more rigorously in the context of the state of the art.

The aggregation size is affected by many factors, e.g., volume fraction, temperature, particle size, particle physical and chemical properties, and flow conditions, among which the first two are the most important and will be discussed in detail. Information concerning the other factors will be addressed briefly here, and can be found easily in the open literature.

The influence of the temperature on R_g is easy to observe, because as temperature increases, particles gain more kinetic energy. Even though this means higher possibility for particles to overcome the potential barrier due to the van der Waals forces and electrostatic force, studies have shown that aggregation favors gentle collisions (Hinds et al., 1983). Moreover, particles may bounce away or glide away from each other especially in more viscous fluids in the case of high velocity collisions. This is partly due to the complex hydrodynamic interactions between particles that involve the drainage of the fluid film in between the particles. The competition and balance between these two aspects are difficult to quantify, but it indicates a slow decrease (or increase) of R_g with the change of temperature. In fact, experiments indicate that raising the mixture temperature could prevent the particles from forming large scale particle clusters (Chein & Chuang, 2007). Therefore in the current study, we propose a weak dependency of R_g on T.

As mentioned earlier, the aggregation size grows when the volume fraction increases, due to the reduced average inter-particle distance *L*, which raises the rate of particle encounter. The collision frequency, i.e., the average number of collisions between identical particles per unit time, can be estimated by:

$$Z = N_A \pi d^2 \sqrt{\frac{8\kappa_B T}{\pi m/2}} \tag{2.56}$$

where N_A is the number of particles per unit volume, d is the diameter of the particle, and m is the particle mass. $N_A \propto \varphi$ for a well dispersed system. Hence the number of particles in a fractal aggregate, *N*, can be estimated to be $N \propto Z \propto N_A \propto \varphi$. Eq. (2.15) shows that *N* is

proportional to the radius of gyration to the order of D_f, i.e., $N \propto R_g^{D_f}$. Therefore the relationship between φ and R_g can be established as

$$\varphi \propto R_g^{D_f} \tag{2.57}$$

where D_f is usually in the range of 1.4~2.1. However, due to the existence of dead ends particles, not all the particles in an aggregate unit are part of the backbones. Considering this, the relationship can be modified as:

$$R_g \propto \varphi^{1/2} \tag{2.58}$$

Other factors such as pH value of the fluids, particle size, and particle physical and chemical properties also affect R_g. For example, larger particles are less likely to form aggregations (recall the case of micro-particles); particles with different atom structures have different dipole alignments; turbulent flow tend to break the aggregation structure due to the large turbulent kinetic energy etc.. However, these factors are less important in the develop of the current model, therefore are not considered explicitly but include in the correction factor C_c. To this end, we can formulate an expression for R_g according to the discussions above:

$$R_g = 2.5 d_p \sqrt{\frac{\varphi}{0.01}} \cdot \sqrt{\frac{T_0}{\overline{T}}} \tag{2.59}$$

where T_0 is the reference temperature, which is 273.15K.

2.8 Comparisons

Having obtained a new expression for k_{nf} , we now compare the predictions of Eq. (2.50) and (2.51) with benchmark experimental data sets (Chon et al., 2005; Das et al., 2003; Li & Peterson, 2007a; Mintsa et al., 2009)(Chon et al., 2005; Das et al., 2003; C. H. Li & Peterson, 2007a; Mintsa et al., 2009) which include Al_2O_3-water, CuO-water and TiO_2-water nanofluids with different nanoparticle diameters at various temperatures and volume fractions. Additionally, comparisons with newly presented experimental data for nanofluid thermal conductivities are also provided.

2.8.1 Al_2O_3-water nanofluid comparisons

We compared the predictions of the newly developed model with benchmark experimental data as well as recent experimental results for the thermal conductivity of Al_2O_3-water nanofluids with particle diameters ranging from 36nm to 47nm, volume fractions less than 10%, and temperatures between 293K and 343K. The aggregation size R_g was determined by Eq. (2.59), and the corrector factor C_c was taken to be 1.05.

The results are given in Fig. 2.10 and Fig. 2.11. Overall, the predictions are in excellent agreement with the experimental results. However, the k_{nf} - model underestimates the measured thermal conductivity of the nanofluids for high volume fractions, i.e., 6%, under high temperatures (see the comparison with Mintsa et al. (2009) in Fig. 2.10). As in the experimental procedures Mintsa et al. (2009) used a mechanical mixer to stir the nanofluid for approximate 60 seconds before every reading, the discrepancy may be due to a better

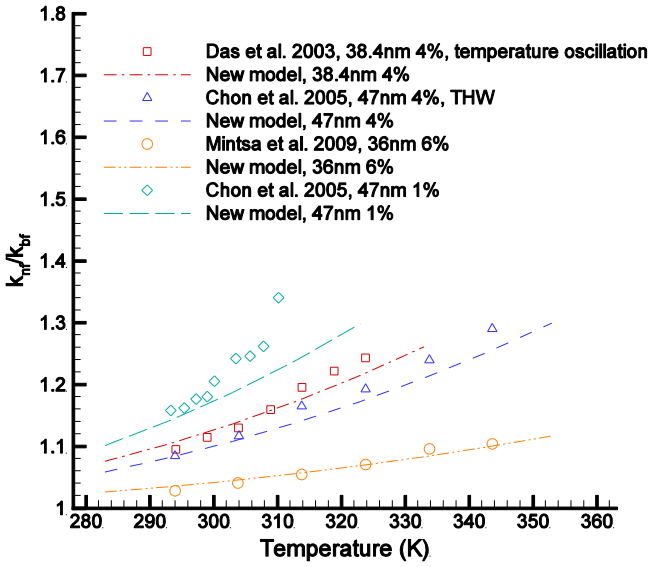

Figure 2.10: Comparison between new model and experimental data for Al_2O_3-water nanofluids thermal conductivity dependence on volume fraction

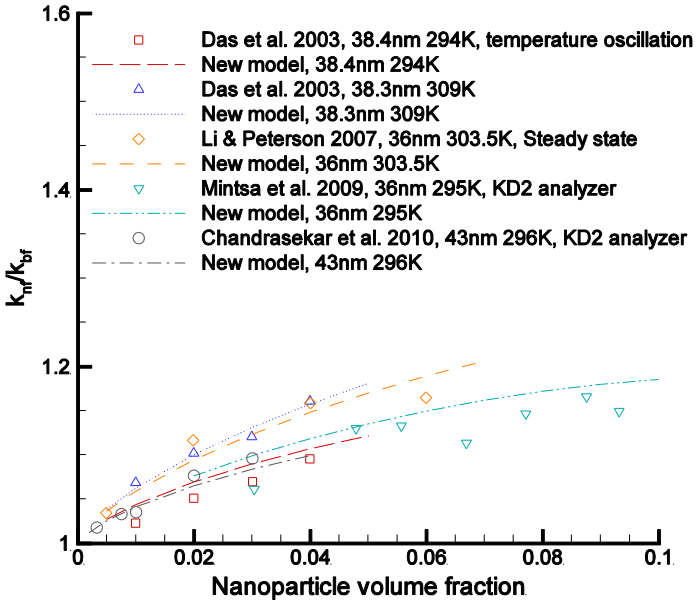

Figure 2.11: Comparison between new model and experimental data for Al_2O_3-water nanofluids thermal conductivity dependence on temperature

dispersion of nanoparticles at higher volume fractions, while the aggregation size predicted by the new model is considerably higher (see Eq. (2.59)). In addition, though the model prediction is slightly higher than the experimental data of Das et al. (2003) for 38.4nm nanoparticles at 294K and under different volume fractions, its predictions agree very well with the data of Mintsa et al. (2009) and Chandrasekar et al. (2010) under similar conditions, i.e., 36nm at 295K, and 43nm at 296K. In fact, it can be seen from Fig. 2.11 that the results by Das et al. (2003) give overall lower thermal conductivities than other experimental data. Hence, we conclude that the new model is able to provide very good predictions for Al_2O_3-water nanofluids for different volume fractions and temperatures.

2.8.2 CuO-water nanofluid comparisons

We then compared the newly developed model predictions with experimental data for the thermal conductivity of CuO-water nanofluids with particle diameters ranging from 25nm to 31nm, volume fractions 0 to 8%, and temperatures 293K to 323K. The aggregation size R_g was determined by Eq.(2.59), and the corrector factor C_c was taken to be 1.0.

The comparisons are shown in Fig. 2.12 and Fig. 2.13, where good agreement has been obtained in both cases. The model predicts slightly higher k_{nf} –values for 31nm nanoparticles at 293K as compared with the data of Mintsa et al. (2009), but the predictions agree well with the results of Das et al. (2003) under similar conditions, i.e., 28.6nm at 294K. Moreover, the predictions match well with the data of Mintsa et al. (2009) for 31nm nanoparticles at 313K. For volume fractions from 1% to 4%, the k_{nf}/k_{bf} values predicted by the new model tend to

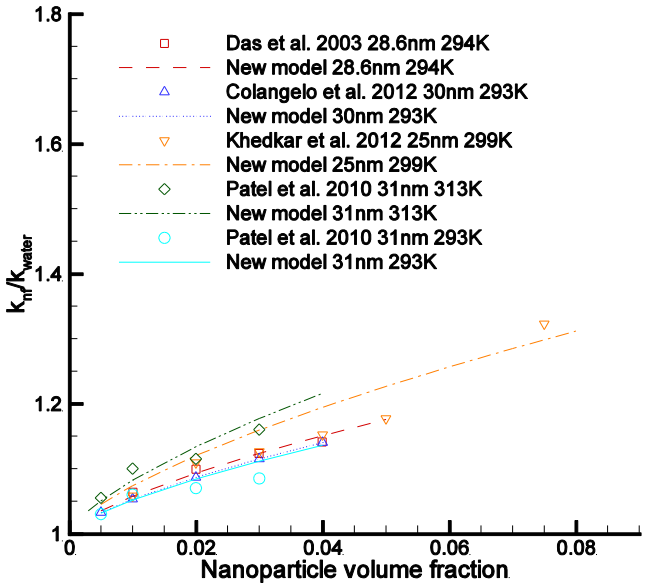

Figure 2.12: Comparison between new model and experimental data for CuO-water nanofluids thermal conductivity dependence on volume fraction

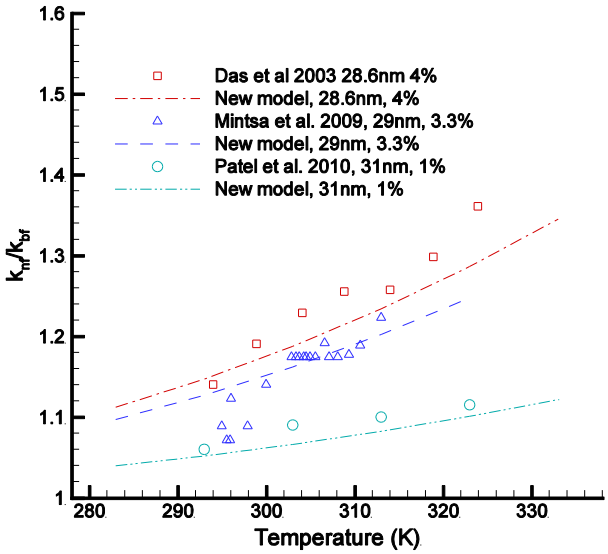

Figure 2.13: Comparison between new model and experimental data for CuO-water nanofluids thermal conductivity dependence on temperature

increase slightly slower than the experimental results, especially for higher volume fractions. However, the experimental results scatter over large ranges and do not always agree with each other (see, for example, Kleinstreuer & Feng (2011)).

It should be noted that in the comparisons for CuO-water nanofluids, a slightly different correction factor, i.e., $C_c = 1.0$, has been used in contrast to the previously used one, $C_c = 1.05$, for Al_2O_3-water nanofluids. This is due to the different physical and chemical properties of these two kinds of nanoparticles. As discussed in previous sections, the aggregation sizes and fractal dimensions may vary for particles of different materials. This accounts mainly for by the minor change in coefficient value.

2.8.3 TiO_2-water nanofluid comparisons

We also compared the predictions of the newly developed model with experimental data for the thermal conductivity of TiO_2-water nanofluids with particle diameters ranging from 21nm to 30nm, volume fractions less than 9%, and temperatures 293K to 338K. C_c has been set to be 0.7 for all cases. Again, overall good agreements have been obtained between model predictions and experimental results (see Figs. 2.14-2.15). We found the experimental data of the thermal conductivities of TiO2-water nanofluids from different studies differ more from each other than for Al_2O_3-water and CuO-water nanofluids. Thus, no single model can match more than a few data sets without, say, adjusting some parameters significantly. Still, the present model can match several of the data sets very well.

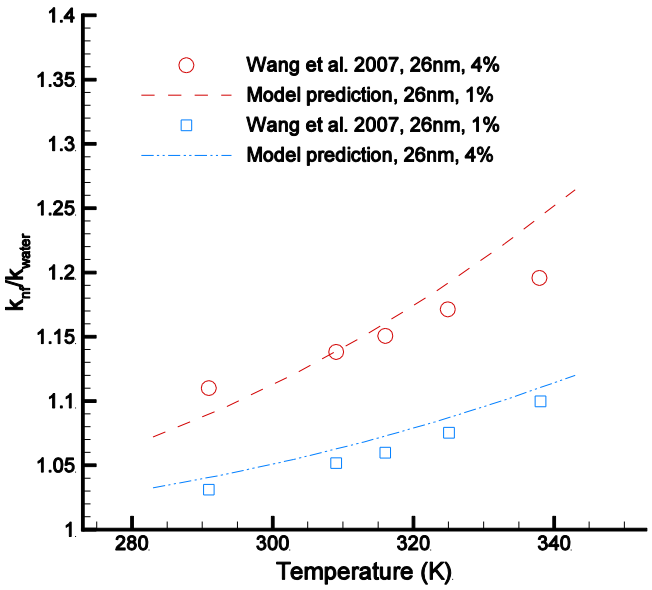

Figure 2.14: Comparison between new model and experimental data for TiO_2-water nanofluids thermal conductivity dependence on temperature

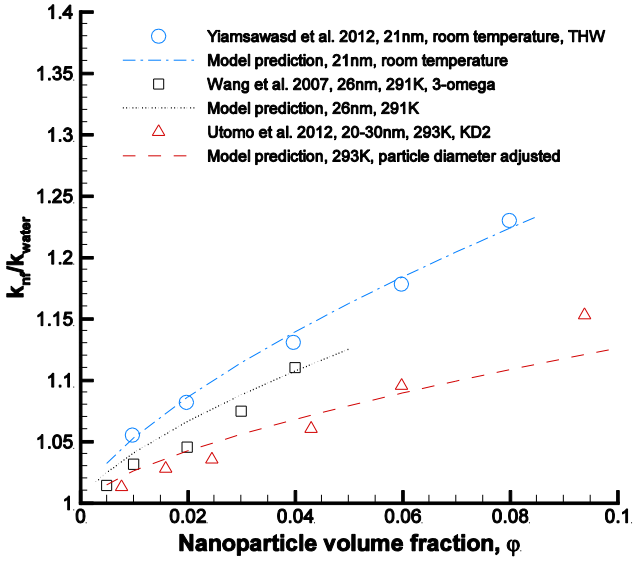

Figure 2.15: Comparison between new model and experimental data for TiO_2-water nanofluids thermal conductivity dependence on volume fraction

2.9 Summary

In this chapter, an improved model for the thermal conductivity of nanofluids, k_{nf} , was developed based on the F-K model proposed by Kleinstreuer & Feng (2012). The derivation of the model and comparison with experimental results for Al_2O_3-water, CuO-water and TiO_2-water nanofluids were provided. Specifically, the new model improves the F-K model by taking into account the otherwise neglected nanoparticle *aggregation effects and thermal contact resistance* at the nanoparticle-base fluid interface. The form of k_{nf} in the F-K model was retained, i.e., $k_{nf} = k_{\text{static}} + k_{mm}$, wherein k_{static} is a modified model expression based on the Maxwell model (Maxwell, 1881), and k_{mm} is derived using the Langevin equation as well as a turbulence-like heat transfer equation which considers the perturbations to the velocity and temperature fields, caused by random Brownian motion of nanoparticle aggregates.

It has been proposed that the enhanced thermal conductivity of nanofluids is due to the combined contributions of three effects, i.e., the Brownian motion effects which intensifies the heat transport in the nanofluid, the aggregation effect which produces fractal like structures that facilitate heat transfer inside the structure, and thermal contact resistance which creates a barrier for heat transfer through the solid-liquid interface that reduces the effective thermal conductivity. The overall effect of the three phenomena provides a nanofluid thermal conductivity that agrees well with experimental data.

The new model provides favorable predictions for Al_2O_3-water, CuO-water, and TiO_2-water nanofluids with nanoparticles ranging from 25nm to 47nm in diameter under temperature range of 293K to 343K and volume fraction less than 10%. The new model is

also suitable for non-spherical particle suspensions with proper settings for geometrical parameters, and can be readily extended to other forms of nanoparticle-liquid pairings.

Chapter 3

NANOFLUID FLOW APPLICATION TO A CONCENTRATION PHOTOVOLTAIC-THERMAL SYSTEM

3.1 Introduction and Overview

As discussed in the previous chapters, nanofluids may have superior heat transfer properties such as enhanced thermal conductivity than the base fluids. In addition, nanoparticle suspensions are more stable than suspensions with micro-size or larger particles, i.e., issues such as filter-clogging and gravity-settling are less likely to occur. Over the past few years there has been an increasing interest in using nanofluids for the improved conversion of solar energy. For example, Mihian et al. (2013) reviewed the applications of nanofluids to solar energy conversion and pointed out that most of the existing studies focused on solar collectors and solar water heaters. More work is necessary to investigate, for example, the effect of using nanofluids for improved efficiencies of concentration photovoltaic-thermal (CPV/T) systems.

In this section, a CPV/T system is proposed to test the performance of a nanofluid in cooling as well as heat recycling. The system is described in Section 3.2 in terms of physical geometries, while the mathematical model is given in Section 3.3. The thermal performance of an Al_2O_3-water cooling system for densely packed photovoltaic cells under low to high

concentrations is numerically investigated in Section 3.4. Specifically, the model features a representative 2-D cooling channel with photovoltaic cells, subject to conjugated heat transfer using turbulent nanofluid flow. The influence of different system design and operational parameters, including required pumping power, on cooling performance and improved system efficiency has been evaluated. Optimal parameter values were found based on minimizing the system's entropy generation. In Section 3.5, a counter-flow double-tube heat exchanger is analyzed for best thermal energy recovery. The impacts of inlet Reynolds number and temperatures of both fluids on the heat exchanger performance have been examined. The efficiency of the electrical and thermal energy co-generation system is determined for different nanofluid working temperatures.

3.2 Physical Description

Figure 3.1 depicts the cooling system as well as possible CPV and CPV/T systems under consideration. Densely packed photovoltaic cells rest on top of a rectangular copper cooling channel via a layer of solder and electric insulator (to prevent electric leakage), respectively. An Al_2O_3-water nanofluid flows through the channel to maintain a high efficiency cell operation and avoid excessive cell temperatures. To make the model computationally tractable, steady-state flow and constant sun radiation input were assumed. Furthermore, neglecting variations at the span-wise (lateral) direction reduces the model to be two-dimensional (see Fig. 3.2). The cooling channel was extended long enough to ensure hydrodynamically fully-developed flow condition upon the entrance of the heat transfer part.

Figure 3.3 depicts a double-tube counter-flow heat exchanger, which will demonstrate a simple yet effective example of how the energy collected in the cooling system can be reused. The hot nanofluid leaving the cooling channel will be directed to the heat exchanger for warm-water recovery. The double-tube heat exchanger has geometric dimensions of $R_{id} = 4\text{mm}$, $R_{od} = 5\text{mm}$, and $R_{\text{annular}} = 7.5\text{mm}$, as shown in Fig. 3.3. The inner tube is made of copper with a wall thickness of 1mm, while the outer tube is thermally insulated. Again, steady-state fluid flow and heat transfer were assumed.

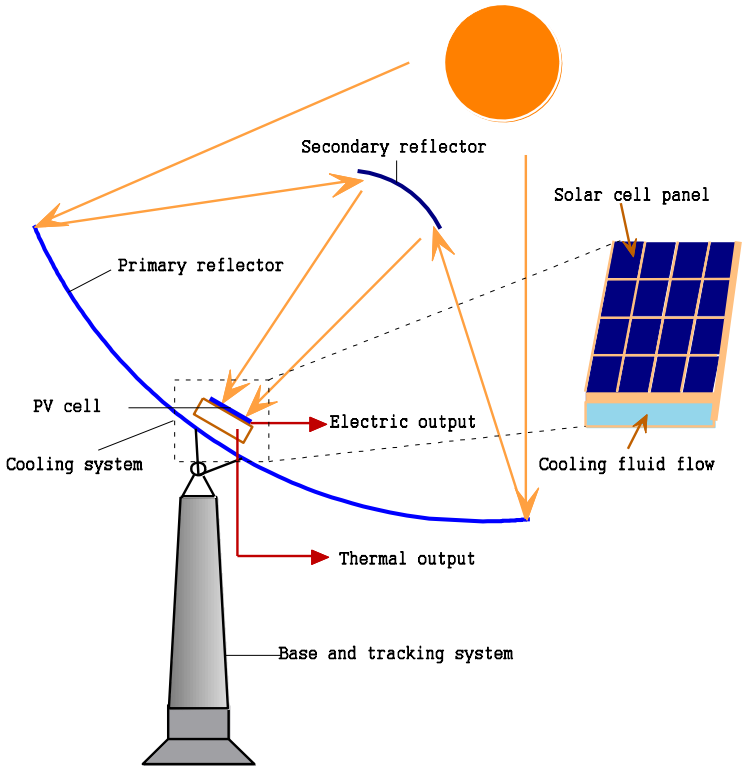

Figure 3.1: Physical model of the CPV receiver and the cooling system

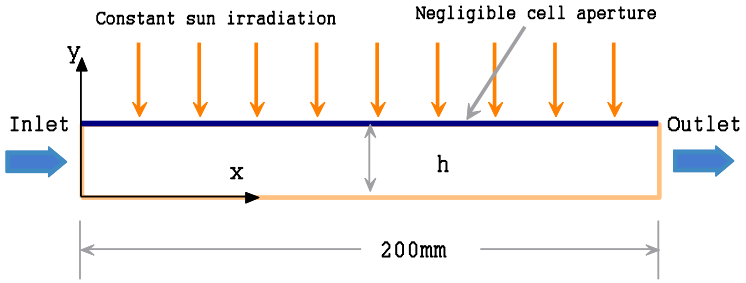

Figure 3.2: Simplified model of the cooling channel for the concentrator cell module

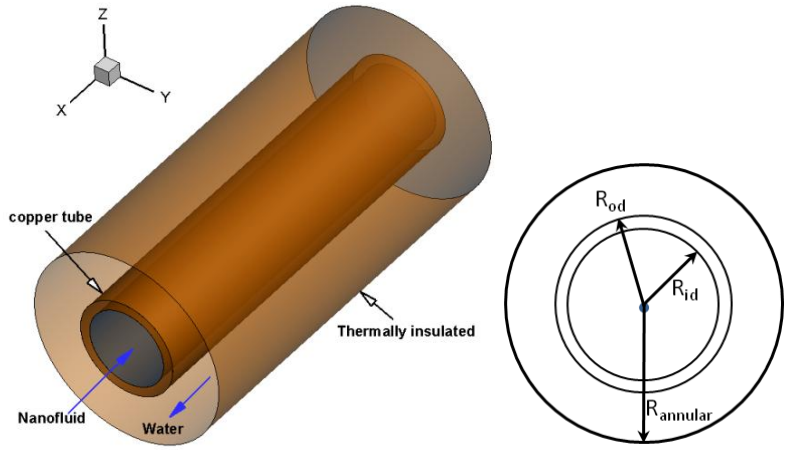

Figure 3.3: Model of the counter-flow, double-tube heat exchanger

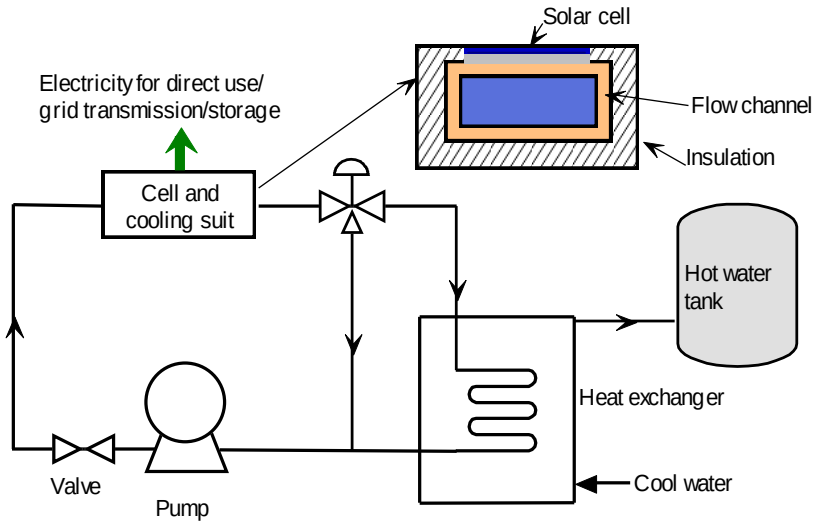

Figure 3.4: Illustration of a concentration photovoltaic/thermal system

A possible combined CPV-T system for a more complete solar energy use is suggested in Fig. 3.4. In this system, the solar cell converts part of the incoming radiation directly into electricity, while most of the remaining energy converts to heat and is being collected by the

circulating nanofluid. Then, the nanofluid transfers thermal energy to streams of water (or air) in a heat exchanger. The hot water can be used for desalination or space heating, and the hot air can cover building heating and air ventilation needs, to give a few examples. It has been shown that for better performance of the solar cells, the cooling nanofluid should have a temperature as low as possible. Thus, the heat exchanger can be extended to maximize the thermal energy recycling and minimize the nanofluid temperature at the outlet of the heat exchanger system.

3.3 Theory

3.3.1 Governing equations

The dilute suspensions of nanoparticles in water used in the present study for cooling of concentration solar cells as well as in the heat exchanger are assumed to be Newtonian mixtures. The Reynolds averaged Navier-Stokes (RANS) equations for steady laminar-turbulent fluid flow and heat transfer can be expressed as follows.

Continuity Equation:

$$\frac{\partial}{\partial x_i}(\rho_{nf} u_i) = 0 \tag{3.1}$$

Momentum Equation:

For laminar flow:

$$\frac{\partial}{\partial x_j}(\rho_{nf} u_i u_j) = -\frac{\partial p}{\partial x_i} + \frac{\partial}{\partial x_j}\left[\mu_{nf}\left(\frac{\partial u_i}{\partial x_j} + \frac{\partial u_j}{\partial x_i}\right)\right] \tag{3.2}$$

For turbulent flow:

$$\frac{\partial}{\partial x_j}(\rho_{nf} u_i u_j) = -\frac{\partial p}{\partial x_i} + \frac{\partial}{\partial x_j}\left[\mu_{nf}\left(\frac{\partial u_i}{\partial x_j} + \frac{\partial u_j}{\partial x_i}\right) - \rho_{nf}\overline{u_i u_j}\right] \tag{3.3}$$

Energy Equation:

For laminar flow:

$$\frac{\partial}{\partial x_i}\left(\rho_{nf} u_i h_{tot}\right) = \frac{\partial}{\partial x_i}\left(k_{nf}\frac{\partial T}{\partial x_i}\right) + \mu_{nf}\Phi \tag{3.4}$$

For turbulent flow:

$$\frac{\partial}{\partial x_i}\left(\rho_{nf} u_i h_{tot}\right) = \frac{\partial}{\partial x_i}\left(k_{nf}\frac{\partial T}{\partial x_i} - \rho_{nf}\overline{u_i h}\right) + \mu_{nf}\Phi - \frac{\partial u_i}{\partial x_j}\left(\rho_{nf}\overline{u_i u_j}\right) \tag{3.5}$$

Here,

$$\Phi = \left(\frac{\partial u_i}{\partial x_j} + \frac{\partial u_j}{\partial x_i}\right)\frac{\partial u_i}{\partial x_j} \tag{3.6}$$

is the energy dissipation term; h_{tot} denotes the mean total enthalpy; $\rho_{nf}\overline{u_i h}$ and $\rho_{nf}\overline{u_i u_j}$ are additional terms due to turbulent fluxes. The velocities are ensemble averaged, where products of fluctuating quantities are denoted with bars and the subscript nf denotes "nanofluid". The Shear Stress Transport (SST) model was employed to approximate the turbulent momentum and energy fluxes. This model is superior to the widely used $k-\varepsilon$ model, as it accounts for the transport of turbulent shear stresses and gives highly accurate predictions in the near-wall region (Menter, 1994), which is especially important for the present application because of the high temperature gradients in this region.

3.3.2 Nanofluid properties

The basic coolant-mixture properties are functions of nanoparticle (NP) volume fraction φ and mixture temperature *T*. Nanoparticles are assumed to be spherical, mono-disperse and forming a homogeneous dilute suspension; although, the effect of NP-aggregates on k_{nf} was considered. In this case of low NP-volume fractions, the nanofluid viscosity, density and heat capacity can be expressed as (Li & Kleinstreuer, 2010):

$$\mu_{nf} = \mu_{bf}\frac{1}{(1-\varphi)^{2.5}} \tag{3.7a}$$

$$\rho_{nf} = \varphi\rho_p + (1-\varphi)\rho_{bf} \tag{3.7b}$$

$$(\rho c_p)_{nf} = \varphi(\rho c_p)_p + (1-\varphi)(\rho c_p)_{bf} \tag{3.7c}$$

where the subscripts bf, p indicate base fluid and particle, respectively.

For the thermal conductivity, the model proposed in Chapter 2 is used. This model divides the thermal conductivity k_{nf} of the nanofluid into two parts: a static part k_{static} similar to Maxwell's model (Maxwell, 1881), and a micro-mixing part k_{mm} due to Brownian motion of nanoparticle aggregate units. Specifically,

$$k_{nf} = k_{static} + k_{mm} \tag{3.8}$$

The static part is a modification of the Maxwell model:

$$k_{static} = k_{bf} \cdot \left(1 + \frac{3\left(\frac{k_a}{k_{bf}} - 1\right)\varphi}{\left(\frac{k_a}{k_{bf}} + 2\right) - \left(\frac{k_a}{k_{bf}} - 1\right)\varphi} \right) \tag{3.9}$$

The micro-mixing part is given by

$$k_{mm} = 19631 \cdot C_c \varphi \frac{\kappa_B \tau_a}{m_a} \left(\rho c_p\right)_{nf} (\overline{T} \cdot ln\overline{T} - \overline{T}) \tag{3.10}$$

The nanoparticle thermal conductivity in the original Maxwell model is replaced by the effective thermal conductivity of the aggregate unit k_a:

$$k_a = k_{de} \cdot \frac{3 + \varphi_b \left[2\beta_{11}\left(1 - L_{11}\right) + \beta_{33}\left(1 - L_{33}\right) \right]}{3 - \varphi_b \left(2\beta_{11} L_{11} + \beta_{33} L_{33} \right)} \tag{3.11}$$

$$\begin{aligned} k_{de} = {} & (3\varphi_{de} - 1)k_{peff} + (2 - 3\varphi_{de})k_{bf} \\ & + \sqrt{[(3\varphi_{de} - 1)k_{peff}]^2 + [(2 - 3\varphi_{de})k_{bf}]^2 + 2[2 + 9\varphi_{de}(1 - \varphi_{de})]k_{peff} k_{bf}} \end{aligned} \tag{3.12}$$

where the effective thermal conductivity of the nanoparticles including the thermal contact resistance, k_{peff}, is given as

$$k_{peff} = \frac{k_p}{1 + R_K k_p / d_p} \tag{3.13}$$

In these equations, k_{de} is the effective thermal conductivity of the mixture of base fluid and dead ends particles, φ_{de} is the volume fraction of dead ends particles in an aggregate unit, φ_b is the volume fraction of backbone particles in an aggregate unit, L_{ii} and β_{ii} are parameters appearing in the derivation of the effective thermal conductivity of arbitrary isotropic particulate composites with interfacial thermal resistance. The readers are referred to Section 2.5 for a complete explanation of the meanings of these parameters. Moreover, R_K is the Kapitza resistance, ρ is the density, c_p is the specific heat capacity, $\bar{T}$ is the time averaged temperature. The subscripts nf, bf, p, and a denote nanofluid mixture, base fluid, nanoparticle, and aggregate unit, respectively. C_c is a correction factor which differs among different nanoparticle-base fluid parings. But the value is around unity for all the parings tested in Section 2.8. The characteristic time interval τ_a is expressed as:

$$\tau_a = \frac{m_a}{3\pi\mu_{bf} R_g} \tag{3.14}$$

where R_g is the radius of gyration of a fractal structure, while the average radius of the aggregate unit is:

$$R_g = 2.5 d_p \sqrt{\frac{\varphi}{0.01}} \cdot \sqrt{\frac{T_0}{\bar{T}}} \tag{3.15}$$

in which d_p is the nanoparticle diameter, and T_0 is the reference temperature, which is set to be 273.15K.

The temperature-dependent properties of the base fluid, i.e., water in the present study, can be expressed as (Feng & Kleinstreuer, 2012):

$$\rho_{\text{water}} = 1000 \cdot \left(1 - \frac{(\tilde{T} + 15.7914)}{508929.2 \cdot (\tilde{T} - 205.0204)} \cdot (\tilde{T} - 277.1363)^2 \right) \left[\frac{\text{kg}}{\text{m}^3} \right] \quad (3.16a)$$

$$c_{p,\text{water}} = 9616.873445 - 48.7364833 \cdot \tilde{T} + 0.1444662 \cdot \tilde{T}^2 - 0.000141414 \cdot \tilde{T}^3 \left[\frac{\text{J}}{\text{m}^3 \cdot \text{K}} \right] \quad (3.16b)$$

$$\mu_{\text{water}} = A_1 \cdot 10^{A_2/(T - A_3)} \left[\frac{\text{kg}}{\text{m} \cdot \text{s}} \right] \quad (3.16c)$$

$$k_{\text{water}} = -1.1245 + 0.009734 \cdot \tilde{T} - 0.00001315 \cdot \tilde{T}^2 \left[\frac{\text{W}}{\text{m} \cdot \text{K}} \right] \quad (3.16d)$$

where $\tilde{T} = T / (1[K])$ is the non-dimensional temperature, A_1, A_2, and A_3 in Eq. (11c) are constants with values of 2.414×10^{-5}, 247.8, and 140, respectively (Fox et al. 2004).

3.3.3 Entropy generation

Thermodynamic optimization for a system or device aims to minimize the system entropy generation S_{gen} for the given objective of obtaining optimal geometry and operational conditions (Ratts & Raut, 2004). The entropy generation of a system is indicative of the amount of work wasted during operation. In the case of convection heat transfer, the entropy-generation rate per unit volume (S_{gen} in W/K m^3) can be expressed as (Kleinstreuer, 2010):

$$S_{gen} = S_{gen}(\text{thermal}) + S_{gen}(\text{friction}) \quad (3.17)$$

Clearly, Eq. (12) encapsulates the irreversibilities due to heat transfer and frictional effects, where

$$S_{gen}(\text{thermal}) = \frac{k}{T^2}\left[\left(\frac{\partial T}{\partial x}\right)^2 + \left(\frac{\partial T}{\partial y}\right)^2 + \left(\frac{\partial T}{\partial z}\right)^2\right] \tag{3.18}$$

and

$$\begin{aligned} S_{gen}(\text{frictional}) &= \frac{\mu\Phi}{T} = \frac{\mu}{T}\left(\overline{\Phi} + \Phi'\right) \\ &= \frac{\mu}{T}\left[\left(\frac{\partial \overline{u_i}}{\partial x_j} + \frac{\partial \overline{u_j}}{\partial x_i}\right)\frac{\partial \overline{u_i}}{\partial x_j} + \overline{\frac{\partial u_i}{\partial x_j}\frac{\partial u_i}{\partial x_j}}\right] \end{aligned} \tag{3.19}$$

3.4 Solar Cell Cooling

3.4.1 Reduced governing equations

For the 2-D geometry as shown in Fig. 3.2, the governing equations reduce to:

$$\frac{\partial}{\partial x}(\rho_{nf}u)+\frac{\partial}{\partial y}(\rho_{nf}v)=0 \tag{3.20a}$$

$$-\frac{\partial p}{\partial x}+\frac{\partial}{\partial y}\left(\mu_{nf}\frac{\partial u}{\partial y}\right)-\frac{\partial}{\partial x_j}\left(\rho_{nf}\overline{u_i u_j}\right)=0 \tag{3.20b}$$

$$\frac{\partial}{\partial x_i}\left(\rho_{nf}u_i h_{tot}\right)=\frac{\partial}{\partial x}\left(k_{nf}\frac{\partial T}{\partial x}\right)+\frac{\partial}{\partial y}\left(k_{nf}\frac{\partial T}{\partial y}\right)+\mu_{nf}\left(\frac{\partial u}{\partial y}\right)^2-\frac{\partial}{\partial x_i}\left(\rho_{nf}\overline{u_i h}\right)-\frac{\partial u_i}{\partial x_j}\left(\rho_{nf}\overline{u_i u_j}\right) \tag{3.20c}$$

Equation (12) can be partially expressed as:

$$S_{gen}(\text{thermal})=\frac{k}{T^2}\left[\left(\frac{\partial T}{\partial x}\right)^2+\left(\frac{\partial T}{\partial y}\right)^2\right] \tag{3.21}$$

and

$$\begin{aligned} S_{gen}(\text{frictional}) &= \overline{S_{gen}(\text{frictional})}+S_{gen}(\text{frictional})' \\ &= \frac{\mu}{T}\left(\frac{\partial \bar{u}}{\partial y}\right)^2+\frac{\mu}{T}\Phi' \end{aligned} \tag{3.22}$$

as the frictional entropy generation is directly proportional to viscous dissipation. Bejan (1996) pointed out that for turbulent flow the dissipation due to mean flow is roughly the same as that due to turbulent fluctuation, with the ratio of the two slowly decreasing as the Reynolds number increases. It turns out that the frictional entropy generation rate is a negligible part of S_{gen}, unless the Reynolds number is very large. Thus, in the present study

the correlation in Bejan (1996) is curve-fitted with the frictional entropy generation rate expressed as a function of $\overline{S_{gen}(\text{frictional})}$ and Re.

3.4.2 Boundary conditions

The boundary conditions include a fully-developed velocity profile at the inlet (which was guaranteed by extending the channel before the heat transfer region) and zero gauge-pressure at the outlet. The bottom channel wall was assumed to be adiabatic and the no-slip condition was applied to all channel walls. The incoming concentrated solar radiation converts partly to electricity and partly to heat which is dissipated through active cooling. Hence the resulting heat flux equals to:

$$q_{cell} = C \cdot q \cdot \alpha \cdot (1-\eta) \tag{3.23}$$

Here C=200 is the concentration ratio, q is the heat flux of 1-sun irradiation (i.e., 1000W/m^2 in this case), $\alpha = 0.9$ is the absorptivity (Ge & Na, 1989), and η is the cell efficiency (Evans & Florschuetz, 1978), i.e.,

$$\eta = \eta_{ref}\left[1-\beta(T_{cell}-T_{ref})\right] \tag{3.24}$$

The reference efficiency η_{ref} and temperature coefficient β varies between published studies, depending on cell materials and test conditions (Skoplaki & Palyvos, 2009). We used a reference efficiency of 0.2 at a reference temperature of T_{ref} =298K to represent typical crystalline silicon solar cells. The temperature coefficient β is equal to 0.0045K^{-1}. For multijunction solar cells, the efficiency could reach almost 40%, and the temperature coefficient is usually different from that for silicon solar cells. It is usually suggested that for

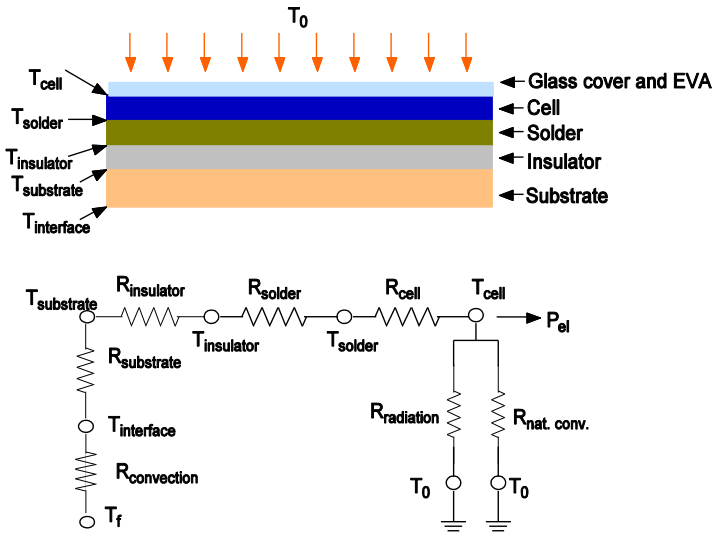

Figure 3.5: Equivalent thermal circuit of cell, mounting and cooling system

high concentration photovoltaic systems, multi-junction solar cells be used to maximize the electrical energy conversion efficiency. However, the characteristics of the temperature dependent efficiency of crystalline silicon solar cells are more thoroughly studied. Moreover, the current study focuses mainly on the medium concentration ratio range. Hence we used crystalline silicon solar cells with the properties specified above. It should be noted that the heat flux added to the heat transfer surface varies local cell temperature because of the cell efficiency is varying with temperature.

1-D heat conduction from the cell surface to the forced convection interface was assumed. The configuration can be represented by the equivalent thermal circuit shown in Fig. 3.5, where R denotes a thermal resistance. The temperature T_0 captures the ambient temperature, while $T_{\text{substrate}}$, $T_{\text{insulator}}$, and T_{solder} are the temperatures on the top surface of the copper substrate, the electric insulator, and the solder layer, respectively. T_{cell} denotes the cell

surface temperature which is used for calculating the cell efficiency. The thickness and thermal properties of each layer are listed in Table 3.1 (Sala, 1989).

The cell loses heat to the ambient through the ethylene-vinyl acetate (EVA) layer and glass cover because of thermal radiation and natural convection at typical rates of 400W/m^2 and 2800W/m^2 (i.e., about 0.3% and 2% of the total input heat flux), respectively. It was assumed that the transmissivity of the glass cover and the EVA layer are both 100%.

Table 3.1: Properties of a nanofluid-cooled encapsulated cell

Material	**Thickness**	***k*** **(W·cm^{-2}·°C^{-1})**	***R*** **(cm^2·°C W^{-1})**
Silicon	200μm	1.45	1.38×10^{-2}
Solder	100 μm	0.5	2.0×10^{-2}
Insulator	0.5mm	0.375	1.33×10^{-1}
Substrate(Cu)	2mm	3.85	5.19×10^{-2}

3.4.3 Numerical method and model validation

The governing equations were solved, employing the user-enhanced software package ANSYS-CFX 14 which is based on the control volume method. The computations were performed on a local workstation (DELL PRECISION T7500). A typical case (i.e., for L=20mm and h=10mm) contains around 157000 structured mesh elements with 240,000 nodes. To better resolve the larger velocity and temperature gradients near the boundaries, the near wall mesh was refined by a factor of 1.08. The y^+-coordinate was kept under unity. The convergence criterion was 1×10^{-6} for the average residual for mass, momentum and heat transfer. Mesh independence was examined and verified by decreasing the mesh size to one half, which produced a maximum result change of less than 1%. Additional model validation

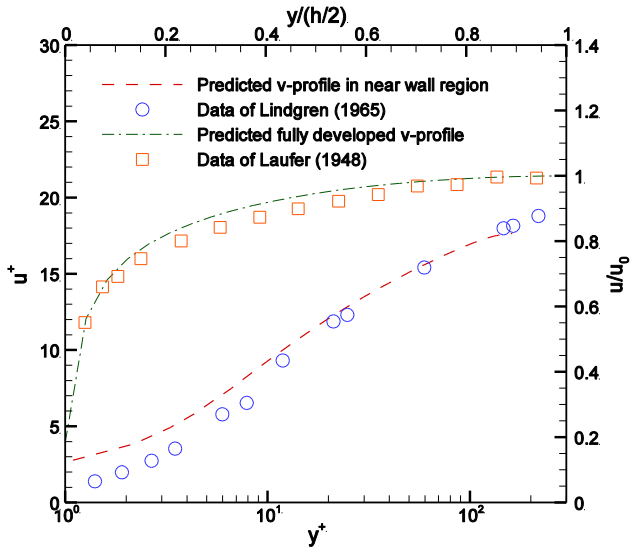

Figure 3.6: Model validation of dimensionless velocity profile in fully developed region and in the near wall region. $y^+ = y \cdot v^* / \nu$ and $u^+ = \bar{u} / v^*$ where $v^* = (\tau_w / \rho)^{1/2}$

was achieved by comparing numerical results of the velocity distribution and heat transfer coefficient with experimental data.

To validate the numerical model, the velocity profile of the base fluid was compared to the experimental data of Laufer (1948). The inlet Reynolds number defined as $\mathrm{Re} = \rho u_m \cdot h / \mu_{nf}$ was set to be 6150, which is equal to the test parameter in the experiment. Figure 3.6 shows a good agreement between the two. The near-wall velocity profile was also compared with the experimental data of Lindgren (1965). The numerical prediction matches well with the experimental data except at the region very near the wall (see Fig. 3.6). The Lindgren experiments were conducted in pipes while for the current study flow between parallel plates was considered. Although correlations developed for pipes also apply for the

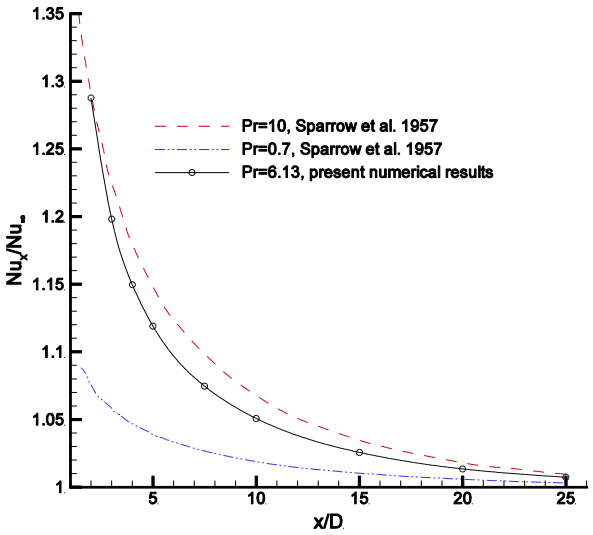

Figure 3.7: Comparison of axial Nusselt number ratio

latter (Rohsenow et al., 1998), minor variation should exist. Thus, we consider the present numerical model to be accurate enough.

To further validate the numerical model, we computed the local Nusselt numbers at different axial locations for a simple case: $10^5 W/m^2$ constant flux applied to both walls cooled by water at $Re=5\times10^4$. Fig. 3.7 provides the Nusselt number as a function of x/D, where D is the hydraulic diameter of the channel. The model prediction with Pr=6.13 lies in-between the theoretical solutions for the Pr = 0.7 and Pr = 10 cases, as given by Sparrow et al. (1957) for a circular tube. Again, Rohsenow et al. (1998) suggested that the turbulent heat transfer correlations for circular tubes also apply to parallel flat plates if Pr>0.7. Thus the present model also predicts heat transfer accurately.

3.4.4 Results and discussion

The effects of various geometrical and operational parameters on the cell efficiency under the impact of 200 effective suns on a densely packed concentrated photovoltaic receiver of 20cm×20cm size were analyzed. As coolants, pure water as well as Al_2O_3-water nanofluid, with nanoparticle diameter of 38.4nm, were considered to evaluate the effects of nanoparticle volume fraction, nanofluid inlet Reynolds number, nanofluid inlet temperature, and channel height.

Nanofluid performance. Nanofluids generate better heat transfer performances than the base fluids alone, due to higher thermal conductivities resulting from Brownian motion effects. This should translate into higher cell efficiencies (i.e., lower cell temperature) for concentrated-cell cooling. This can be seen from Fig. 3.8, which indicates the superiority of nanofluid over pure water in terms of cooling performance. Clearly, the use of a nanofluid yields higher cell efficiency than pure-water cooling, but this difference becomes smaller when the Reynolds number increases.

The thermal conductivity of a nanofluid increases with the nanoparticle volume fraction, which leads to a better cooling capacity. Figure 3.9 shows the variation of the cell efficiency *vs.* the nanoparticle volume fraction for a Reynolds number of 3000, a channel-height of 10mm, and a nanofluid inlet temperature of 297K. It is shown in Section 3.4 that 10mm is the optimal channel height for a cooling system for the current thermal loading. As a nanofluid provides a better cooling performance than water, hereafter the alumina-water nanofluid with 4% volume fraction was used to study optimal geometric and operational parameters for a 200-sun concentration.

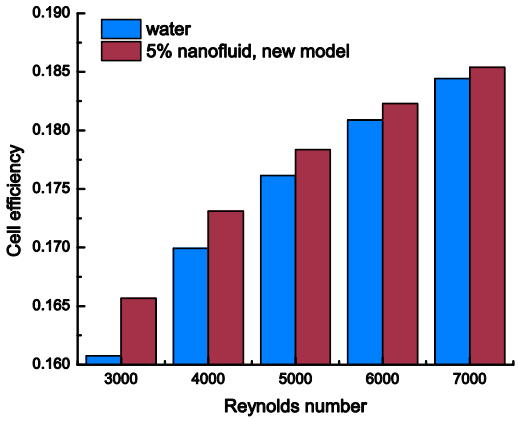

Figure 3.8: Comparison of cell efficiencies using water and nanofluid cooling under different inlet Reynolds numbers

Reynolds number. A large span of Reynolds numbers, i.e., 3000< Re <70000, was considered to investigate their effect on cell efficiency. The channel height and the inlet nanofluid temperature were kept constant at 10mm and 297K, respectively. Fig. 3.10 shows that the cell efficiency increases drastically when elevating the Reynolds number in the lower range, i.e., Re<20000. After that, a Re- increase gains little improvement in cell efficiency. Specifically, in the Re range from 3000 to 20000 the cell efficiency increased by 2.4%, while for 20000 to 70000 the cell efficiency only increased by 0.23%. This is because in the lower Reynolds number range, heat transfer between the wall and the fluid is dominant by forced convection, which depends directly on the flow rate. At a higher Reynolds number range, the cell temperature is already close to the coolant temperature, so there is little to gain from further increasing Re.

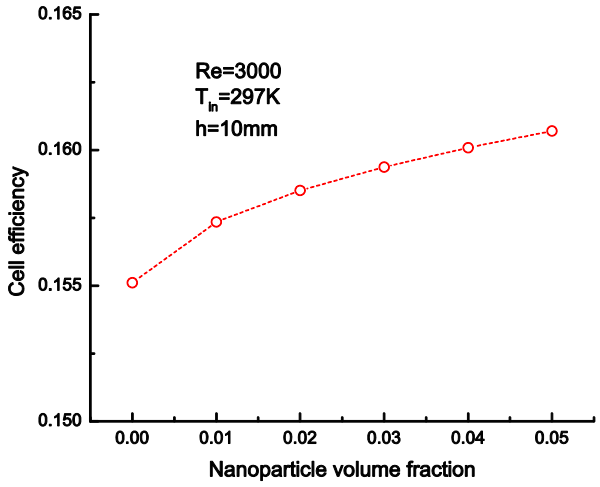

Figure 3.9: Efficiency versus nanoparticle volume fraction

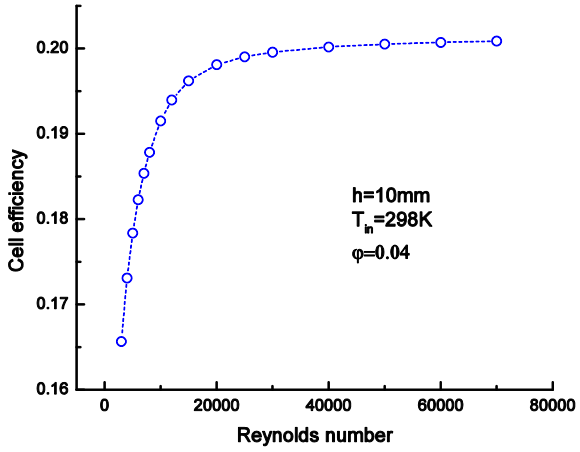

Figure 3.10: Cell efficiency versus Reynolds number

The efficiency curve of Fig. 3.10 indicates a suitable Reynolds number for which the net electrical output is relatively high and the necessary pumping power input is quite low. Hence, to determine such a Reynolds number, a gross power output, i.e., P_{gross} = electrical

power output – pumping power input, can be defined. Figure 3.11 depicts P_{gross} as well as the input-to-output power ratio *vs.* Reynolds number. The grey band denotes the region where the most suitable Reynolds numbers appear. The pumping power accounts for only a small part of the power generation by the photovoltaic cell, even if tripled to account for additional pipe head loss and/or lower pump efficiency. This suggests that the use of active cooling allows for significant electricity output and provides useful thermal energy while causing little penalty.

Figure 3.11 shows the gross power output of the system at a constant concentration ratio, i.e., C=200. In fact, same analysis can be applied to different concentration ratios. For example, Fig. 3.12 shows the suitable Reynolds numbers for different concentration ratios ranging from low concentration (C=100) to high concentration (C=1000). Same pattern exists for all concentration ratios studied, i.e., there is a suitable Reynolds number for any specific concentration ratio, above which further increase of Re harm the system efficiency. It should be noted that P_{gross} was normalized with values under different Reynolds numbers for different concentration ratios. Therefore the larger magnitudes of the normalized P_{gross} should not be interpreted as higher gross power output. Also shown in Fig. 3.12 are the ratios of pumping power input to electrical power output. Interestingly, at suitable Reynolds numbers determined by P_{gross}, the power ratio increases with concentration ratio C, as indicated by the arrow in the figure. This is probably due to the raise of the temperature difference between the cell surface and the convective heat transfer surface under higher C values.

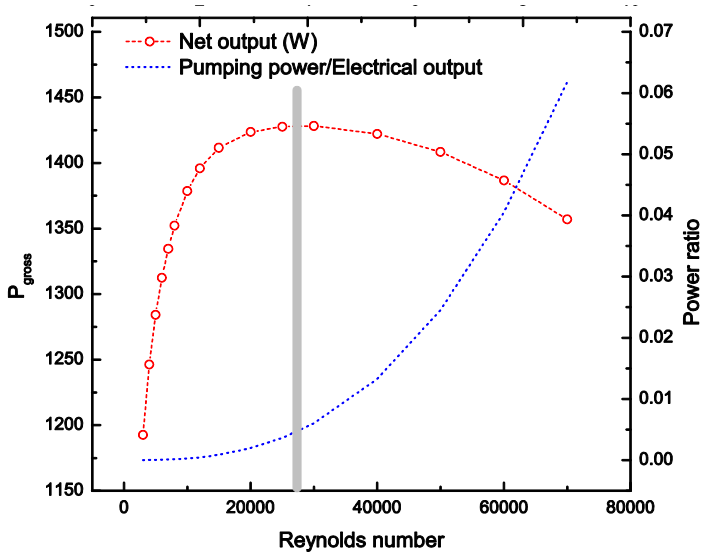

Figure 3.11: Gross power output and input/output power ratio over Reynolds numbers

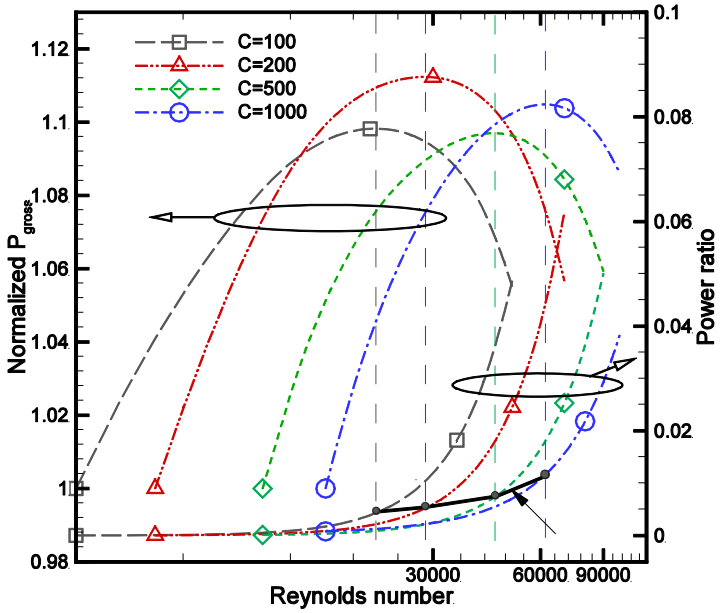

Figure 3.12: Variation of optimal Reynolds numbers in terms of maximum gross power output, as well as input/output power ratios under different concentration ratios

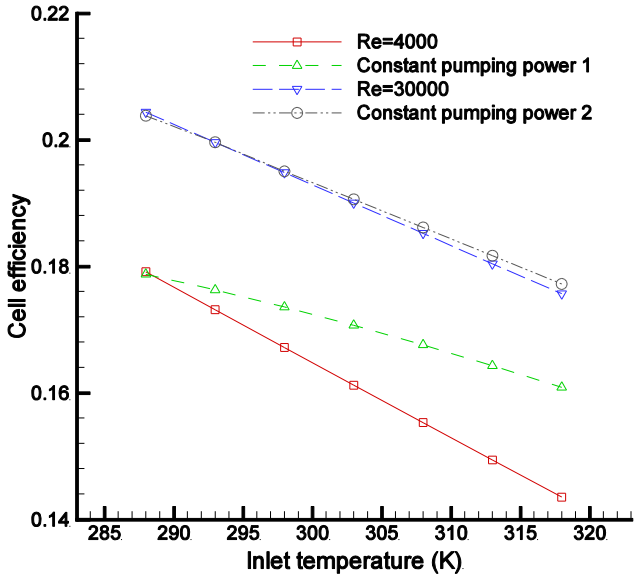

Figure 3.13: Cell efficiency versus nanofluid inlet temperature. The two cases with constant pumping powers adopted the reference pumping powers of Re=4000, T_{in}=288K case, and Re=30000, T_{in}=293K case, respectively

Inlet Temperature. Figure 3.13 shows the cell efficiency as a function of seven different inlet temperatures; again, using the 4% nanofluid in a channel of 10mm height. Two different Reynolds numbers were applied for comparison, where for both cases a lower inlet temperature yields higher cell efficiencies. In fact, a linear relation exists between the nanofluid inlet temperature and the cell efficiency, while the slope is steeper for the lower Reynolds number. Both slopes are smaller than the cell temperature coefficient β=0.0045; hence, a 1K drop of inlet temperature yields a much smaller temperature drop of the cells. It should be noted that for a constant Reynolds number, the volume flow rate of nanofluids for different cases varies because of the temperature-dependent viscosity and density of nanofluids.

For comparison, the cell efficiency *vs.* different inlet temperatures is also plotted in Fig. 3.13 for two pumping powers, i.e., that of the cases of Re=4,000 with T_{in}=25 °C, and Re=30,000 with T_{in}=25 °C. At constant pumping power, the cell efficiency is more sensitive to the nanofluid inlet temperature when the Reynolds number is high. Again, this is due to the temperature-dependent property of nanofluids. In the temperature range between 15°C to 45°C, the nanofluid density almost remains constant, while the viscosity decreases rapidly with rising temperature, leading to higher flow rates for the same pressure drop, and therefore lowers cell temperatures. While the property change has a strong effect on the cell efficiency in the lower Reynolds number range, it is not important in the high Reynolds number range. The reason is that an increase in flow rate has a compromising effect on the cell efficiency within this range. This relation also indicates that the effort to minimize the inlet temperature is imperative when designing the cooling system, implying that the source of the coolant could significantly affect the cell efficiency.

Channel Height. Figure 3.14 provides the pumping power for different channel heights, varying from 2mm to 14mm in 2mm increments, while the cell efficiency remains nearly constant. Again the 4% Al_2O_3-water nanofluid with an inlet temperature of 297K was used. At small channel heights the pumping power drops very fast as the channel height increases; however, when the height becomes larger, the pumping power tends to converge. This can be explained in terms of the pressure drop relation:

$$\Delta p = f \frac{L}{D} \rho \frac{u_m^{\ 2}}{2} \tag{3.25}$$

where f denotes the friction coefficient. The pumping power can be calculated as:

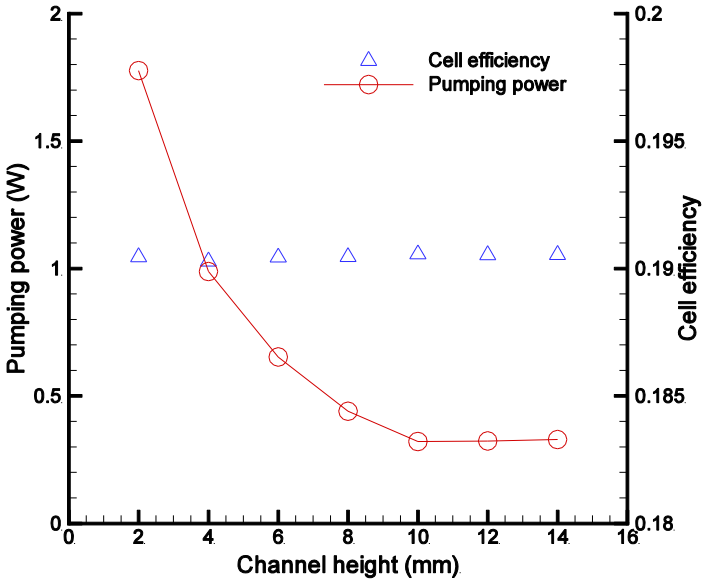

Figure 3.14: Pumping power comparison for varying channel height

Table 3.2: Applied nanofluid flow conditions for different channel heights

Channel height (mm)	2	4	6	8	10	12	14
Reynolds number	2980	5210	7000	8300	9400	11500	13650
Average velocity (m/s)	1.6054	1.4034	1.2571	1.1178	1.0128	1.0326	1.0505

$$P_{pump.} = \Delta p \cdot A_{in} \cdot u_m \tag{3.26}$$

where u_m is the average velocity, and A_{in} is the inlet area. Thus, Eq. (3.26) can be rewritten as:

$$P_{pump} \propto f \cdot u_m^{\,3} \tag{3.27}$$

Table 3.2 lists the Reynolds number and average velocity for each channel height. Although an increase in channel height is coupled to higher Reynolds numbers, the pumping power

decreasesbecause both the friction factor and the average velocity decrease (except for the h=14mm case where the average velocity had a minor increase compared with the h=12mm case). Nevertheless, the decrease of the friction factor apparently counteracted the average velocity increase and reduced the pumping power.

Again, the pumping power curve of Fig. 3.14 indicates a suitable channel height for which the overall system efficiency is high and the necessary pumping power is low. As mentioned, the best overall efficiency means the total output of the system, including the electrical energy directly converted by the PV cells and the available thermal energy collected, is a maximum. Here the entropy-generation analysis is employed to determine such a channel height. Fig. 3.15 shows the thermal and frictional entropy-generation rate in different channels. Both S_{gen}(thermal) and S_{gen}(frictional) decrease with an increasing channel height for h<10mm; but when h>10mm, S_{gen}(thermal) begins to increase while S_{gen}(frictional) keeps decreasing. In fact, the thermal entropy-generation rate is several orders of magnitude higher than the frictional entropy-generation rate; hence, the total entropy-generation rate follows the trend of S_{gen}(thermal). In other words, the energy unnecessarily wasted per unit time, i.e., the waste power, begins to increase if the channel height keeps increasing beyond h=10mm. To determine the optimal channel height, a net power output was defined as:

$$P_{net} = P_{el} - P_{lost} \tag{3.28}$$

where P_{el} is the electrical power output, and P_{lost} is the waste-power which can be calculated via:

$$P_{lost} = \int_{\forall} \left(S_{gen}(thermal) + S_{gen}(frictional) \right) \cdot T d\forall \tag{3.29}$$

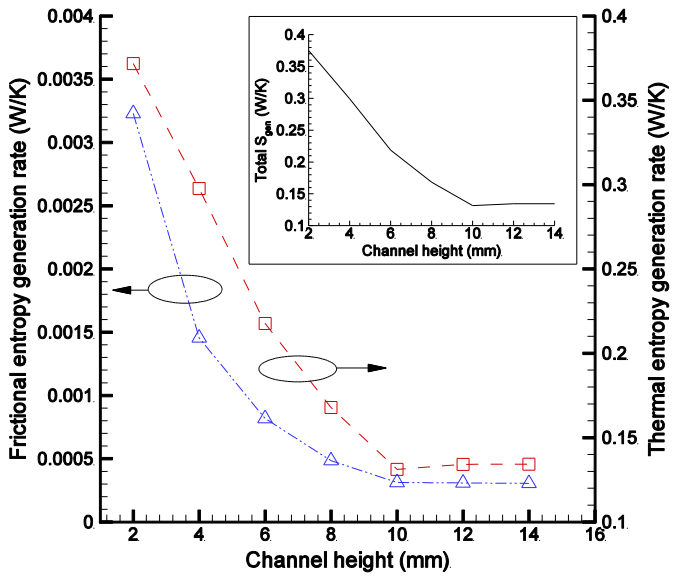

Figure 3.15: Thermal and frictional entropy-generation rate versus channel height

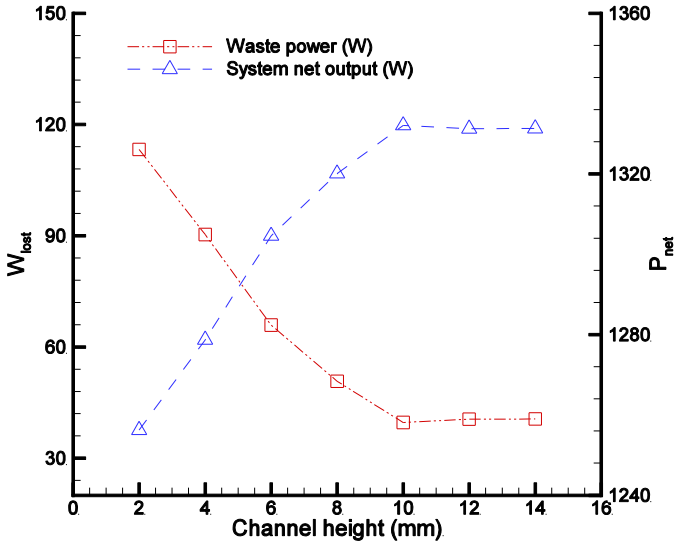

Figure 3.16: Waste power and system net power output for different channel heights

It can be seen from Fig. 3.16 that P_{lost} changes the same way as S_{gen}(thermal) does with an increasing channel height, again because of the different contributions of S_{gen}(thermal) and S_{gen}(frictional) to the total entropy-generation rate. Meanwhile, the net power output changes reversely, as it increases before *h* reaches 10mm and decreases thereafter. Therefore the optimal channel height is 10mm for the 200-sun concentration.

Entropy generation. As mentioned in previous sections, the entropy-generation analysis is a powerful tool in thermal system design. Minimization of the entropy-generation via operational and/or geometrical optimizations has been proved effective (e.g., see the section above). Therefore it is of interest here to analyze the effect of the nanoparticle volume fraction, the inlet Reynolds number, as well as the nanofluid inlet temperatures on the entropy-generation due to both friction and heat transfer. Similar to Fig. 3.15, the entropy generation rates are shown in Figs. 3.17 - 3.19.

Figure 3.17 suggests that at low Reynolds numbers, S_{gen}(thermal) is several orders of magnitude greater than S_{gen}(frictional), which indicates that thermal entropy-generation dominates the cooling process. The entropy-generation rate decreases with the increase of nanoparticle volume fraction, which again indicates that nanofluid cooling provides a better efficiency than pure water, since entropy generation is related to energy loss.

Figure 3.18 plots the entropy-generation rate versus inlet Reynolds number for nanofluids in an h=10mm channel with 4% nanoparticle volume fraction. The frictional entropy-generation rate increases with the Reynolds number because of an enhanced friction effect. On the contrary, S_{gen}(thermal) is smaller at higher Reynolds numbers. Hence an optimal Reynolds number is identified corresponding to minimum total entropy generation.

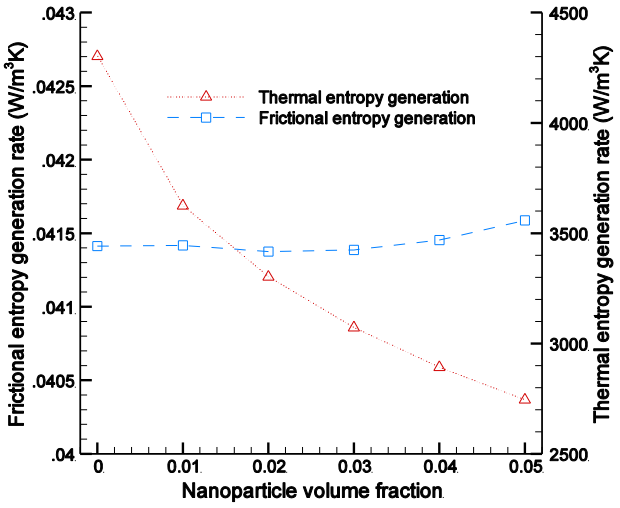

Figure 3.17: System entropy generation versus nanoparticle volume fraction

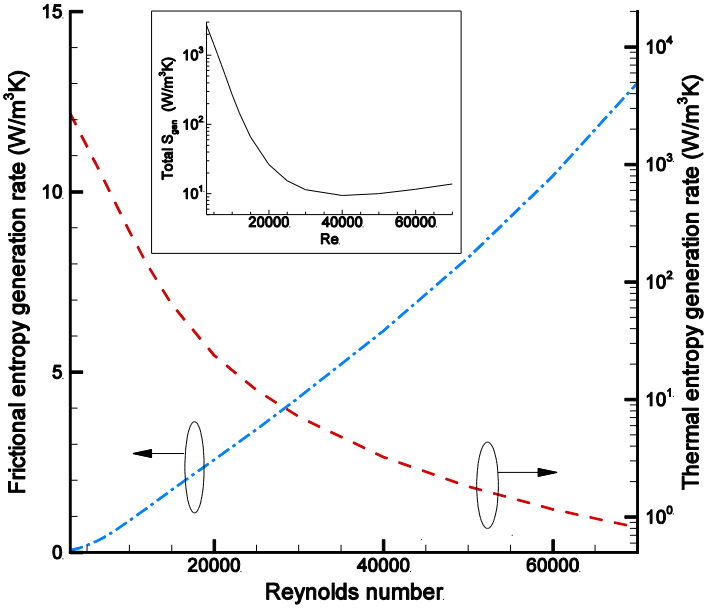

Figure 3.18: System entropy generation versus Reynolds number. *h*=10mm

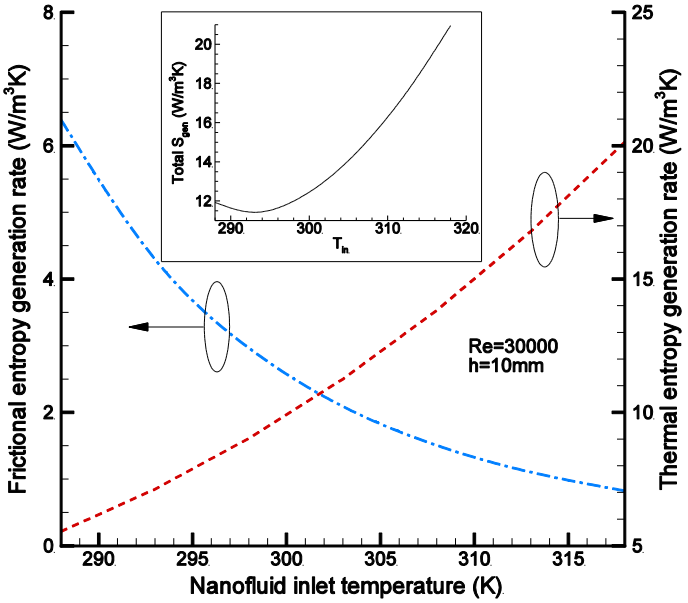

Figure 3.19: System entropy generation versus nanofluid inlet temperature

The thermal entropy-generation rate increases with the nanofluid inlet temperature (see Fig. 3.19). However, the frictional entropy-generation rate decreases at the same time. In fact, as temperature is elevated, the nanofluid viscosity drops, which requires lower flow rate since Re is constant, hence bringing down the S_{gen}(frictional). An optimal inlet temperature is found at which the total entropy generation rate is minimized. The analysis above indicates that higher nanoparticle volume fraction, lower nanofluid inlet temperature are desired for the cooling system.

Combined Photovoltaic-Thermal System application. The above analyses were mainly devoted to the application of nanofluid cooling in a high-end CPV system with a focus on improved cell efficiency. Alternatively, a concentration photovoltaic-thermal hybrid system

could make even better use of the incoming solar energy by utilizing the thermal energy collected by the coolant. In fact, in Sect. 3.5 the net power output and entropy generation are discussed based on this consideration. Terrestrial test data using silicon solar cells suggest that a basic hybrid PV-T system can obtain an overall efficiency of nearly 70%, where the thermal efficiency accounts for the major part of it, i.e., around 60% (Coventry, 2005). Meanwhile, for multi-junction solar cells, the cell efficiency could reach 30% while the thermal energy contribution still amounts to around 50% (Naegeli, 2013). Therefore, for a more complete use of the solar energy, a combined CPV-T system should be considered. This will be addressed in the following section.

3.5 Thermal Energy Recycling

In this section, to evaluate the performance of heat exchanger as well as the overall efficiency of the CPV-T system, a representative counter flow double tube heat exchanger is analyzed using nanofluid as one of the working fluids. The heat exchanger has radiuses of 4mm, 5mm, and 7.5mm for inner tube, tube outer wall, and annular (see Fig. 3.3). High temperature nanofluid comes from the high-end CPV cooling system, and transfers heat to cold water. The heated water can then be used directly or through a next-step heating for downstream applications. The thermal performance of the nanofluid in the heat exchanger will be compared with that of water.

The function of the heat exchanger is to transfer heat from the hot nanofluid to the cold water. The main concern of the heat exchanger differs from that of the cooling system in such that the heat transfer rate is no longer paramount compared to the amount of heat transferred. In other words, one wants to maximize the heat recovery efficiency, defined as the amount of heat transferred from the nanofluid to water over the amount of heat collected by the nanofluid. For such a purpose, laminar flow may be required to allow more heat transfer time. Clearly, the heat transfer rate is determined by the mass flow rate of the nanofluid, since the heat exchanger also bears the responsibility of cooling the nanofluid. As will be demonstrated later, the mass flow rate of nanofluid at the heat exchanger inlet is small enough for a laminar flow condition. Therefore, for the analyses in the current section, laminar flow will be applied.

3.5.1 Reduced governing equations

For laminar flow, the governing equations of Eq.(3.1-3.2), Eq.(3.4) and Eq.(3.6) were used for the fluie flow and heat transfer in this 3-D double tube heat exchanger. In addition to the heat convection, the steady state heat conduction in the inner copper tube was calculated using Fourier's law:

$$\vec{q} = -k_{\text{copper}} \nabla T \tag{3.30}$$

where $\vec{q}$ is the heat flux per unit area, k_{copper} is the copper thermal conductivity, and ∇T is the temperature gradient.

The entropy generation equations (Eqs. (3.18-3.19)) become:

$$S_{gen}(\text{thermal}) = \frac{k}{T^2}\left[\left(\frac{\partial T}{\partial y}\right)^2 + \left(\frac{\partial T}{\partial z}\right)^2\right] \tag{3.31a}$$

$$S_{gen}(\text{frictional}) = \frac{\mu}{T}\left(\left(\frac{\partial u}{\partial y}\right)^2 + \left(\frac{\partial u}{\partial z}\right)^2\right) \tag{3.31b}$$

Due to symmetry, the governing equations are solved in only a quarter of the geometry (see Fig. 3.20). The boundary conditions are uniform inlet velocity profile, pressure outlet, and adiabatic wall for the annular.

3.5.2 Numerical method and model validation

The governing equations were solved, employing the user-enhanced software package ANSYS-CFX 14 which is based on the control volume method. The computations were performed on a local workstation (DELL PRECISION T7500). A typical case contains about

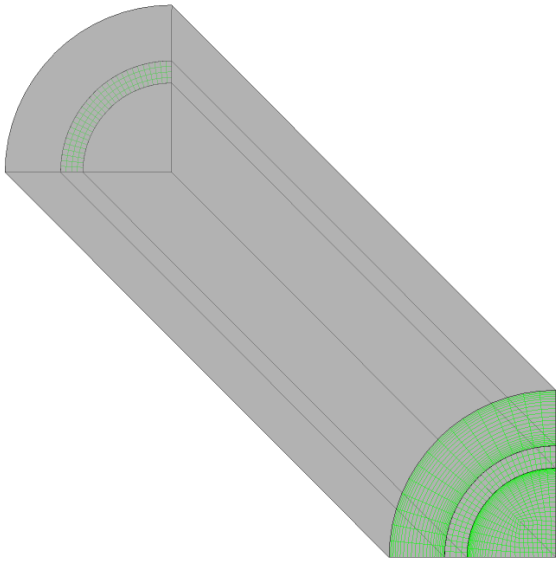

Figure 3.20: Schematic view of the computation domain of the heat exchanger

198,000 structured mesh elements with 224,000 nodes. To better resolve the larger velocity and temperature gradients near the boundaries, the near wall mesh was refined by a factor of 1.08. The convergence criterion was 5×10^{-6} for the average residual for mass, momentum and heat transfer. Mesh independence was examined and verified by decreasing the mesh size to one half, which produced a maximum result change of less than 0.6%. Additional model validation was achieved by comparing numerical results of the fully developed velocity profiles and Nusselt numbers with analytical solutions.

For fully developed flow in circular tubes as well as in annular, the analytical solutions for the velocity profiles are

$$u(r) = 2V\left(\frac{r^2}{R_{id}^2} - 1\right) \tag{3.26a}$$

$$u(r) = -\frac{2V}{R_{\text{annular}}^2 + R_{od}^2 - \dfrac{R_{\text{annular}}^2 - R_{od}^2}{\ln(R_{\text{annular}}/R_{od})}}\left[r^2 - R_{\text{annular}}^2 + \frac{R_{\text{annular}}^2 - R_{od}^2}{\ln(R_{od}/R_{\text{annular}})}\ln(r/R_{\text{annular}}) \right] \quad (3.32b)$$

To validate model, the numerical predictions of the velocity profiles of the base fluid was compared with the analytical solutions for both the inner tube and the annular. The inlet Reynolds number defined as $\mathrm{Re} = \rho u_m \cdot R / \mu_{bf}$ was set to be 200. Figure 3.21 shows good agreements between the two.

To further validate the numerical model, we compare the Nusselt numbers of both the tube and the annular in fully developed region with the analytical values. For circular tubes, the Nu is a constant in fully developed region, i.e., Nu=4.36; while for annular flows, it is suggested that the Nu number be calculated using the hydraulic diameter D_{annular}-D_{od} and be compared with that of rectangular channels (Kays & Crawford, 1993). Here, due to the large aspect ratio of the annular, we compare the Nu number of the annular in fully developed region with Nu of convective heat transfer between parallel plates. The latter has a constant value of Nu=5.385 for the condition of one wall subjected to constant heat flux, and one wall insulated. The computations were conducted with constant wall heat flux of 1.5kW/m^2 applied to the circular tube, as well as to the annular inner wall, while the outer wall of the annular was thermally insulated. Figure 3.22 provides the Nusselt number comparisons under different Reynolds numbers. For both cases, the error is within 1%. Thus the present model also predicts heat transfer accurately.

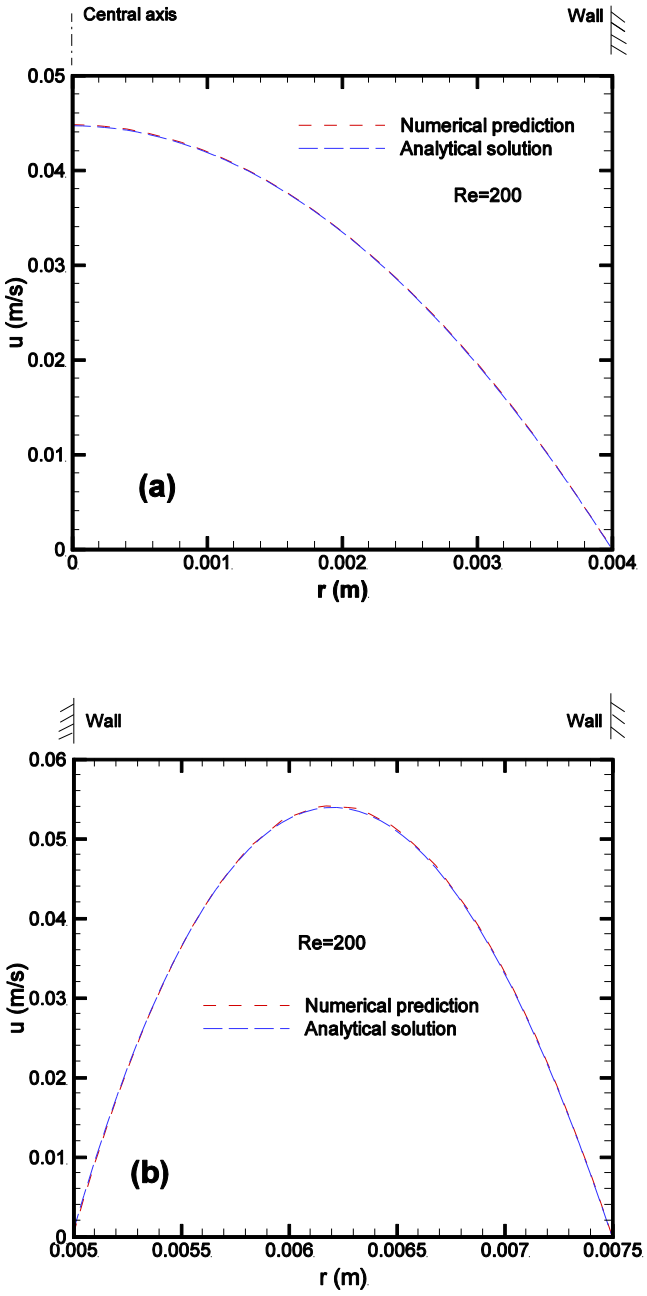

Figure 3.21: Model validation of dimensionless velocity profile in fully developed region, (a) flow in inner tube; (b) flow in annular region.

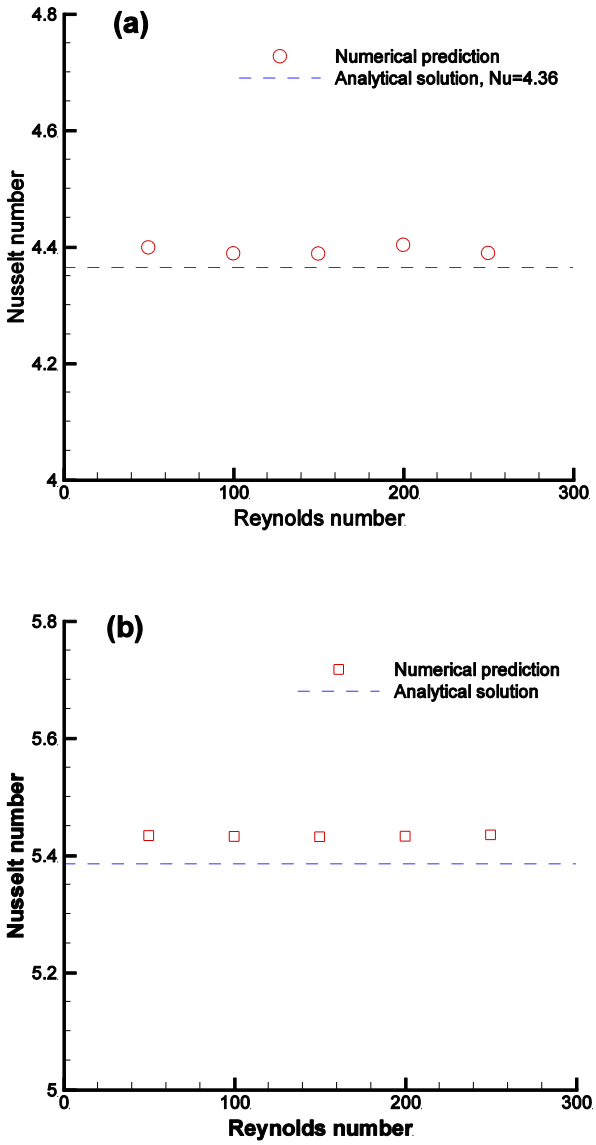

Figure 3.22: Model validation of Nusselt number in fully developed region, (a) inner tube; (b) annular.

3.5.3 Results and discussion

In this section, a counter-flow double-tube heat exchanger is described as an example to demonstrate the performance of the heat exchanger system transferring thermal energy from hot nanofluid flow to a cold water stream. The average convective heat transfer coefficient and Nusselt number of the heat exchanger as well as the entropy generation of the system was evaluated for different conditions. The system efficiency in terms of net energy income (thermal energy income per unit time minus pumping power) has also been evaluated. The overall efficiency of the CPV-T system was evaluated under different fluid income temperatures to determine the optimal operational conditions. To demonstrate the effectiveness of using nanofluid as a heat transfer fluid, the convective heat transfer coefficient and Nusselt number of a water-water heat exchanger are compared with those of the nanofluid-water heat exchanger.

Nanoparticle volume fraction. The convective heat transfer coefficient h and the Nusselt number for nanofluids with particle volume fractions ranging between 0.01 and 0.05 as well as for water have been determined as shown in Fig. 3.23. The inlet temperatures for cold and hot fluids are, respectively, 293K and 333K. It can be seen from Fig. 3.23 that adding nanoparticles in water enhances the heat transfer coefficient significantly, i.e., by up to 23.2% at the 5% volume fraction. However, a slight decrease in Nusselt number was also observed. This indicates that the increase in heat transfer coefficient is due mainly to the enhanced thermal conductivity of the nanofluid. Recall that k_{nf} increases with nanoparticle volume fraction; so, when the rate of increase of k_{nf} exceeds that of h, the Nusselt number will drop, i.e., the convective heat transfer become less important compared to conductive

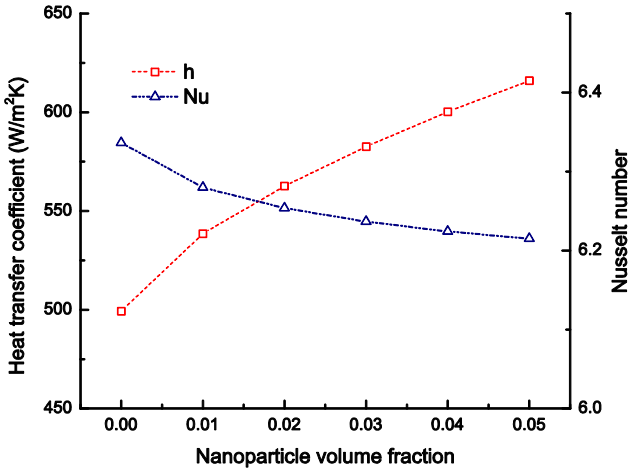

Figure 3.23: Change of convective heat transfer coefficient and Nusselt number (Nu) due to varying nanoparticle volume fraction

heat transfer. Note that the nanofluid loses energy. This again shows that the Nusselt number is not a proper parameter, as has been discussed in section 1.7.1.

The net thermal income of the heat exchanger is the heat flow rate between the two fluids minus the energy waste due to entropy generation. Therefore, similar to Eq. (3.28), it can be expressed as:

$$\dot{Q}_{\text{net}} = \dot{Q} - P_{\text{lost}} \tag{3.33}$$

where $\dot{Q}$ is the rate of heat flow between the two fluids, and P_{lost} is the waste-power. Clearly, a larger $\dot{Q}_{\text{net}}$ is desired as it indicates a higher thermal energy recycling efficiency. The $\dot{Q}_{\text{net}}$ ratio of nanofluid to water shows the relative efficiency. The change of $\dot{Q}_{\text{net}}$ as well as $\dot{Q}_{\text{net}}$ ratio with nanoparticle volume fraction are shown in Fig. 3.24. A thermal efficiency increase

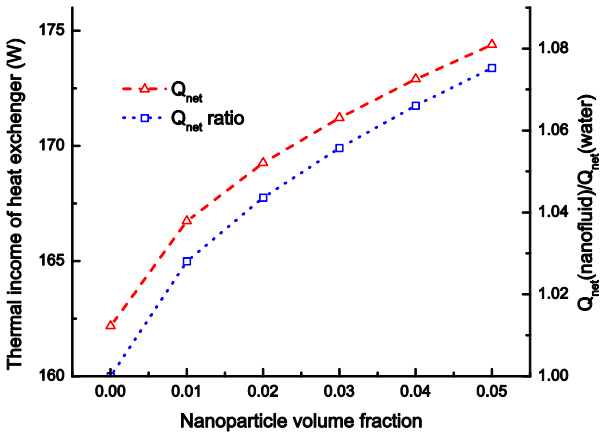

Figure 3.24: Comparison between nanofluid and water in terms of thermal income of heat exchanger

of up to 7.5% can be realized using nanofluids over water, which again demonstrates the superior of nanofluid over water as a heat transfer fluid.

Nanofluid inlet temperature. It has been determined in Section 3.4.4 that for solar cell cooling, lower nanofluid inlet temperature offers higher cell efficiency, suggesting minimized inlet temperature. Meanwhile, as the inlet temperature varies, the nanofluid at the outlet of the cooling channel also changes accordingly. If water at the entrance of the annular of the heat exchanger is kept at a constant temperature of, for example, 293K, different nanofluid inlet temperatures should provide different thermal efficiency of the heat exchanger. Hence it is necessary to investigate the thermal efficiency of the heat exchanger as well as the overall efficiency of the CPV-T system under different nanofluid operating temperatures.

In this section, we evaluate the effect of different *nanofluid* inlet temperatures on the thermal performance of the heat exchanger. Nanofluid in the cooling part can be heated to a

desired temperature by circulation, i.e., the nanofluid leaving the cooling channel will be directed back to the channel inlet and get heated again, until it reaches a desired temperature and be directed to the heat exchanger. The thermal efficiency of the heat exchanger can be determined by dividing the thermal income, $\dot{Q}_{\text{net}}$, over the total energy of the sun irradiation. The overall efficiency of the CPV-T system is then the sum of the cell efficiency and the heat exchanger efficiency:

$$\eta_{\text{overall}} = \frac{P_{net} + Q_{net}}{C \cdot q \cdot A} \tag{3.34}$$

where A is the cell area.

Figure 3.25 shows the changes of efficiencies when the nanofluid inlet temperature of the heat exchanger, T_{in}, varies. The inlet Re of water flowing in the annular was kept at 2000. It can be seen from Fig. 3.25 that though the cell efficiency dropped due to a higher nanofluid temperature, the overall efficiency of the system increased because of the improved thermal efficiency. However, one should notice that with the increase of T_{in}, the flow rate of the hot nanofluid reduces, since the nanofluid would need to run through more circulation cycles cooling the solar cells before being directed to the heat exchanger. The reason for the increase of the thermal efficiency can be seen from Fig. 3.26, which shows the effects of nanofluid inlet temperature on $\dot{Q}_{\text{net}}$ and nanofluid temperature at the outlet of the heat exchanger, T_{out}. A 20K change of T_{in} produces only a 2K change of T_{out}. In other words, at Re=2000, the temperature difference between the nanofluid and water is the main limitation for heat transfer rate; thus higher T_{in} is preferred.

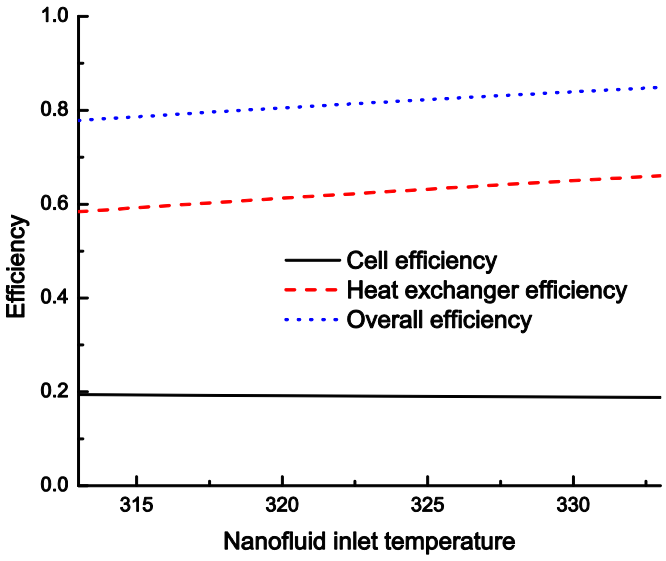

Figure 3.25: System efficiency change due to varying nanofluid inlet temperatures at heat exchanger

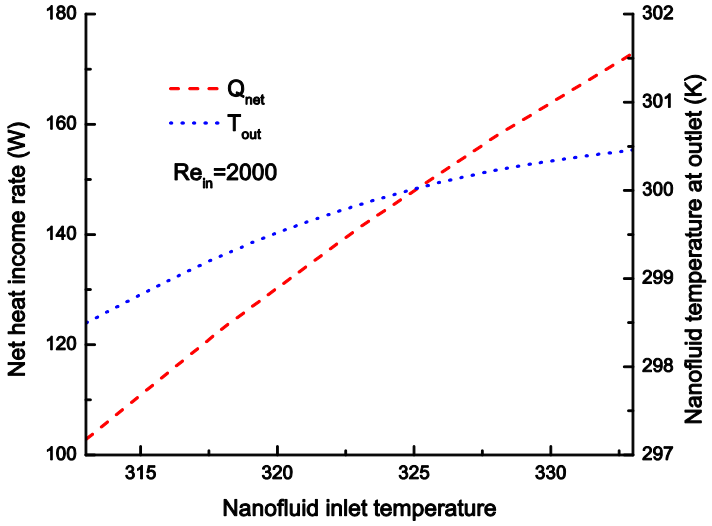

Figure 3.26: Heat exchanger net heat income rates and outflow temperatures under different nanofluid inlet temperatures

Reynolds number. The inlet Reynolds numbers of both the nanofluid in the inner tube and water in the annular affect $\dot{Q}_{net}$ and hence $\eta_{overall}$. However, for a given system the mass flow rate of the nanofluid is determined by the cooling needs, as has been discussed in Sect. 3.4. Although Re_{nf} of the heat exchanger can be adjusted by adding or reducing the number of double tube assemblies in the designing stage, Re_{nf} is fixed once the system is constructed. In this section, we discuss the change in Reynolds numbers on the thermal performance of the heat exchanger.

The changes of convective heat transfer coefficient and Nusselt number with inlet Reynolds number of the inner tube are shown in Fig. 3.27 The inlet Reynolds number for water in the annular space was kept at 2000 for all cases. For comparison, the results for both 4% nanofluid and water as working fluid of the inner tube are shown. It can be seen from Fig. 3.27 that a 4% nanofluid yields higher convective heat transfer coefficients yet lower Nusselt numbers than water. The differences amplify, especially for the Nusselt number, as the Reynolds number increases. This is because of the temperature dependence of the thermal conductivities of both water and nanofluid. The average temperature of the fluid in the inner tube decreases with elevated Reynolds number. Meanwhile, k_{nf} changes faster than k_{water} because of a more sensitive dependence on temperature. As the Reynolds number increases, the thermal income of the heat exchange $\dot{Q}_{net}$ also grows rapidly (see Fig. 3.28). However, this may not be desired when considering the overall efficiency of the CPV-T system.

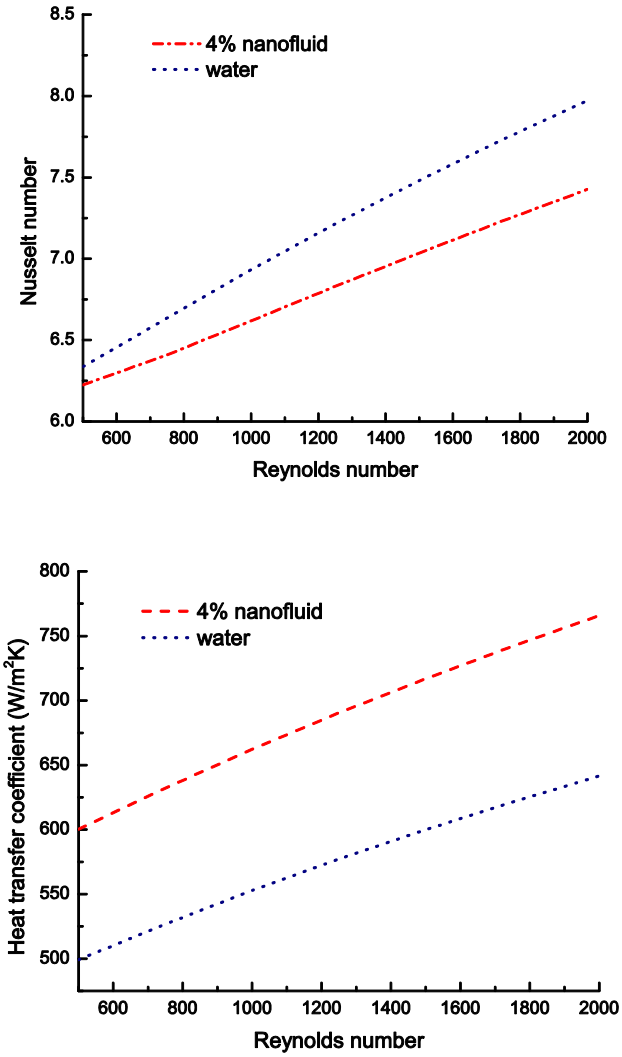

Figure 3.27: Convective heat transfer coefficient and Nusselt number of heat exchanger under different inlet Reynolds numbers

Figure 3.29 shows that the thermal efficiency of the system decreases rapidly with elevated Reynolds number, indicating a reduced overall efficiency of the system. In fact, the improved *h*, *Nu*, and $\dot{Q}_{net}$ values are accompanied by a raised mass flow rate in the inner tube. Therefore, the heat exchange between the fluids in the inner tube and annular becomes

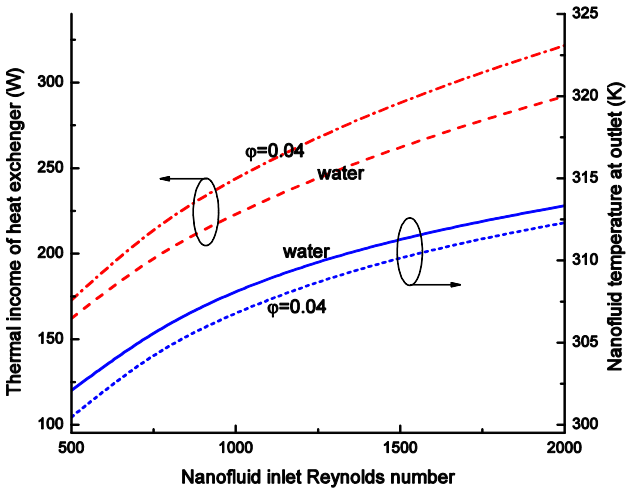

Figure 3.28: Influence of nanofluid inlet Reynolds number on thermal income of the heat exchanger and nanofluid temperature at outlet

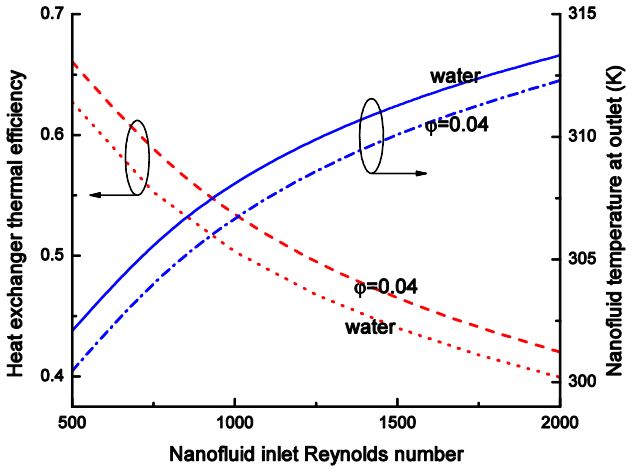

Figure 3.29: Influence of nanofluid inlet Reynolds number on thermal efficiency of the heat exchanger

poorer if the temperature difference of the nanofluid at inlet and outlet of the inner tube are considered (see Figs. 3.28-29).

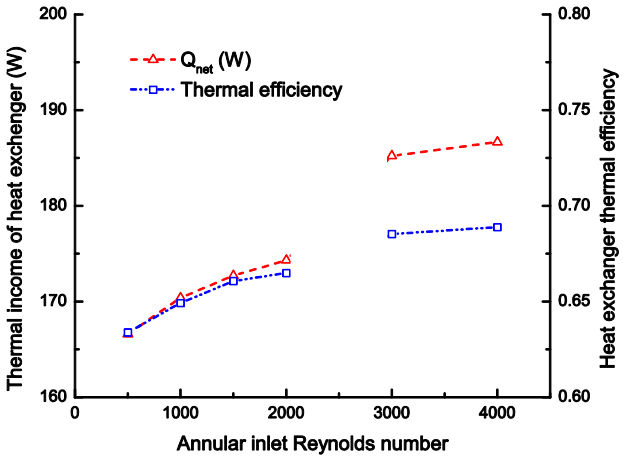

Figure 3.30: Influence of water inlet Reynolds number on thermal income thermal efficiency of the heat exchanger

Figure 3.30 shows the thermal income of heat exchanger, $\dot{Q}_{net}$, and thermal efficiency under different annular inlet Reynolds numbers. Both of them increase with Reynolds number at laminar and turbulent regimes (assuming that the flow becomes turbulent at Re>2300). However, it can be seen from Fig. 3.30 that the thermal efficiency improves only slightly after Re exceeds 2000. The flow can actually be in the transitional regime when Re is between, say, 3000 and 6000, depending on the wall roughness and operational condition. In engineering applications, this regime is usually avoided because of strong mechanical vibration and instability. Therefore an inlet Reynolds number of Re=2000 is the optimal condition for flow in the annular region.

It should be noted that the above analyses on a CPV/T system are under ideal conditions. In reality, there will be heat losses from thermally insulated walls in the cooling and heat recycling sections, as well as from the connection pipes between them. There will also be

heat loss from the top glass layer to the ambient. In addition, the transmissivity of the EVA layer will be less than 100%, and the packing factor of the solar cells will be below unity. Moreover, there water pump operates under limited efficiency. These losses due to imperfections may account for 30-40% of the total income energy from the sun irradiation, according to field testing (Huang et al, 2001). Therefore, a more accurate calculation should consider these factors.

3.6 Summary

The k_{nf} model developed in Chapter 2 was used to study numerically the convective heat transfer characteristics of a nanofluid. Furthermore, the nanofluid cooling capacity as well as heat recycling from a concentration photovoltaic-thermal (CPV-T) system were investigated, with the overall goal of improved CPV-T efficiency.

First, cooling of densely packed CPV cells under high concentration was analyzed using Al_2O_3-water nanofluids. The effects of nanoparticle-volume fractions, inlet Reynolds numbers, nanofluid inlet temperatures, and channel heights on the system performance were determined. The entropy-generation rates of both thermal and frictional causes were evaluated to obtain optimal system parameters. Clearly, nanofluids are superior to pure water in cooling of CPV cells. Specifically, for a 200-sun concentration, an energy balance analysis determined the optimal Reynolds number to be around 30,000. A low nanofluid inlet temperature is desired to achieve high cell efficiency. Varying the channel height yields significantly different entropy-generation rates and pumping power requirements to achieve the same cell efficiency. The entropy-generation analysis showed that the best channel height is 10mm for the current operating condition, i.e., 200-sun concentration with Al2O3-water nanofluid cooling.

Next, heat recycling was investigated using a counter-flow, double-tube heat exchanger. Again, the effects of nanoparticle-volume fractions, inlet Reynolds numbers, and nanofluid/water inlet temperatures on the system performance were determined. As expected, the nanofluid yields performance than water as up to 7.5% more thermal energy can be collected when using the nanofluid with 5%-volume-fraction. A high nanofluid inlet

Reynolds number is not needed as it reduces the overall efficiency of the CPV-T system; meanwhile, a higher, laminar inlet Reynolds number for water in the annular region is desired. Higher nanofluid inlet temperatures will improve the overall efficiency of the system, which can reach 85% for a nanofluid inlet temperature of 333K.

Chapter 4

CONCLUSIONS AND FUTURE WORK

4.1 Conclusions

The following conclusions can be drawn from this study.

- *The key mechanisms enhancing the effective thermal conductivity of nanofluids are nanoparticle aggregation and Brownian-motion induced micro-convection.*
    1. An effective thermal conductivity model, i.e., the F-K model has been improved by including the nanoparticle aggregation effect and the interfacial thermal resistance, in addition to the Brownian motion effect.
    2. The basic units in the nanofluid are fractal-like aggregates, which undergo Brownian motion, and induce micro-scale convection. The aggregation size is a function of the pH-value of the base fluid, the particle volume fraction, the mixture temperature, and the particle properties.
    3. The effective thermal conductivity of the nanofluid is composed of a static part and a dynamic part, both of which are functions of nanoparticle size, nanoparticle-volume fraction, mixture temperature, and particle properties.
    4. The new k_{nf} model is consistent with the F-K model. The aggregation effect becomes negligible as the particle volume fraction decreases.
- *The application of nanofluids to concentration photovoltaic-thermal (CPV/T) systems for improved efficiencies seems to be promising.*

1. A combined model for electrical and thermal energy co-generation using concentration photovoltaic cells and thermal recovery systems has been developed to test the application of nanofluids in improving the CPV/T system efficiency.
2. Nanofluids are superior to pure water in cooling of CPV cells and in heat recovery when using counter-flow double-tube heat exchangers.
3. For different concentration ratios, corresponding optimal Reynolds numbers exist in terms of best system efficiencies, which can be determined using energy-balance analyses.
4. Channel height and nanofluid working temperature are important parameters of the cooling system, while the latter is essential for improving the overall efficiency of a CPV/thermal system.
5. Entropy-generation minimization is a powerful tool in analyzing the thermal performance of the CPV/T system. The frictional entropy generation is comparable to the thermal entropy generation at the optimal Reynolds number for CPV cooling, while the later dominates for heat recycling due to the laminar nature of the fluid flow in tubes.
6. The concentration photovoltaic-thermal system for electrical and thermal energy co-generation significantly improves the energy conversion efficiency when compared to the CPV system.

4.2 Future work

For a better understanding of the mechanisms of conductive and convective heat transfer properties of nanofluids with applications to CPV/T systems, several suggestions are proposed for future studies:

- The newly developed effective thermal conductivity model should be expanded to consider other effects, such as the pH-value of the mixture, size distribution of aggregates, etc.
- The new model shows good predictions for metal-oxide-water nanofluids. However, further studies are needed for metallic-water nanofluids and organic particle-water nanofluids, as well as nanofluids with other types of base fluids.
- The aggregation effect diminishes when the nanoparticle volume fraction decreases. Analyses are needed in terms of the threshold volume fraction for considering the aggregation effect.
- An ideal model has been used to analyze the CPV/T system performance. For more accurate results, this model should be extended to include, for example, the thermal and mechanical losses of the system.
- The monthly energy conversion rate should be evaluated throughout the year for different regions using statistical data, for utility-value purpose. Also, comparisons should be made between nanofluid-based CPV/T system and water-based system.

REFERENCES

Abbasian Arani, A., & Amani, J. (2013). Experimental investigation of diameter effect on heat transfer performance and pressure drop of TiO_2-water nanofluid. *Experimental Thermal and Fluid Science, 44*, 520-533.

Acrivos, A., & Taylor, T. D. (1962). Heat and mass transfer from single spheres in stokes flow. *Physics of Fluids, 5*, 387-394.

Akhavan Zanjani, H., Saffar-Avval, M., Mansourkiaei, M., Ahadi, M., & Sharif, F. (2013). Turbulent convective heat transfer and pressure drop of graphene-water nanofluid flowing inside a horizontal circular tube. *Journal of Dispersion Science and Technology,* (In production)

Azmi, W., Sharma, K., Sarma, P., Mamat, R., Anuar, S., & Dharma Rao, V. (2013). Experimental determination of turbulent forced convection heat transfer and friction factor with SiO_2 nanofluid. *Experimental Thermal and Fluid Science, 51*, 103-111.

Barrat, J., & Chiaruttini, F. (2003). Kapitza resistance at the liquid—solid interface. *Molecular Physics, 101*(11), 1605-1610.

Barrau, J., Rosell, J., Chemisana, D., Tadrist, L., & Ibañez, M. (2011). Effect of a hybrid jet impingement/micro-channel cooling device on the performance of densely packed PV cells under high concentration. *Solar Energy, 85*(11), 2655-2665.

Bastea, S. (2005). Comment on``Model for heat conduction in nanofluids". *Physical Review Letters, 95*(1), 19401.

Beck, M. P., Yuan, Y., Warrier, P., & Teja, A. S. (2009). The effect of particle size on the thermal conductivity of alumina nanofluids. *Journal of Nanoparticle Research, 11*(5), 1129-1136.

Behzadmehr, A., Saffar-Avval, M., & Galanis, N. (2007). Prediction of turbulent forced convection of a nanofluid in a tube with uniform heat flux using a two phase approach. *International Journal of Heat and Fluid Flow, 28*(2), 211-219.

Bejan, A. (1996). *Entropy generation minimization: The method of thermodynamic optimization of finite-size systems and finite-time processes* Boca Raton: CRC Press.

Bianco, V., Manca, O., & Nardini, S. (2011). Numerical investigation on nanofluids turbulent convection heat transfer inside a circular tube. *International Journal of Thermal Sciences, 50*(3), 341-349.

Bruggeman, V. D. (1935). Berechnung verschiedener physikalischer konstanten von heterogenen substanzen. I. dielektrizitätskonstanten und leitfähigkeiten der mischkörper aus isotropen substanzen. *Annalen Der Physik, 416*(7), 636-664.

Buongiorno, J., Venerus, D. C., Prabhat, N., McKrell, T., Townsend, J., Christianson, R., Alvarado, J. L. (2009). A benchmark study on the thermal conductivity of nanofluids. *Journal of Applied Physics, 106*(9), 094312-1-14.

Chandrasekar, M., Suresh, S., & Chandra Bose, A. (2010). Experimental investigations and theoretical determination of thermal conductivity and viscosity of Al_2O_3/water nanofluid. *Experimental Thermal and Fluid Science, 34*(2), 210-216.

Chein, R., & Chuang, J. (2007). Experimental microchannel heat sink performance studies using nanofluids. *International Journal of Thermal Sciences, 46*(1), 57-66.

Chen, H., Witharana, S., Jin, Y., Kim, C., & Ding, Y. (2009). Predicting thermal conductivity of liquid suspensions of nanoparticles (nanofluids) based on rheology. *Particuology, 7*(2), 151-157.

Chon, C. H., Kihm, K. D., Lee, S. P., & Choi, S. U. (2005). Empirical correlation finding the role of temperature and particle size for nanofluid (Al_2O_3) thermal conductivity enhancement. *Applied Physics Letters, 87*, 153107-1-3.

Colangelo, G., Favale, E., de Risi, A., & Laforgia, D. (2012). Results of experimental investigations on the heat conductivity of nanofluids based on diathermic oil for high temperature applications. *Applied Energy, 97*, 828-833.

Corcione, M. (2011). Empirical correlating equations for predicting the effective thermal conductivity and dynamic viscosity of nanofluids. *Energy Conversion and Management, 52*(1), 789-793.

Coventry, J. S. (2005). Performance of a concentrating photovoltaic/thermal solar collector. *Solar Energy, 78*(2), 211-222.

Das, S. K., Putra, N., Thiesen, P., & Roetzel, W. (2003). Temperature dependence of thermal conductivity enhancement for nanofluids. *Journal of Heat Transfer, 125*(4), 567-574.

Davis, R. (1986). The effective thermal conductivity of a composite material with spherical inclusions. *International Journal of Thermophysics, 7*(3), 609-620.

Demir, H., Dalkilic, A., Kürekci, N., Duangthongsuk, W., & Wongwises, S. (2011). Numerical investigation on the single phase forced convection heat transfer characteristics of TiO_2 nanofluids in a double-tube counter flow heat exchanger. *International Communications in Heat and Mass Transfer, 38*(2), 218-228.

Du, B., Hu, E., & Kolhe, M. (2012). Performance analysis of water cooled concentrated photovoltaic (CPV) system. *Renewable and Sustainable Energy Reviews, 16*(9), 6732-6736.

Duangthongsuk, W., & Wongwises, S. (2010). An experimental study on the heat transfer performance and pressure drop of TiO_2-water nanofluids flowing under a turbulent flow regime. *International Journal of Heat and Mass Transfer, 53*(1), 334-344.

Eastman, J., Choi, U., Li, S., Thompson, L., & Lee, S. (1997). Enhanced thermal conductivity through the development of nanofluids. Paper presented at the *Materials Research Society Symposium Proceedings, , 457* 3-12.

Elias, M., Shahrul, I., Mahbubul, I., Saidur, R., & Rahim, N. (2014). Effect of different nanoparticle shapes on shell and tube heat exchanger using different baffle angles and operated with nanofluid. *International Journal of Heat and Mass Transfer, 70*, 289-297.

Elmir, M., Mehdaoui, R., & Mojtabi, A. (2012). Numerical simulation of cooling a solar cell by forced convection in the presence of a nanofluid. *Energy Procedia, 18*, 594-603.

Evans, D., & Florschuetz, L. (1978). Terrestrial concentrating photovoltaic power system studies. *Solar Energy, 20*(1), 37-43.

Evans, W., Fish, J., & Keblinski, P. (2006). Role of brownian motion hydrodynamics on nanofluid thermal conductivity. *Applied Physics Letters, 88*(9), 093116-1-3.

Evans, W., Prasher, R., Fish, J., Meakin, P., Phelan, P., & Keblinski, P. (2008). Effect of aggregation and interfacial thermal resistance on thermal conductivity of nanocomposites

and colloidal nanofluids. *International Journal of Heat and Mass Transfer, 51*(5), 1431-1438.

Feng, Y., & Kleinstreuer, C. (2012). Thermal nanofluid property model with application to nanofluid flow in a parallel disk System—Part II: Nanofluid flow between parallel disks. *Journal of Heat Transfer, 134*(5)

Fotukian, S., & Nasr Esfahany, M. (2010a). Experimental investigation of turbulent convective heat transfer of dilute γ-Al_2O_3/water nanofluid inside a circular tube. *International Journal of Heat and Fluid Flow, 31*(4), 606-612.

Fotukian, S., & Nasr Esfahany, M. (2010b). Experimental study of turbulent convective heat transfer and pressure drop of dilute CuO/water nanofluid inside a circular tube. *International Communications in Heat and Mass Transfer, 37*(2), 214-219.

Fox, R. W., McDonald, A. T., and Pritchard, P. J. (2004), *Introduction to Fluid Mechanics*, 6^{th}, Wiley, New York.

Garnett, J. M. (1906). Colours in metal glasses, in metallic films, and in metallic solutions. II. *Philosophical Transactions of the Royal Society of London.Series A, Containing Papers of a Mathematical Or Physical Character, ,* 237-288.

Ge, S., and Na, H. (1989), *Thermal Radiation Properties and Its Measurement*, Science Press, Beijing, pp. 446–451. (In Chinese)

Gharagozloo, P. E., & Goodson, K. E. (2011). Temperature-dependent aggregation and diffusion in nanofluids. *International Journal of Heat and Mass Transfer, 54*(4), 797-806.

Haddad, Z., Abid, C., Oztop, H. F., & Mataoui, A. (2014). A review on how the researchers prepare their nanofluids. *International Journal of Thermal Sciences, 76,* 168-189.

Hamilton, R., & Crosser, O. (1962). Thermal conductivity of heterogeneous two-component systems. *Industrial & Engineering Chemistry Fundamentals, 1*(3), 187-191.

Han, X., Wang, Y., & Zhu, L. (2013). The performance and long-term stability of silicon concentrator solar cells immersed in dielectric liquids. *Energy Conversion and Management, 66,* 189-198.

Hasselman, D., & Johnson, L. F. (1987). Effective thermal conductivity of composites with interfacial thermal barrier resistance. *Journal of Composite Materials, 21*(6), 508-515.

Hemmat Esfe, M., Saedodin, S., & Mahmoodi, M. (2014). Experimental studies on the convective heat transfer performance and thermophysical properties of MgO–water nanofluid under turbulent flow. *Experimental Thermal and Fluid Science, 52*, 68-78.

Heyhat, M., Kowsary, F., Rashidi, A., Alem Varzane Esfehani, S., & Amrollahi, A. (2012). Experimental investigation of turbulent flow and convective heat transfer characteristics of alumina water nanofluids in fully developed flow regime. *International Communications in Heat and Mass Transfer, 39*(8), 1272-1278.

Ho, T., Mao, S. S., & Greif, R. (2010). Improving efficiency of high-concentrator photovoltaics by cooling with two-phase forced convection. *International Journal of Energy Research, 34*(14), 1257-1271.

Hong, S. W., Kang, Y., Kleinstreuer, C., & Koo, J. (2011). Impact analysis of natural convection on thermal conductivity measurements of nanofluids using the transient hot-wire method. *International Journal of Heat and Mass Transfer, 54*(15), 3448-3456.

Huang, B. J., Lin, T. H., Hung, W. C., & Sun, F. S. (2001). Performance evaluation of solar photovoltaic/thermal systems. *Solar Energy, 70*(5), 443-448.

Iranidokht, V., Hamian, S., Mohammadi, N., & Shafii, M. B. (2013). Thermal conductivity of mixed nanofluids under controlled pH conditions. *International Journal of Thermal Sciences, 74*, 63-71.

Jamal-Abad, M. T., Zamzamian, A., & Dehghan, M. (2013). Experimental studies on the heat transfer and pressure drop characteristics of cu-water and al-water nanofluids in a spiral coil. *Experimental Thermal and Fluid Science, 47*, 206-212.

Jang, S. P., & Choi, S. U. (2004). Role of brownian motion in the enhanced thermal conductivity of nanofluids. *Applied Physics Letters, 84*(21), 4316-4318.

Jeffrey, D. J. (1973). Conduction through a random suspension of spheres. *Proceedings of the Royal Society of London.A.Mathematical and Physical Sciences, 335*(1602), 355-367.

Jeong, J., Li, C., Kwon, Y., Lee, J., Kim, S. H., & Yun, R. (2013). Particle shape effect on the viscosity and thermal conductivity of ZnO nanofluids. *International Journal of Refrigeration, 36*(8), 2233-2241.

Jung, J., & Yoo, J. Y. (2009). Thermal conductivity enhancement of nanofluids in conjunction with electrical double layer (EDL). *International Journal of Heat and Mass Transfer, 52*(1), 525-528.

Kapitza, P. (1941). The study of heat transfer in helium II. *J.Phys.(USSR), 4*(3), 181-210.

Karthik, R., Harish Nagarajan, R., Raja, B., & Damodharan, P. (2012). Thermal conductivity of CuO–DI water nanofluids using 3-ω measurement technique in a suspended micro-wire. *Experimental Thermal and Fluid Science, 40*, 1-9.

Kays, W. M., & Crawford, M. E. (1993). *Convective heat and mass transfer*. New York: McGraw-Hill.

Keblinski, P., Phillpot, S., Choi, S., & Eastman, J. (2002). Mechanisms of heat flow in suspensions of nano-sized particles (nanofluids). *International Journal of Heat and Mass Transfer, 45*(4), 855-863.

Khedkar, R. S., Sonawane, S. S., & Wasewar, K. L. (2012). Influence of CuO nanoparticles in enhancing the thermal conductivity of water and monoethylene glycol based nanofluids. *International Communications in Heat and Mass Transfer, 39*(5), 665-669.

Kim, S. H., Choi, S. R., & KIM, D. (2007). Thermal conductivity of metal-oxide nanofluids: Particle size dependence and effect of laser irradiation. *Journal of Heat Transfer, 129*(3), 298-307.

Kleinstreuer, C. (2010), *Modern Fluid Dynamics: Basic Theory and Selected Applications in Macro-and Micro-fluidics*, Springer, New York.

Kleinstreuer, C., & Li, J. (2008). Discussion:"Effects of various parameters on nanofluid thermal conductivity"(jang, SP, and choi, SDS, 2007, ASME J. heat transfer,[bold 129], pp. 617–623). *Journal of Heat Transfer, 130*, 025501.

Kleinstreuer, C., & Feng, Y. (2011). Experimental and theoretical studies of nanofluid thermal conductivity enhancement: A review. *Nanoscale Research Letters, 6*(1), 1-13.

Kleinstreuer, C., & Feng, Y. (2012). Thermal nanofluid property model with application to nanofluid flow in a parallel-disk System—Part I: A new thermal conductivity model for nanofluid flow. *Journal of Heat Transfer*, *134*(5), 051002.

Kleinstreuer, C., Li, J., & Koo, J. (2008). Microfluidics of nano-drug delivery. *International Journal of Heat and Mass Transfer, 51*(23), 5590-5597.

Kleinstreuer, C., Childress, E., & Kennedy, A. (2013). Targeted drug delivery: Multifunctional nanoparticles and direct micro-drug delivery to tumors. In S. Becker, & A. Kuznetsov (Eds.), ***Transport in biological media*** (pp. 391-416) Elsevier.

Kole, M., & Dey, T. (2012). Effect of prolonged ultrasonication on the thermal conductivity of ZnO–ethylene glycol nanofluids. *Thermochimica Acta, 535*, 58-65.

Koo, J., & Kleinstreuer, C. (2004). A new thermal conductivity model for nanofluids. *Journal of Nanoparticle Research, 6*(6), 577-588.

Kulkarni, P., Baron, P. A., & Willeke, K. (2011). *Aerosol measurement: principles, techniques, and applications*. John Wiley & Sons.

Kumar, D. H., Patel, H. E., Kumar, V. R., Sundararajan, T., Pradeep, T., & Das, S. K. (2004). Model for heat conduction in nanofluids. *Physical Review Letters, 93*(14), 144301.

Laufer, J. (1948). *Investigation of turbulent flow in a two-dimensional channel.* (PhD, California Institute of Technology).

Leal, L. (1973). On the effective conductivity of a dilute suspension of spherical drops in the limit of low particle peclet number. *Chemical Engineering Communications*, *1*(1), 21-31.

Lee, D., Kim, J., & Kim, B. G. (2006). A new parameter to control heat transport in nanofluids: Surface charge state of the particle in suspension. *The Journal of Physical Chemistry B, 110*(9), 4323-4328.

Lee, G., Kim, C., Lee, M. K., Rhee, C. K., Kim, S., & Kim, C. (2012). Thermal conductivity enhancement of ZnO nanofluid using a one-step physical method. *Thermochimica Acta, 542*, 24-27.

Lee, J., Hwang, K. S., Jang, S. P., Lee, B. H., Kim, J. H., Choi, S. U., & Choi, C. J. (2008). Effective viscosities and thermal conductivities of aqueous nanofluids containing low

volume concentrations of Al_2O_3 nanoparticles. *International Journal of Heat and Mass Transfer, 51*(11), 2651-2656.

Li, C. H., & Peterson, G. P. (2006). Experimental investigation of temperature and volume fraction variations on the effective thermal conductivity of nanoparticle suspensions (nanofluids). *Journal of Applied Physics, 99*(8), 084314-1-8.

Li, C. H., & Peterson, G. P. (2007a). The effect of particle size on the effective thermal conductivity of Al_2O_3-water nanofluids. *Journal of Applied Physics, 101*(4), 044312-1-5.

Li, C. H., & Peterson, G. P. (2007b). Mixing effect on the enhancement of the effective thermal conductivity of nanoparticle suspensions (nanofluids). *International Journal of Heat and Mass Transfer, 50*(23), 4668-4677.

Li, C. H., Williams, W., Buongiorno, J., Hu, L., & Peterson, G. P. (2008). Transient and steady-state experimental comparison study of effective thermal conductivity of Al_2O_3/water nanofluids. *Journal of Heat Transfer, 130*, 042407-1-7.

Li, J., & Kleinstreuer, C. (2008). Thermal performance of nanofluid flow in microchannels. *International Journal of Heat and Fluid Flow, 29*(4), 1221-1232.

Li, J., & Kleinstreuer, C. (2010). Entropy generation analysis for nanofluid flow in microchannels. *Journal of Heat Transfer, 132*(12)

Li, Q., Xuan, Y., & Wang, J. (2003). Investigation on convective heat transfer and flow features of nanofluids. *Journal of Heat Transfer, 125*, 151-155.

Liao, L., & Liu, Z. (2009). Forced convective flow drag and heat transfer characteristics of carbon nanotube suspensions in a horizontal small tube. *Heat and Mass Transfer, 45*(8), 1129-1136.

Lindgren, E. R. (1965). *Experimental study on turbulent pipe flows of distilled water*. (No. Report 1 AD21071). Stillwater: Civil Eng. Dept., Oklahoma State Univ.

Liu, J., Wang, F., Zhang, L., Fang, X., & Zhang, Z. (2014). Thermodynamic properties and thermal stability of ionic liquid-based nanofluids containing graphene as advanced heat transfer fluids for medium-to-high-temperature applications. *Renewable Energy, 63*, 519-523.

Longo, G. A., & Zilio, C. (2011). Experimental measurement of thermophysical properties of oxide–water nano-fluids down to ice-point. *Experimental Thermal and Fluid Science, 35*(7), 1313-1324.

LotfizadehDehkordi, B., Ghadimi, A., & Metselaar, H. S. (2013). Box–Behnken experimental design for investigation of stability and thermal conductivity of TiO_2 nanofluids. *Journal of Nanoparticle Research, 15*(1), 1-9.

Maciej, W., Anna, D., Pawel, R., & Dariusz, K. (2013). Thermal conductivity of highly loaded aluminium nitride–poly (propylene glycol) dispersions. *International Journal of Heat and Mass Transfer, 65*, 592-598.

Mahian, O., Kianifar, A., Kalogirou, S. A., Pop, I., & Wongwises, S. (2013). A review of the applications of nanofluids in solar energy. *International Journal of Heat and Mass Transfer, 57*(2), 582-594.

Mahian, O., Kianifar, A., Kleinstreuer, C., Al-Nimr, M. A., Pop, I., Sahin, A. Z., & Wongwises, S. (2013). A review of entropy generation in nanofluid flow. *International Journal of Heat and Mass Transfer, 65*, 514-532.

Maïga, S. E. B., Nguyen, C. T., Galanis, N., Roy, G., Maré, T., & Coqueux, M. (2006). Heat transfer enhancement in turbulent tube flow using Al_2O_3 nanoparticle suspension. *International Journal of Numerical Methods for Heat & Fluid Flow, 16*(3), 275-292.

Mallick, S., Mishra, A., & Kundan, L. (2013). An investigation into modelling thermal conductivity for alumina-water nanofluids. *Powder Technology, 233*, 234-244.

Maxwell, J. C. (1881). *A treatise on electricity and magnetism.* Clarendon press.

Menter, F. R. (1994). Two-equation eddy-viscosity turbulence models for engineering applications. *AIAA Journal, 32*(8), 1598-1605.

Meriläinen, A., Seppälä, A., Saari, K., Seitsonen, J., Ruokolainen, J., Puisto, S., Ala-Nissila, T. (2013). Influence of particle size and shape on turbulent heat transfer characteristics and pressure losses in water-based nanofluids. *International Journal of Heat and Mass Transfer, 61*, 439-448.

Micheli, L., Sarmah, N., Luo, X., Reddy, K., & Mallick, T. K. (2013). Opportunities and challenges in micro-and nano-technologies for concentrating photovoltaic cooling: A review. *Renewable and Sustainable Energy Reviews, 20*, 595-610.

Moghadassi, A., Hosseini, S. M., & Henneke, D. E. (2010a). Effect of CuO nanoparticles in enhancing the thermal conductivities of monoethylene glycol and paraffin fluids. *Industrial & Engineering Chemistry Research, 49*(4), 1900-1904.

Müller, M., Escher, W., Ghannam, R., Goicochea, J., Michel, B., Ong, C., & Paredes, S. (2011). Ultra-High-Concentration Photovoltaic-Thermal systems based on microfluidic Chip-Coolers. Paper presented at the *AIP Conference Proceedings, , 1407* 231.

Murshed, S., Leong, K., & Yang, C. (2005). Enhanced thermal conductivity of TiO_2-water based nanofluids. *International Journal of Thermal Sciences, 44*(4), 367-373.

Nabi, S., & Shirani, E. (2012). Simultaneous effects of brownian motion and clustering of nanoparticles on thermal conductivity of nanofluids. *IJST, Transactions of Mechanical Engineering, 36*, 53-68.

Naegeli, C. (2013). **The power of 2000 suns**. Retrieved 01/16, 2014, from **https://www.ethlife.ethz.ch/archive_articles/130422_hcpvt_cn/index_EN.**

Naik, M., Janardana, G. R., & Sundar, L. S. (2013). Experimental investigation of heat transfer and friction factor with water–propylene glycol based CuO nanofluid in a tube with twisted tape inserts. *International Communications in Heat and Mass Transfer, 46*, 13-21.

Namburu, P. K., Das, D. K., Tanguturi, K. M., & Vajjha, R. S. (2009). Numerical study of turbulent flow and heat transfer characteristics of nanofluids considering variable properties. *International Journal of Thermal Sciences, 48*(2), 290-302.

Nan, C., Birringer, R., Clarke, D. R., & Gleiter, H. (1997). Effective thermal conductivity of particulate composites with interfacial thermal resistance. *Journal of Applied Physics, 81*(10), 6692-6699.

Nan, C., Liu, G., Lin, Y., & Li, M. (2004). Interface effect on thermal conductivity of carbon nanotube composites. *Applied Physics Letters, 85*(16), 3549-3551.

Nguyen, C. T., Roy, G., Gauthier, C., & Galanis, N. (2007). Heat transfer enhancement using Al_2O_3-water nanofluid for an electronic liquid cooling system. *Applied Thermal Engineering, 27*(8), 1501-1506.

Nieto de Castro, C., Murshed, S., Lourenço, M., Santos, F., Lopes, M., & França, J. (2012). Enhanced thermal conductivity and specific heat capacity of carbon nanotubes ionanofluids. *International Journal of Thermal Sciences, 62*, 34-39.

Pak, B. C., & Cho, Y. I. (1998). Hydrodynamic and heat transfer study of dispersed fluids with submicron metallic oxide particles. *Experimental Heat Transfer an International Journal, 11*(2), 151-170.

Pang, C., Jung, J., Lee, J. W., & Kang, Y. T. (2012). Thermal conductivity measurement of methanol-based nanofluids with Al_2O_3 and SiO_2 nanoparticles. *International Journal of Heat and Mass Transfer, 55*(21-22), 5597-5602.

Paul, G., Sarkar, S., Pal, T., Das, P., & Manna, I. (2012). Concentration and size dependence of nano-silver dispersed water based nanofluids. *Journal of Colloid and Interface Science, 371*(1), 20-27.

Prasher, R., Bhattacharya, P., & Phelan, P. E. (2005). Thermal conductivity of nanoscale colloidal solutions (nanofluids). *Physical Review Letters, 94*(2), 025901.

Prasher, R., Phelan, P. E., & Bhattacharya, P. (2006). Effect of aggregation kinetics on the thermal conductivity of nanoscale colloidal solutions (nanofluid). *Nano Letters, 6*(7), 1529-1534.

Putnam, S. A., & Cahill, D. G. (2004). Micron-scale apparatus for measurements of thermodiffusion in liquids. *Review of Scientific Instruments, 75*(7), 2368-2372.

Putnam, S. A., Cahill, D. G., Braun, P. V., Ge, Z., & Shimmin, R. G. (2006). Thermal conductivity of nanoparticle suspensions. *Journal of Applied Physics, 99*(8), 084308-1-6.

Ratts, E. B., & Raut, A. G. (2004). Entropy generation minimization of fully developed internal flow with constant heat flux. *Journal of Heat Transfer, 126*(4), 656-659.

Rohsenow, W. M., Hartnett, J. P., and Cho, Y. I. (1998), *Handbook of Heat Transfer,* McGraw-Hill, New York.

Rosen, M. J., & Kunjappu, J. T. (2012). *Surfactants and interfacial phenomena* John Wiley & Sons.

Royne, A., Dey, C. J., & Mills, D. R. (2005). Cooling of photovoltaic cells under concentrated illumination: A critical review. *Solar Energy Materials and Solar Cells, 86*(4), 451-483.

Rusconi, R., Isa, L., & Piazza, R. (2004). Thermal-lensing measurement of particle thermophoresis in aqueous dispersions. *JOSA B, 21*(3), 605-616.

Rusconi, R., Rodari, E., & Piazza, R. (2006). Optical measurements of the thermal properties of nanofluids. *Applied Physics Letters, 89*(26), 261916-1-3.

Sahin, B., Gültekin, G. G., Manay, E., & Karagoz, S. (2013). Experimental investigation of heat transfer and pressure drop characteristics of Al_2O_3-water nanofluid. *Experimental Thermal and Fluid Science, 50*, 21-28.

Sala, G. (1989). Cooling of solar cells. *Solar Cells and Optics for Photovoltaic Concentration.Adam Hilger–IOP Publishing,* , 239-267.

Shenogin, S., Xue, L., Ozisik, R., Keblinski, P., & Cahill, D. G. (2004). Role of thermal boundary resistance on the heat flow in carbon-nanotube composites. *Journal of Applied Physics, 95*(12), 8136-8144.

Shima, P., Philip, J., & Raj, B. (2010). Synthesis of aqueous and nonaqueous iron oxide nanofluids and study of temperature dependence on thermal conductivity and viscosity. *The Journal of Physical Chemistry C, 114*(44), 18825-18833.

Shima, P. D., & Philip, J. (2014). Role of thermal conductivity of dispersed nanoparticle on heat transfer properties of nanofluid. *Industrial & Engineering Chemistry Research, 53*(2), 980-988.

Shukla, R. K., & Dhir, V. K. (2008). Effect of brownian motion on thermal conductivity of nanofluids. *Journal of Heat Transfer, 130*(4), 040301-1-4.

Skoplaki, E., & Palyvos, J. (2009). On the temperature dependence of photovoltaic module electrical performance: A review of efficiency/power correlations. *Solar Energy, 83*(5), 614-624.

Sparrow, E., Hallman, T., & Siegel, R. (1957). Turbulent heat transfer in the thermal entrance region of a pipe with uniform heat flux. *Applied Scientific Research, Section A, 7*(1), 37-52.

Sundar, L. S., Farooky, M. H., Sarada, S. N., & Singh, M. (2012). Experimental thermal conductivity of ethylene glycol and water mixture based low volume concentration of Al_2O_3 and CuO nanofluids. *International Communications in Heat and Mass Transfer, 41*, 41-46.

Sundar, L. S., Singh, M. K., & Sousa, A. (2013). Thermal conductivity of ethylene glycol and water mixture based Fe_3O_4 nanofluid. *International Communications in Heat and Mass Transfer, 49*, 17-24.

Timofeeva, E. V., Gavrilov, A. N., McCloskey, J. M., Tolmachev, Y. V., Sprunt, S., Lopatina, L. M., & Selinger, J. V. (2007). Thermal conductivity and particle agglomeration in alumina nanofluids: Experiment and theory. *Physical Review E, 76*(6), 061203.

Timofeeva, E. V., Routbort, J. L., & Singh, D. (2009). Particle shape effects on thermophysical properties of alumina nanofluids. *Journal of Applied Physics, 106*(1), 014304-1-10.

Timofeeva, E. V., Smith, D. S., Yu, W., France, D. M., Singh, D., & Routbort, J. L. (2010). Particle size and interfacial effects on thermo-physical and heat transfer characteristics of water-based α-SiC nanofluids. *Nanotechnology, 21*, 215703-1-10.

Timofeeva, E. V., Yu, W., France, D. M., Singh, D., & Routbort, J. L. (2011). Base fluid and temperature effects on the heat transfer characteristics of SiC in ethylene glycol/H_2O and H_2O nanofluids. *Journal of Applied Physics, 109*(1), 014914-014914-5.

Turgut, A., Tavman, I., Chirtoc, M., Schuchmann, H., Sauter, C., & Tavman, S. (2009). Thermal conductivity and viscosity measurements of water-based TiO_2 nanofluids. *International Journal of Thermophysics, 30*(4), 1213-1226.

Venerus, D. C., Schieber, J. D., Iddir, H., Guzman, J. D., & Broerman, A. W. (1999). Measurement of thermal diffusivity in polymer melts using forced rayleigh light scattering. *Journal of Polymer Science Part B: Polymer Physics, 37*(11), 1069-1078.

Venerus, D. C., Kabadi, M. S., Lee, S., & Perez-Luna, V. (2006). Study of thermal transport in nanoparticle suspensions using forced rayleigh scattering. *Journal of Applied Physics, 100*(9), 094310-1-5.

Wang, B., Zhou, L., & Peng, X. (2003). A fractal model for predicting the effective thermal conductivity of liquid with suspension of nanoparticles. *International Journal of Heat and Mass Transfer, 46*(14), 2665-2672.

Wang, X., Xu, X., & S. Choi, S. U. (1999). Thermal conductivity of nanoparticle-fluid mixture. *Journal of Thermophysics and Heat Transfer, 13*(4), 474-480.

Wasp, E. J., Kenny, J. P., & Gandhi, R. L. (1977). Solid--liquid flow: Slurry pipeline transportation.[pumps, valves, mechanical equipment, economics]. *Ser.Bulk Mater. Handl.; (United States), 1*(4)

Williams, W., Buongiorno, J., & Hu, L. (2008). Experimental investigation of turbulent convective heat transfer and pressure loss of alumina/water and zirconia/water nanoparticle colloids (nanofluids) in horizontal tubes. *Journal of Heat Transfer, 130*(4), 040301.1-044503.4.

Xie, H., Wang, J., Xi, T., Liu, Y., Ai, F., & Wu, Q. (2002a). Thermal conductivity enhancement of suspensions containing nanosized alumina particles. *Journal of Applied Physics, 91*(7), 4568-4572.

Xie, H., Lee, H., Youn, W., & Choi, M. (2003). Nanofluids containing multiwalled carbon nanotubes and their enhanced thermal conductivities. *Journal of Applied Physics, 94*(8), 4967-4971.

Xie, H., Wang, J., Xi, T., Liu, Y., & Ai, F. (2002). Dependence of the thermal conductivity of nanoparticle-fluid mixture on the base fluid. *Journal of Materials Science Letters, 21*(19), 1469-1471.

Xie, H., Wang, J., Xi, T., Liu, Y., Ai, F., & Wu, Q. (2002b). Thermal conductivity enhancement of suspensions containing nanosized alumina particles. *Journal of Applied Physics, 91*(7), 4568-4572.

Xu, J., Yu, B., Zou, M., & Xu, P. (2006). A new model for heat conduction of nanofluids based on fractal distributions of nanoparticles. *Journal of Physics D: Applied Physics, 39*, 4486-4490.

Xuan, Y., Li, Q., & Hu, W. (2003). Aggregation structure and thermal conductivity of nanofluids. *AIChE Journal, 49*(4), 1038-1043.

Xuan, Y., Li, Q., Zhang, X., & Fujii, M. (2006). Stochastic thermal transport of nanoparticle suspensions. *Journal of Applied Physics, 100*(4), 043507-1-6.

Yang, B. (2008). Thermal conductivity equations based on brownian motion in suspensions of nanoparticles (nanofluids). *Journal of Heat Transfer, 130*(4), 042408-1-5.

Yang, J., Li, F., Zhou, W., He, Y., & Jiang, B. (2012). Experimental investigation on the thermal conductivity and shear viscosity of viscoelastic-fluid-based nanofluids. *International Journal of Heat and Mass Transfer, 55*(11), 3160-3166.

Yiamsawasd, T., Dalkilic, A. S., & Wongwises, S. (2012). Measurement of the thermal conductivity of titania and alumina nanofluids. *Thermochimica Acta, 545*, 48-56.

Yu, W., France, D. M., Choi, S. U., & Routbort, J. L. (2007). Review and assessment of nanofluid technology for transportation and other applications. *(No. ANL/ESD/07-9). Argonne National Laboratory (ANL).,*

Yu, W., Xie, H., Li, Y., & Chen, L. (2011). Experimental investigation on thermal conductivity and viscosity of aluminum nitride nanofluid. *Particuology, 9*(2), 187-191.

Yu, W., France, D. M., Routbort, J. L., & Choi, S. U. (2008). Review and comparison of nanofluid thermal conductivity and heat transfer enhancements. *Heat Transfer Engineering, 29*(5), 432-460.

Yu, W., France, D. M., Smith, D. S., Singh, D., Timofeeva, E. V., & Routbort, J. L. (2009). Heat transfer to a silicon carbide/water nanofluid. *International Journal of Heat and Mass Transfer, 52*(15), 3606-3612.

Yu, W., France, D. M., Timofeeva, E. V., Singh, D., & Routbort, J. L. (2012). Comparative review of turbulent heat transfer of nanofluids. *International Journal of Heat and Mass Transfer, 55*(21-22), 5380-5396.

Zhu, D., Li, X., Wang, N., Wang, X., Gao, J., & Li, H. (2009). Dispersion behavior and thermal conductivity characteristics of Al_2O_3-H_2O nanofluids. *Current Applied Physics, 9*(1), 131-139.

Zhu, L., Boehm, R. F., Wang, Y., Halford, C., & Sun, Y. (2011). Water immersion cooling of PV cells in a high concentration system. *Solar Energy Materials and Solar Cells*, *95*(2), 538-545.